MOLECULAR ORIGINS OF POLYMORPHIC PHASE TRANSITIONS FOR DYNAMIC ORGANIC ELECTRONICS

BY

DANIEL DAVIES

DISSERTATION

Submitted in partial fulfillment of the requirements
for the degree of Doctor of Philosophy in Chemical Engineering
in the Graduate College of the
University of Illinois Urbana-Champaign, 2022

Urbana, Illinois

Doctoral Committee:

Associate Professor Ying Diao, Chair
Assistant Professor Christopher Evans
Professor Baron G. Peters
Professor Hong Yang

ABSTRACT

The correlation between polymorph discovery and the time and effort spent researching a compound was famously proposed by McCrone in 1965. Nearly 60 years later, and despite the importance of polymorphic structure to a variety of properties, polymorphs are still mostly found through tried-and-true serendipity. However, control over the polymorphic structure is critical for fully realizing the performance of organic semiconductors requiring a deep understanding of the molecular origins regulating these polymorphic structures. This is particularly the case in quinoidal n-type semiconductors which have significantly lagged behind p-type counterparts.

One way to control polymorphism is through reversible phase transitions which may occur through different pathways. Typically transitions occur by nucleation and growth, which is widely observed among solid-to-solid transitions. These transitions occur via diffusive, molecule by molecule mechanisms which completely reconstructs the crystal and often disrupt the material structural integrity. In a few, but growing, number of crystals, cooperative structural transitions are found. These transitions, in contrast, involve simultaneous, concerted displacement of molecules in a crystalline material. Cooperative transitions have acquired much attention in the research community for their low transition barrier, ultrafast kinetics, and structural reversibility. Moreover, due to the displacive nature of the mechanism, many times shape changes and even thermosalient effects may be observed. Harnessing these behaviors offer a route to dynamic electronics not possible previously.

For our portion of time and effort devoted to the understanding of these polymorphic transitions, we uncover the prolific polymorphism in a high performing n-type organic semiconductor, 2 dimensional quinoidal terthiophene (2DQTT-o-B), obtaining at least 6 different polymorphs. These polymorphs exhibited vastly different structural characteristics as analyzed by single crystal X-ray diffraction (SCXRD) and grazing incidence X-ray diffraction (GIXD). Via the selection of these different polymorphic structures, we show tuning of the electron charge carrier mobility by 5 orders of magnitude. Moreover, we explore a thermally induced self doping effect in these devices.

Along with the rich polymorphic space, we observed the presence of both a cooperative and nucleation and growth transition via two reversible thermally triggered transitions in single crystals under in situ polarized optical microscopy (POM). The presence of both mechanisms offered an unprecedented chance to compare the origins of these mechanisms on an equal footing to isolate structural and molecular design effects on the transitions. Through Raman spectroscopy and GIXD, We show the cooperative behavior is driven by a reorientation of the alkyl chains, resulting in a change in the tilt of the molecules, much like dominos falling. On the other hand, the nucleation and growth behavior was driven by biradical formation and facilitated by melting alkyl chains. Moreover, the cooperative behavior is used to design novel single crystal thermally actuated organic semiconductor devices. By utilizing the cooperative shape change, the crystal can break and reform the contact with PEDOT:PSS, providing a thermally switchable device.

The molecular mechanisms suggested that the alkyl chains play a key, yet distinct role in both reversible phase transitions. We investigated the effect of alkyl chain length on both transition mechanisms by successively shortening the branched alkyl chain length and observing the transition behavior under in situ POM. We showed the at the shortest side chains, the cooperative behavior was suppressed, which was confirmed through Raman spectroscopy. Moreover, we showed the nucleation and growth behavior was present in all three systems, but the transition temperature increased with shorter side chains, consistent with a higher alkyl chain order to disorder transition. Moreover, the biradical formation showed a coupling with the phase transition, providing a new route to tuning the electronic structure behavior. This provides a generalizable design rule for controlling the cooperative behavior and fine tuning nucleation and growth pathways.

Finally, we explore the kinetic trapping of polymorph III at room temperature, resulting in significant breaking of the hexagonal symmetry, despite no first order transition, as well as changes to the electronic properties. Despite the property changes, this kinetically trapped state still retains insulating like behavior, orders of magnitude below the conductance from the stable form. We demonstrate a method using laser induced heating as a way to control the conversion of this kinetically trapped polymorph back to the stable form, allowing for tuning of the conductance state in the device. Using this setup, we fabricated a memristor device based on the electronic switching properties from this transition.

ACKNOWLEDGMENTS

As with most scientific endeavors, this project would not be possible without the continued support of my family, friends and colleagues. I extremely grateful for my advisor Dr. Ying Diao for all her effort and insightful discussion. She is one of the hardest working people I have met and that is apparent in everything she works on. I appreciate the opportunity she provided in letting me pursue this project to the end and in her help overcoming the many challenges along the way.

I am also grateful for the suggestions and ideas from my committee members, Dr. Hong Yang, Dr. Chris Evans and Dr. Baron Peters and their support through the defense process. I gratefully acknowledge the financial support of the Parr Fellowship, A.T. Widiger Fellowship and DuPont Science & Engineering Fellowship.

Additionally, I am forever indebted to all of the graduate students and post-doctoral researchers in the Diao group. I would particularly like to acknowledge Dr. Sang Kyu Park whose many discussions provided much needed ideas and support in making it through the toughest parts my project. Moreover, my work would not be finished without the help of Giorgio Graziano, who worked relentlessly in the pursuit of understanding the 2DQTT system. I am also glad to have had the opportunity to work closely alongside the many members of the Diao group: Dr. Bijal Patel, Dr. Prapti and Dr. Justin Kwok, Dr. Tim Chung, Dr. Ge Qu, Dr. Fengjiao Zhang, Kyung Sun Park, Dr. Gonzalo Campillo-Alvarado, and Dr, Erfan Mohammadi. Their collaborations, humor and kindness made working in this research group truly special. Moreover, appreciate the immense flexibility and helpfulness of Sanghyun Jeon and Changhyun Hwang who kindly adjusted their experiment schedule to accommodate me finishing my final project for this dissertation. Finally, I would like to thank Azzaya Khasbaatar, Siqing Wang, Kavinraaj Elangovan, Jong-Hoon Lee, Rui Zhang, and Tiara Torres Flores for all of the fantastic discussions, group lunches, parties and interactions. I could not imagine a better, more hardworking, cool group of individuals to spend 5 years of my life working with.

Along with those in the Diao group, I am especially thankful for the help from Dr. Danielle Gray and Toby Woods. Visiting Noyes laboratory to discuss crystallography and crystals in general was one of the highlights of my work. Every time I stopped by, I learned something completely unexpected and greatly appreciate the support in solving all of the messy molecular structures. Along with solving the crystal structures, I want to thank Dr. SuYin Grass Wang for her help in collecting these structures. Similarly, I would like to thank Dr. Joseph Strzalka for all of his help in collecting grazing incidence X-ray diffraction data at Argonne National Laboratory. I particularly appreciate his accommodations in accessing in situ measurements during the pandemic operations to finish out my last project. GIXD proved to be an invaluable technique and I look forward to visiting the beamline again when it reopens after the upgrades.

This project would not have reached the heights it has without the help of Stephen Shiring, Dr. Brett Savoie at Purdue University and Dr. Ralph Weber at Bruker instruments. Showing the biradical formation was critical for a complete understanding of this work and accessing this information at such extreme conditions and under such complicated structures is no easy feat. The simulation of the vibrational spectra together with the in situ EPR spectra were some of the most challenging parts of this work and I am grateful for all their help in these aspects.

I would not have made it to this point without all of the mentors and teachers that inspired me to pursue a career in research as well as provided invaluable knowledge, advice and skills. I am deeply grateful to have met and worked with Ms. Oberbroeckling, Mr. Neff and Dr. Julie Jessop. Their unending kindness and caring made me the person I am today and I hope to one day be half the teacher and mentor they have been for me.

I am grateful to have so many people in my life and want to specifically mention Brandon Walker, Sarah Goettler, Corrine Andresen, Abby Weaver, Katie Classon, and Nate Shires for being there with me through everything. Most importantly, I am most grateful for my family supporting me through this process. My parents have sat through every practice talk and read every paper without fail and I would not have made it through without their help. I would not be the person I am today without all of their guidance over the years. I also want to thank my brother Michael Davies for all of the late-night zoom calls discussing computer architecture at all levels. His computer programming skills are unparalleled and I would not have succeeded without his help. Hopefully some day we will get back to finishing Graze^{TM} and be able to write a paper together. As well, my brother and Sister Andy and Alexa Davies have continuously shown their unwavering support, always rooting for me. Finally, I also would not have made it through without significant support from my friends.

Dedicated to my family, friends, and fish

TABLE OF CONTENTS

CHAPTER 1: INTRODUCTION

1.1 ORGANIC SEMICONDUCTORS AS A "FLEXIBLE" ALTERNATIVE TO SILICON

Organic semiconductors offer a number of key advantages over inorganic counterparts such as solution processibility[1–4], enhanced mechanical properties[5–7] and access to diverse form factors[8,9]. We have seen this already revolutionize the consumer electronics industry in the production of organic light emitting diode (OLED) based panels allowing for a whole host of folding devices. At the 2022 Consumer Electronics Samsung revealed the extent of these folding designs in the tri-folding Flex S and even incorporated rollable screens in the Flex Slidable. Fully flexible, wearable electronics, however, requires utilizing organic semiconductors not only as OLEDs, but also as fully functioning logic operation based on transistor devices. Such devices are heavily dependent on the electronic properties of these molecules and are characterized by charge carrier mobility (μ = ~10^3 cm^2 V^{-1} s^{-1} for crystalline silicon) and ratio between the currents in the on and off states (~10^6 for silicon). The first organic field effect transistor was demonstrated by Tsumura, Koezuka and Ando in 1986[10], showing a modest mobility at 10^{-5} cm^2 V^{-1} s^{-1} and on off ratio of 10^2-10^3. However, since then the performance of organic semiconductors has been pushed to mobilities of 1-10 cm^2 V^{-1} s^{-1} and 10^6 on-off ratios, rivaling that of amorphous silicon (μ = ~1 cm^2 V^{-1} s^{-1})[11]. These advances provide a bright future in developing next generation logic and sensor devices for wearable electronics.

1.2 QUINOIDAL STRUCTURE: TOO RADICAL OR TWO RADICALS?

While high mobility p-type organic semiconductors have become numerous over the years, n-type counterparts have remained few and far between. Due to the need of injecting electrons, the LUMO level must be quite low in energy to match potential contact work functions. This can be done via adding strong electron withdrawing groups, however, typically leaves the molecule highly reactive and susceptible to degradation. To combat this, bulky side chains, such as long alkyl chains become necessary to prevent interaction with water or oxygen under ambient conditions.

One route to such electron deficient cores is via forming a quinoidal core by introducing cyano groups into the conjugated system and breaking the aromaticity. This was highly successful in the synthesis of tetracyanoquinodimethane (TCNQ), and its derivatives, which exhibit a high n-type mobility. However, due to the stabilizing power of aromaticity, the electronic structure of the quinoidal core provides a unique ground state. While the strong electron withdrawing groups can force this quinoidal form, aromaticity provides another potentially stable state. Depending on the exact molecular structure and the length of conjugation, this can result in stabilizing radicals at the terminal carbons of the cyano groups. This electronic structure creates an equilibrium between the quinoidal and aromatic forms that can be tuned via external stimuli such as temperature, chemical environment, etc. Moreover, the radical ground state allows for stabilization of both positive and negative charges, leading both ambipolar transport as well as self-doping effects[12].

Along with optical and electronic properties, the stabilized radicals alter both the molecular structure and intermolecular interactions. As a result of forming an aromatic system, some of the bonds switch between single and double bonds. This shift is characterized by the difference between the lengths of the double and single bonds called the bond length alternation (BLA). While in the aromatic form, bonds that would typically be static, become freely rotating single bonds allowing the molecules to isomerize in solution. Given the right conditions, molecules stabilizing the radicals may dimerize, forming elongated pseudo σ-bonds between the radical centers, leading to intriguing chromic effects. Moreover, these interactions can dominate the crystal formations as the interaction strength is on the same order as π-π interactions[13,14]. On the other hand, once in the solid state, intramolecular spin interactions (bond formation within the molecule) compete with intermolecular spin interactions[15–17]. These can take the form of peierls distortion or forming “pancake” bonded dimers or stacks[18,18,19,19,20].

The biradical ground state in these systems can be observed through a number of techniques such as Raman spectroscopy and electron paramagnetic resonance (EPR) spectroscopy. The resulting aromatic core has significantly different chemical features, which allows for the aromatic form to be distinguishable from the quinoidal form based on the vibrational modes observed. Under Raman spectroscopy, the C=C stretching in the conjugated core occurs at a much higher wavenumber in the aromatic state than that of the quinoidal form. On the other hand, the unpaired electrons result in a measurable spin state through EPR spectroscopy which can directly identify the number of spins in a system.

1.3 CHARGE TRANSPORT IN ORGANIC SEMICONDUCTORS

In typical inorganic semiconductors, and even some small molecule organic semiconductors such as pentacene, band-like transport dominates. In these scenarios the carrier charges become delocalized across the crystal, exhibiting a mean free path much longer than the a few molecules. In a perfect crystal, this delocalization occurs without scattering, however in the real case scattering occurs from defects and lattice phonon vibrations. Reducing the lattice vibrations in band transport, such as through decreasing temperature, results in increasing mobility.

However, in most organic crystals, charges move via a hopping mechanism, with charges localized on one or a few neighboring molecules. In this mechanism, the charges couple with phonon vibrations reflecting polaron behavior. The charge mobility (μ) is thus governed by the electron-phonon coupling interactions which in the classical sense, and is related to diffusion in the Einstein-Smoluchowski equation

$$\mu = \frac{eD}{k_B T}$$

Where e is the electron charge, D is the diffusion coefficient, k_B is the Boltzmann constant and T is the temperature[21–23]. In a 1-dimensional system, D follows Einstein's equation $D = a^2 k_{ET}$ where a is the molecular spacing and k_{ET} is the hopping rate. A decent approximation based on electron phonon interactions is given by:

$$k_{ET} = \frac{t^2}{\hbar}\left[\frac{\pi}{2E_{pol}k_BT}\right]^{\frac{1}{2}} \exp\left(-\frac{E_{pol}}{2k_BT}\right)$$

Where t is the transfer integral and E_{pol} is the polaron binding energy. This hopping rate can be substituted into the diffusion equation above to give a hopping mobility of:

$$\mu_{hop} = \frac{ea^2t^2}{k_BT\hbar}\left[\frac{\pi}{2E_{pol}k_BT}\right]^{\frac{1}{2}} \exp\left(-\frac{E_{pol}}{2k_BT}\right)$$

Where E_{pol} is related to the reorganization energy (λ) by $E_{pol} = \lambda/2$. This gives two important parameters in the determination of the charge mobility: the transfer integral, t, and the phonon reorganization energy, λ. The transfer integral provides an indication of the strength of intermolecular interactions whereas the reorganization energy reflects the strength of electron-phonon coupling. Generally, a larger transfer integral (higher intermolecular interaction) and reduced reorganization energy (lower electron-phonon coupling) are necessary to achieve high charge carrier mobility[21,23,24].

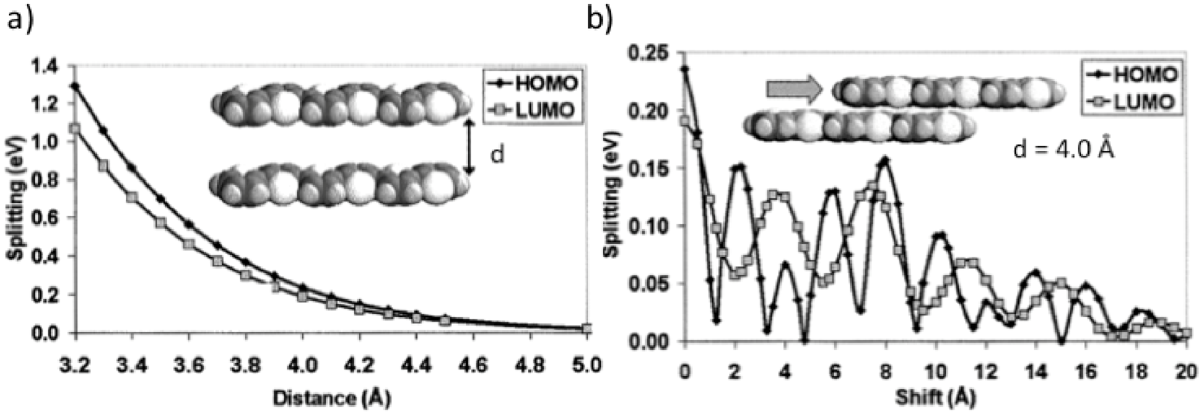

Figure 1.1. Calculations showing the HOMO and LUMO splitting for conjugated molecules as functions of (a) stacking distance and (b) shift position showing a complex relationship between the molecular stacking and π-overlap. Reproduced from[25].

Based on this theory for charge hopping, the transfer integral or π-orbital overlap plays a crucial role in how charges will move through the system. Calculations by J. Bredas and J. Cornil et. al. Show how even slight changes to the π system overlap can change this overlap and by extension, the electronic splitting between the HOMO and LUMO levels (Figure 1.1a,b)[24]. Naturally the π-stacking distance is a major factor in the transfer integral and increases with decreasing distance. However, they also established that translating the π-conjugated core results in a much more complex effect on the electronic splitting. Given that J. Bredas et. al. found even tiny shifts in the molecular overlap; we can see how accessing different crystal structures can dramatically shift the electronic properties.

1.4 THERMODYNAMICS OF POLYMORPHISM

Polymorphism, where a molecule can adopt multiple different crystal structures, has been shown to be extremely prevalent in organic molecules. By some surveys of the Cambridge structural database, at least 50% of molecules exhibit at least two different polymorphs[26,27]. The nucleation and growth of these different structures and their stability depends heavily on the free energy of the system. At constant pressure, the Gibbs free energy will additionally have a temperature component via

$$\Delta G = \Delta H - T\Delta S$$

Where ΔG is the difference in free energy, ΔH is the difference in enthalpy, T is temperature and ΔS is the difference in entropy. This can provide a detailed understanding of how polymorphs behave and the conditions under which they transition, as we will soon see.

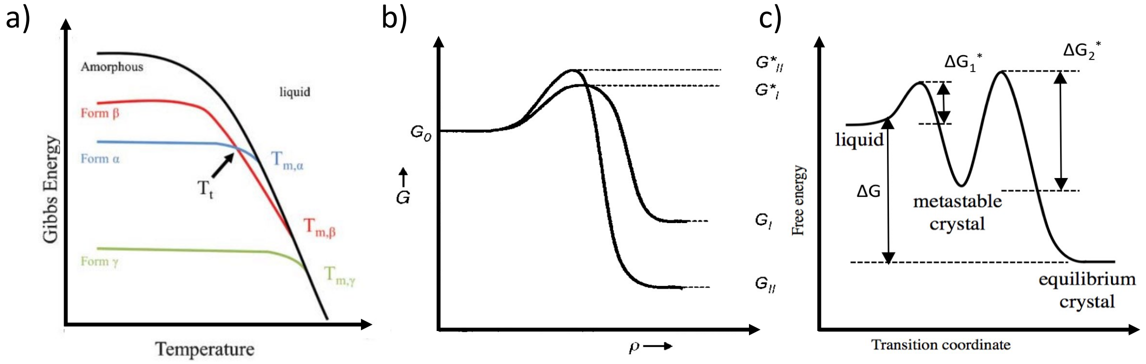

Figure 1.2. TIPS-P phase transition coupled with [100] shearing applied to the crystal (a,d) and twinning coupled with stretching. (a) Reproduced from[28]. (b) and (c) reproduced from[29]

When the free energy of a given molecular system is plotted, we may , there will be a thermodynamically stable form at the lowest free energy state, as in the case of γ in **Figure 1.2a**[28]. Other forms such as α and β will slowly convert to the stable γ over time, making α and β metastable and therefore monotropic with respect to γ. α and β will undergo an irreversible transition and will require other influences on reform those metastable structures. On the other hand, focusing on α and β, there is a point in the diagram where the free energy crosses, resulting in a change of which polymorph is more stable. This means α and β are enantiotropic and will undergo a reversible phase transition when the temperature crosses the transition temperature.

There are a number of methods to access metastable polymorphs through manipulating the nucleation and growth. Typical nucleation and growth for a system may take a path shown in **Figure 1.2b**[29] and exhibit a certain free energy barrier, depending on the particular crystal structure. The lower the barrier, the faster the nucleation rate allowing for tuning this kinetics to access a particular metastable polymorph that is faster. Moreover, the formation of particular structure typically follows Ostwald's rule of stages (**Figure 1.2c**), where the most metastable polymorph forms first and more stable structures form later[30–32]. This in connection with various crystallization methods such as solution printing, drop casting, slow evaporation etc. can tune the crystal formation rate to sometimes trap these more metastable forms[29,33–36]. Additionally, the nucleation barriers can be tuned through controlling nucleation conditions such as confinement and solvent selection. Nucleation barriers can even be completely bypassed in the presence of a seed crystal, causing disappearing (or new, appearing!) polymorphs resulting in countless sleepless nights for graduate students[33].

1.5 NUCLEATION AND GROWTH V.S. COOPERATIVE PHASE TRANSITIONS

During solid-to-solid phase transitions, two distinct pathways control the formation the new phase. Typically, these transitions undergo a nucleation and growth transition, similar to crystallizations processes discussed above. These transitions involve the nucleation of a new phase within the crystal and diffusive motion of molecules across a phase boundary to be incorporated into the daughter phase. The thermodynamics are much the same as discussed above, however in the sold state, the energy barriers can be significantly higher due to the low mobility of the molecules. As a result, many solid to solid transitions can be quite slow, requiring minutes to hours[37]. These transitions will typically take the original shape of the crystal, barring any significant change in density, and may form multiple domains due to no relationship between the crystallographic directions for the mother and daughter phases.

Cooperative phase transitions, in contrast, are a class of critical phenomena, similar in kind to magnetic switching at the curie temperature or ferromagnetic switching and is well-studied in inorganic martensitic transitions. These transitions result from a sudden, diffusionless, correlated motion of many molecules, very much unlike the diffusive motion of molecules in nucleation and growth. The diffusionless motion means the phase transition boundary is coupled with a particular lattice phonon vibration, which often undergo softening during the transition[38,39]. In a perfect crystal, the phonon coupling results in an intrinsic phase boundary velocity at the speed of sound in through the material[39–42]. However, in most real crystals, defects will introduce energy barriers that interrupt the cooperative motion, forming a rough free energy landscape and causing avalanche behaviors. In his article *"How Would we Recognize a Martensitic Transformation if it Bumped into us on a Dark & Austy Night"*, P. Clapp suggested we would know a cooperative transition by the sound they make due to the acoustic emission resulting from these avalanches[43].

Along with rapid kinetics and avalanche behavior, these cooperative transitions are intrinsically linked to mechanical properties within the crystal. Due to the diffusionless motion, there is a strict correlation between the orientation of the mother and daughter phases. This typically results in single to single crystal transitions, though under certain cases, twinned domains may also occur[5]. Moreover, any packing changes at the atomic or molecular level translate to changes in the shape of the crystal to maintain the orientation. Despite the relatively small motions of the molecules, this can lead to large changes in the length of the crystal even leading to thermosalient motionl[42,44,45]. This means the transition is also coupled with strain in the lattice allowing for unique mechanical effects such as shape memory[46–48], super elasticity[5,46,48,49] and ferroelasticity[5,50,51].

In fact, recently superelasticity and ferroelasticity observed for the first time in an organic semiconductor molecule. Park and Diao et. al. (2020)[52] showed a TIPS-P crystal held near the phase transition temperature undergoes rapid switching between polymorphs upon application and release of [100]-shear loading (i.e., superelasticity). The mechanical stress was also accompanied with a significant shape change (**Figure 1.3a,d**), previously shown to be thermally triggered[53]. In a similarly cooperative fashion, TIPS-P also exhibited cooperative twinning upon stretching of the crystal or [100] shearing at room temperature. Unlike the previous structural transitions, twinning preserves the same molecular packing in both the mother and daughter crystal (i.e., ferroelasticity), but introduces new domain boundaries which accommodate significant strain (**Figure 1.3b,e**). Remarkably, they demonstrated in the case of ferroelasticity that 70% of the charge carrier mobility is preserved under as large as 13% strain (**Figure J4c**. Not only does ferroelasticity maintain performance to high strains, but the twinning process is also reversible, showing no signs of degradation even after multiple cycles up to 2.5% strain (**Figure J4f**). This work establishes mechanically-induced cooperative transitions as a new stress-releasing mechanism for highly deformable single crystal electronic devices.

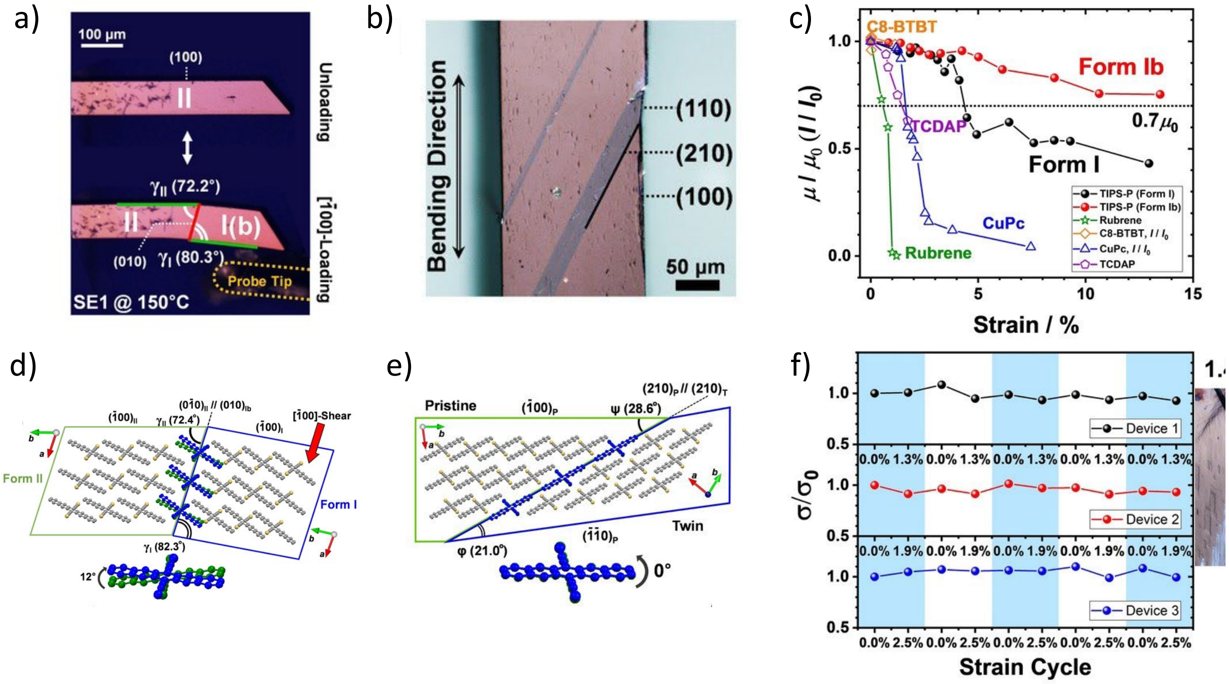

Figure 1.3. TIPS-P phase transition coupled with [100] shearing applied to the crystal (a,d) and twinning coupled with stretching (b,e) exhibiting superelasticity and ferroelasticity, respectively. Device performance under stretching showed (c) stable charge carrier mobility in TIPS-P crystals up to 5% strain in form I and even higher strains in form Ib along (f) with high recoverability across 5 cycles. Reproduced from[52].

1.6 THESIS OVERVIEW

In this thesis, I studied the polymorphic behavior of 2-dimensional quinoidal terthiophene (2DQTT-o-B), a high-performance n-type semiconductor. My research has shown prolific diversity in polymorphism and transition behavior resulting in 5 obtainable polymorphs showing variations in electronic over 5 orders of magnitude and corresponding to optical bandgap. Along with structural diversity, I found 2 thermally triggered reversible phase transitions showed both cooperative and nucleation and growth mechanisms in the same system. In situ microscopy, single crystal and grazing incidence X-ray diffraction, and Raman spectroscopy suggested the cooperative transition occurred via a reorientation in the alkyl side chains causing a change in molecular tilt. The nucleation and growth transition, on the other hand, shows alkyl chain melting coupled with an increased presence of biradical species, confirmed via in situ electron paramagnetic resonance spectroscopy. By adjusting the branching alkyl chain length, I could control the presence of the cooperative transition, “turning off” by shortening the side chain length. Moreover, we established synergistic effect between alkyl chain melting and biradical concentration during the nucleation and growth transition. Finally, via quenching of polymorph III, I kinetically trapped a sixth metastable polymorph and utilized laser writing to locally heat and direct the return to the stable form. Through understanding how the molecular structure affects the transition mechanisms, we can establish design rules to target these polymorphic behaviors in organic semiconductors. These phase transition enable dynamic electronics through combining structure and property switching.

CHAPTER 2: RADICALLY TUNABLE N-TYPE ORGANIC SEMICONDUCTOR VIA POLYMORPH CONTROL

2.1 CHAPTER OVERVIEW

Polymorphism has emerged as an important design consideration in organic semiconductors (OSCs). Previously in many OSCs, even small changes in molecular stacking can cause drastic changes to the optical and electronic properties. However, investigation into n-type semiconductors has significantly lagged behind their p-type counterparts. In this work, we present the prolific polymorphism of 2 dimensional quinoidal terthiophene (2DQTT-o-B) and systematically investigate each of 5 polymorphs, 3 of which have been previously unreported. Grazing incidence X-ray diffraction provided a key method to understanding the structure of each polymorph. Via the polymorphic transitions mapped, we tuned the electron mobility by 5 orders of magnitude, from $5.63x10^{-5}$ to 0.22 cm^2 V s^{-1}. These were accompanied by modifications to the optical properties, namely we observed substantial differences in the refractive index noted by intensity differences under polarized optical microscopy and large shift in optical band gap from 1.18 eV up to 1.40 eV. Finally, we suggest changes to these properties may be related to the unique quinoidal to aromatic transition observed in quinoidal molecules.

2.2 INTRODUCTION

Polymorphism has been widely demonstrated in systems ranging from inorganic metals to organic semiconductors and pharmaceuticals[23,34,39,54–56]. In these systems, changes in polymorphic structures can alter the critical material properties, such as solubility, hardness, melting point, optoelectronic properties among many others[35,57–59]. Particularly in organic molecules, where relatively weak interactions dominate, multiple polymorphs may be obtainable near ambient conditions[60–62]. These conditions may vary considerably, depending on the solvents, temperatures and processes involved (i.e. drop casting or solution shearing)[23,33,35,63]. However, understanding the presence and behavior of crystal polymorphism still eludes prediction, making systematic approaches to investigating these phenomena imperative.

In organic semiconductors, polymorphism as a design parameter for semiconducting properties is quite underexplored, despite the potential for changing charge transport characteristics by orders of magnitude. This is particularly the case in n-type semiconductors that have been significantly understudied compared to p-type semiconductors. N-type OSCs require an electronic structure capable of stabilizing negative charge carriers, mainly accomplished by accessing low lying LUMO levels, which typically leaves the molecule highly susceptible to degradation[64,65]. One path to obtaining a low LUMO level and stability for high performing n-type semiconductors is the introduction of strong electron withdrawing groups to conjugated cores such as cyano groups[3,65]. These cyano group based molecules such as tetracyanoquinodimethane (TCNQ) break the aromaticity of that conjugated core to form a quinoidal type structure[66–68]. This quinoidal molecular framework leads to reduced bandgaps and lower LUMO levels necessary for the n-type performance[69,70].

Moreover, the quinoidal structures has shown to lead to an exotic biradical ground state which facilitates the stabilization of both holes and electrons in the semiconducting material[68,71–74]. The stability of the biradical states has shown to be tunable based on the conjugation length of the quinoidal molecule. In the case of a series of 2 dimensional quinoidal thiophene molecules, Yuan et. al. found by adding thieno[3,4-c]pyrrole-4,6-dione (TPD) moieties to the molecule increased the biradical character due to a longer conjugation length[75]. In OFET devices made from molecules with 0 or 1 TPD monomers, semiconductor like behavior was observed. However, for molecules with more than 2 TPD monomers, drain current depended little on gate voltage, and remained high regardless of the gate voltage. Due to the biradical character, interesting electronic properties have been reported of quinoidal structures, such as charge stabilization and ambipolar behavior[73,76,77]. Not only do quinoidal molecules form high performing n-type OSCs, but novel device behaviors may also arise from the unique electronic structure. Despite these intriguing electronic properties, polymorphism in quinoidal molecules has been rarely studied. Only a few reports have discovered crystal polymorphs in these quinoidal systems through serendipity[69,78,79]. Many aspects remain unexplored such as what is the complete polymorphic phase space for such molecules, the relationship between polymorphs and the resultant optoelectronic properties and finally, how the biradical forms interplay with polymorphism.

In this work, we report the discovery of remarkably prolific polymorphism exhibited by 2 dimensional quinoidal terthiophene and demonstrate the ability to drastically tune the electronic properties through controlling polymorphism. We employ 2DQTT-o-B[69,70,80] as a model system which is a high performance n-type semiconductor with reported electron mobility as high as 4.2 $cm^2 V^{-1} s^{-1}$. Using solution printed films, we observe a total of 5 distinct polymorphs and their phase transitions under cross polarized optical microscopy (CPOM) and resolved the unit cell structures with in situ grazing incidence X-ray diffraction (GIXD). The printed films of each polymorph are evaluated for their optical properties and electronic performance to find drastic modulation of the electron mobility, threshold voltage and bandgap across the polymorphs. We further perform in situ temperature-dependent device measurements and UV-vis absorption spectroscopy, which suggest that electronic and optical properties are influenced by a biradical character stemming from the unique quinoidal electronic structure. To our knowledge, this is the first time a polymorph-property relationship for quinoidal n-type semiconductors has been uncovered. Moreover, mobility modulation over 5 orders of magnitude along with dramatic changes to optical properties have rarely been reported.

2.3 RESULTS AND DISCUSSION

2.3.1 Polymorph discovery and mapping

We discovered a total of five distinct polymorphs of 2DQTT-o-B (**Figure 2.1a**) by a combination of DSC (**Figure 2.1b**), printing parameter screening (**Table S1**), in situ optical microscopy during thermal annealing (**Figure 2.2**) and GIXD (**Figure 2.3**). Based these data, discussed later, a complete map of the polymorph transition behavior is summarized in **Figure 2.1c**. Two main morphologies were obtained directly from the printing process. One case with tiny (<5 µm), misoriented domains was produced via printing at room temperature (~25 °C) from chloroform, dichloromethane, and toluene at moderate to fast speeds (0.1 – 50 mm s^{-1}), along with spin coating from those same solvents. The second morphology was obtained via printing from chlorobenzene at 85 °C at moderate speeds (0.1-0.5 mm s^{-1}), which exhibited significantly larger domains in this range, while at faster (>1 mm s^{-1}) speeds the solution appeared to dewet and would not deposit a film. These different morphologies initially suggested potentially 2 different polymorphs, which was confirmed via grazing incidence X-ray diffraction (GIXD). In both cases, upon annealing to 100 °C, the films converted to the same polymorph, evidenced by equivalent diffraction patterns along with changes in birefringence and color under POM. We designated this as polymorph I, the stable room temperature polymorph and later observed direct access to polymorph I at printing speeds <0.1 mm s^{-1}. We designated the aforementioned polymorphs obtained prior to annealing as I′ and I′′ respectively, as they were both metastable relative to polymorph I across the temperatures explored (25-230 °C). Further annealing polymorph, I induced two additional polymorph transitions (at 152°C and 210°C) observed by in situ polarized optical microscopy and in situ GIXD. These transitions were found to be reversible and were named as polymorph I-II and II-III transitions. All but polymorph I′′ are also observed in power samples, with the same polymorph transition characteristics revealed by DSC. A complete set of parameters for each polymorph, and transition map is compiled in **Table S1 and Figure 2.1c**. Below, we discuss the DSC, in situ optical microscopy and GIXD in detail to unveil the thermodynamic relationship and the structural characteristics of all five polymorphs, I′, I′′, I, II, III.

We first discuss DSC studies performed on as synthesized form I′ powder samples (**Figure 2.1b**). We observed the presence of 3 distinct solid-solid phase transitions prior to melting with onset temperatures of 110 °C, 167 °C and 234 °C. The first phase transition was exothermic in nature, suggesting by the heat of transition rule that polymorph I′ is metastable relative to polymorph I and that the I′-I transition is monotropic. On the other hand, The I-II and II-III were both endothermic, which likely indicates enantiotropic transitions based on the heat of transition rule, and as we will discuss later, are reversible phase transitions. After melting, however, the material appeared to have degraded and did not show reverse transitions for these polymorphs.

We were able to obtain both heating and cooling traces by heating only up to polymorph II or III to avoid degradation during melting (**Figure A1**). This allowed us to isolate and compare I-II and II-III transition behaviors. Interestingly, during the cooling process, the II-III transition showed a massive hysteresis, 78 °C, indicating a large free energy barrier to transition with a midpoint temperature of 185°C (**Figure A1a**). Due to this large hysteresis, rather than two discrete cooling transitions for the III-II and II-I transitions, we only observed a single transition, which may represent either a direct III-I phase transition, or both transitions occurring in rapid succession. In contrast, the I-II transition showed only 6 °C of hysteresis and a much smaller free energy barrier and a midpoint temperature of 160 °C (**Figure A1b**). Overall, both transitions are reversible and exbibit enantiotropic relationship, consistent with the inference from the heat of transition rule discussed above.

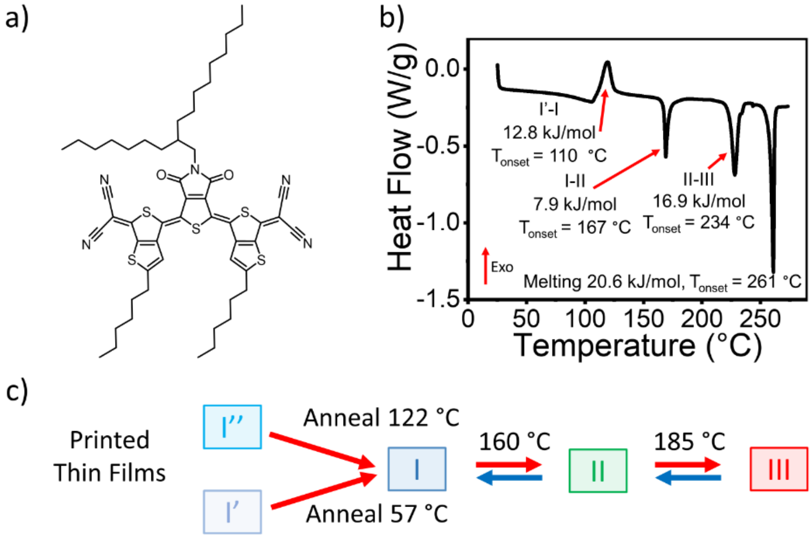

Figure 2.1. Molecular structure of 2DQTT-o-B (a) and DSC scan (b) showing 3 phase transitions in the powder sample at 10 °C min^{-1}. Summary of the transition pathways based on DSC, in situ POM and GIXD (c). Temperatures indicated are the onset temperatures for the irreversible transitions and the midpoint temperature from DSC for the reversible transitions. For printing conditions, see **Table S1**.

We next applied in situ cross polarized optical microscopy (CPOM) on printed thin films to visualize the polymorph transitions. A meniscus-guided coating process was adopted to obtain thin films of 2DQTT-o-B coated from chloroform. Using CPOM, we observed three solid-state phase transitions in thin films with similar behavior to those found in DSC (**Figure 2.2a-c, Movie A1-3**). By following the change in color (hue value) during the videos, we could extract onset temperatures for these transitions to be 57 °C, 152 °C and 210 °C (**Figure 2.2e-g**), that appear to correlate to the I’-I, I-II, and II-III transition, respectively. However, these onset temperatures differ significantly from the DSC measurements on powder, likely due to confinement effects within the film[35].

During the I’ to I transition (**Figure 2.2a**), while the intensity does not change as significantly, we do see slight growth of domain size, which suggests a crystallization process, which we confirm later via GIXD. For the I-II transition (**Figure 2.2b**) , there is an obvious shift in color to deeper reds, suggesting a change in how the refractive index varies with incident wavelength. The II-III transition, on the other hand, exhibits a significant change in birefringence, which is clearly indicated by the extreme brightness of polymorph III. This would suggest a much higher anisotropy to the refractive index, relative to polymorphs I', I and II, which we expect will dramatically change the optical and electronic properties of the film.

To our surprise, when printing films from chlorobenzene, we observed a new polymorph, designated I''. Films of form I'' exhibit clear differences from I' in morphology (**Figure 2.2a,d**). Mainly, polymorph I'' appears to have significantly larger domains and present a high degree of alignment, compared to polymorph I'. Similar to the II-III transition, upon heating, we see substantial decrease in intensity as polymorph I forms. Annealing isotropic films of polymorph I' results in isotropic domains of polymorph I (**Figure A6a,b**). Likewise, the alignment of polymorph I'' is templated onto polymorph I upon annealing induced I''-I transition (**Figure A6c,d**). This alignment in polymorph I was confirmed via GIXD, where peaks observed in isotropic films produced by annealing films of polymorph I' are missing in films annealed from polymorph I'' (**Figure A7**).

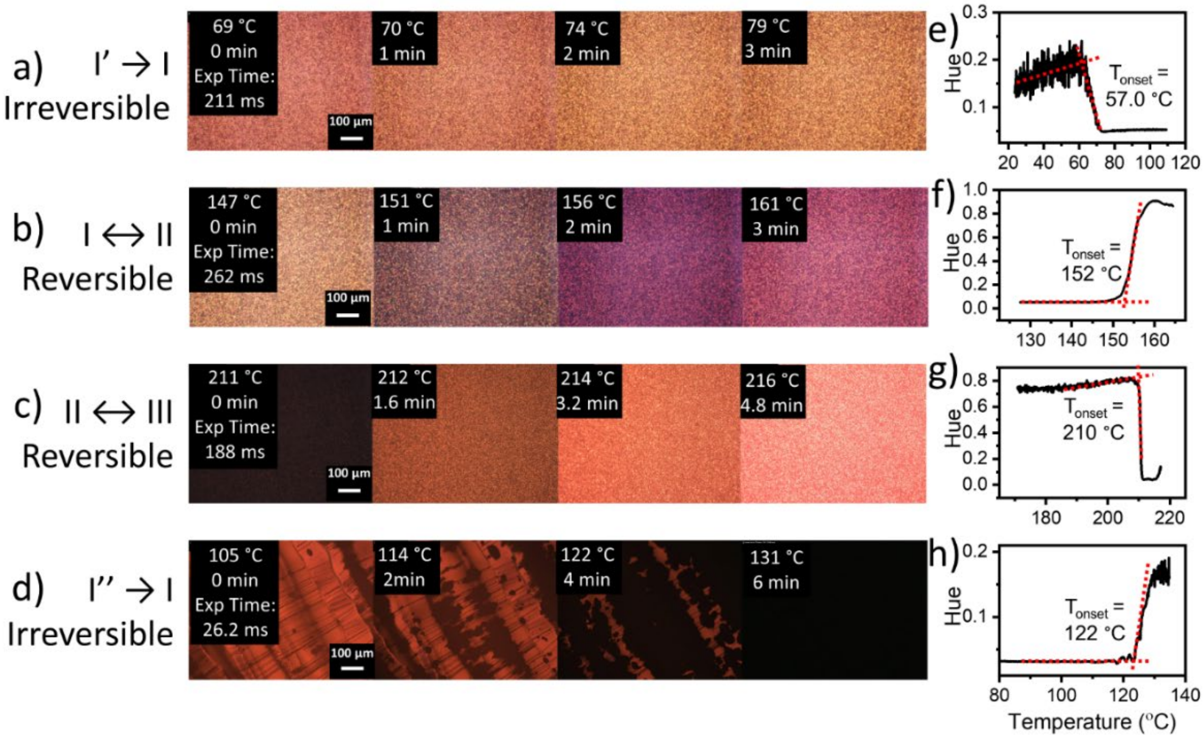

Figure 2.2. In situ polarized optical microscopy of thin film phase transition with increasing temperature. (a-d) in situ CPOM images of the I’-I, I-II, II-III, and I’’-I phase transitions respectively corresponding to **Movie A1-4**. Films were printed at 0.3 mm/s from chloroform (polymorph I’) or Chlorobenzene (polymorph I’’). Each video was recorded at 5 °C/min and at 1 frame per second. (e-h) show the change in color (hue value, defined as a value between 0-1) during the phase transition extracted from the CPOM images using a Python program.

2.3.2 Structural characterizations.

Using single crystal X-ray diffraction (SCXRD) and in situ grazing incidence X-ray diffraction (GIXD), we obtained the crystal structure of polymorph I and we confirmed I’ and I’’ were separate polymorphs and both transition to the same polymorph I as expected. While at room temperature, the alkyl chains were quite disordered, the core was resolvable and revealed 2DQTT-o-B packs in layers of 1 dimensional π stacks along the b-direction with a $C_{2/c}$ symmetry (**Figure A2a-b** and see **Crystallographic Information File**). Using GIXSGUI, we confirmed polymorph I and the single crystal had the same packing by overlaying the simulated diffraction pattern, with the $C_{2/c}$ symmetry, on the measured diffraction pattern for polymorph I (**Figure A3**).

Each layer is separated by alkyl chains and the molecules tilt at a 67° angle with respect to the substrate (bc-plane) consistent with the β-angle of the unit cell.

Using the single crystal unit cell as a starting point, coupled with GIXD (**Figure 2.3a-e**), we were able to calculate the expected unit cells for polymorphs I'', I and II (**Figure 2.3f-i**)[81]. The parameters for each unit cell are summarized in **Table 1.** We found fitted unit cell for polymorph I matched closely with the unit cell from SCXRD. Tackling the polymorph III fit posed a unique challenge due to the low number of diffraction peaks observed, so we turned to simulating the positions of the diffraction peaks using GIXSGUI[82]. Due to the rectangular like pattern presented, we realized there would likely be a higher symmetry and through a process of elimination uncovered the trigonal unit cell. We did this by using the rectangular cell as a starting point and adjusting the cell parameters until the simulated and experimental patterns overlaid perfectly and accounted for all visible peaks. Finally, we confirmed our unit cell fitting via simulating the diffraction patterns and plot the simulation on the measured diffraction pattern (**Figure A4a-d**). We found the unit cells matched with quite good agreement between the fitted cell and the single crystal structure.

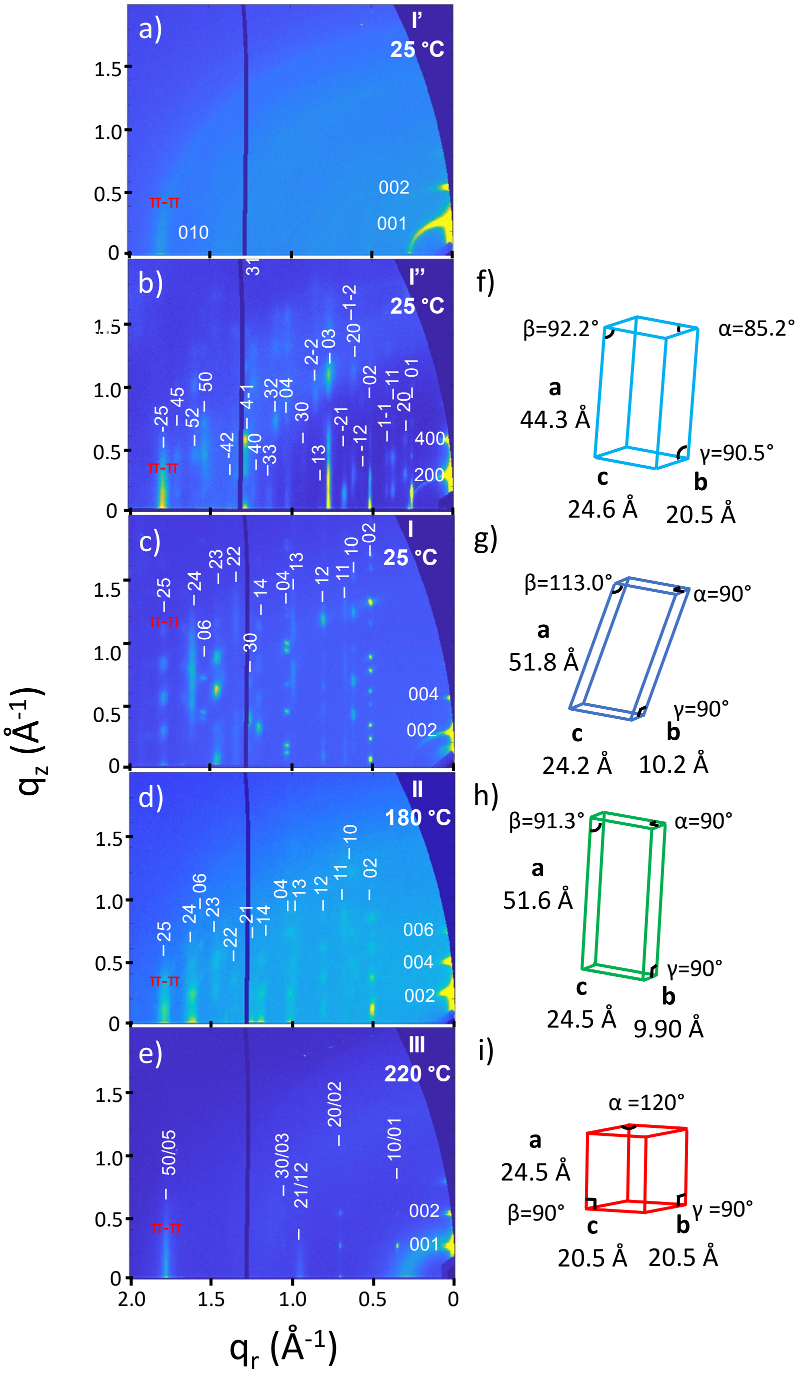

Figure 2.3. GIXD signatures and unit cells for each polymorph. (a-e) Indexed GIXD patterns based on the unit cells calculated for each polymorph respectively. (f-i) unit cells representing the GIXD patterns. A full simulation of the diffraction patterns can be found in **Figure A4**.

Table 2.1. Comparison of unit cell structure across each polymorph.

	I′	I′′	I (SCXRD)	I (GIXD)	II	III
Temperature (°C)	25	25	25	25	200	221
a (Å)	--	44.3	50.5	51.8	51.6	24.5
b (Å)	--	20.5	10.2	10.2	9.90	20.5
c (Å)	--	24.6	24.1	24.2	24.5	20.5
α (°)	--	85.2	90	90	90	120
β (°)	--	92.2	113	113	91.3	90
γ (°)	--	90.5	90	90	90	90
Volume (Å^3)	--	22316	11396	11216	12460	8918
π-π stack distance (Å)	3.53	3.52	3.59	3.56	3.45	3.58

Beginning with the I′-I transition, polymorph I′ clearly exhibits a highly disordered phase. The diffraction pattern only shows lamella out of plane stacking and an in plane π-π stacking peak at 3.53 Å, indicated by the intense rod in the 1.7-1.8 Å-1 region. Polymorph I, in contrast, is highly crystalline, confirming a crystallization process during the I′-I transition, suggested by in situ POM previously. Upon crystallizing polymorph I, we observe a monoclinic crystal system form. Specifically, we noticed the (h01) rod did not appear near q_r = -0.25 Å^{-1} as expected based on the unit cell simulation (**Figure A4b**), consistent with the $C_{2/c}$ symmetry of the single crystal structure. Unlike polymorphs I′ and I′′, there is a full Bragg rod in the location where we would expect the π-π stacking peak near q_r=1.76 Å^{-1}, representing a π-π stacking distance of 3.56 Å. This value was consistent with the measured 3.59 Å measured from the single crystal structure (**Table 1**). To confirm our expectation that this rod represents the π-π stacking, this Bragg rod was indexed to (h25) and the ($\bar{4}$25) peak, which appears at the horizon, has been associated with the π-π stacking direction (**Figure A2c-d**). This indicates the π-π stacking now has long range order in the out of plane direction, which is not present in polymorphs I′ and I′′. Moreover, we measured the π-π stacking distance based on the single crystal structure and found this to be 3.59 Å, was quite consistent with our GIXD result of 3.56 Å (**Table 1**).

Polymorph I′′, on the other hand, exhibits crystalline packing with a triclinic unit cell (**Figure 2.3b,f**). A strong π-π stacking peak was also observed at 3.52 Å, a very similar distance to that of polymorph I’ discussed previously. Upon phase transition to polymorph I, significant changes to the unit cell, and thus packing, are necessary to form the monoclinic polymorph I. Specifically, we see a halving of the b direction, which related to the formation of the c glide plane. These packing changes are consistent with the large decrease in birefringence during the I’’-I transition.

During the I-II transition, we observe preservation of the monoclinic crystal system. In fact, the systematic absences observed in polymorph I persist, suggesting a similar symmetry, and thus relatively small packing changes (**Figure 2.3c-d, Movie A5**). The Bragg rod positions change very little between polymorphs I and II in the q_r direction. Instead, the major packing changes occur in the out of plane position of the peaks, which is reflected in the change in the β angle, which appears to be associated with the molecular tilt. This suggests the molecules tilt up to stand upright with respect to the substrate, much like changing the tilt of a deck of cards standing on end. Moreover, we observed a significantly smaller π- π stacking distance compared to polymorph I, likely linked to the change in molecule tilt. The structural similarity between polymorphs I and II is consistent with the small birefringence change under CPOM.

The II-III transition, in contrast to the I-II transition, shows dramatic changes to the packing. Polymorph III shows a radically different diffraction pattern compared to polymorph II, resulting in an entirely new crystal system and packing. We observed many of the Bragg rods from polymorph II disappear (**Figure 2.3d-e**, **Movie A6**), resulting in a distinct rectangular diffraction pattern. The disappearance of the rods suggests a higher packing disorder and/or a significant increase in symmetry of the crystal structure, to form a hexagonal unit cell (**Figure 2.3i**). Polymorph III exhibited 2 a Bragg rod near $q_r = 1.75$ Å^{-1} corresponded to a π-π stacking of 3.58 Å, increasing the π-π distance substantially from polymorph II. As expected from the large changes in intensity under in situ POM, the II-III transition exhibits extensive changes to the molecular packing.

2.3.3 Optical and electronic properties

In order to investigate the optical properties, we employed in situ UV-Vis absorption spectroscopy to probe the electronic structure transition during thermal annealing of thin films. For polymorphs I′ and I′′, films were measured as printed from chloroform and chlorobenzene with thicknesses of 51.3 nm and 59.8 nm respectively, as discussed in the methods section (**Figure A8**). To obtain polymorphs I, II and III, the film of I′′ was annealed for 1 hour in the glove box at 100 °C, and then heated, using a resistive heater setup, to the corresponding temperature for each polymorph (25 °C, 170 °C, 219 °C respectively). Upon comparison of each polymorph, we observed dramatic changes in the absorption behavior.

Polymorphs I′ and I′′ both exhibited relatively broad vibronic peaks, that upon transition to polymorph I become significantly sharper (**Figure 2.3a,b**). This is consistent with reduced paracrystalline disorder upon I′-I and I′′-I transitions measured by GIXD when we observed formation of sharp higher order peaks in place of a diffuse, broad π-π stacking streak during both the I′-I and I′′-I transitions (**Figure 2.3a-c**). Along with the reduction in peak width, both the I′-I and I′′-I transitions show substantial increases to the optical band gap (+0.19 eV and +0.15 eV, respectively) shown in **Table 2**. Polymorph II, on the other hand, exhibits only modest changes from polymorph I (**Figure 2.4c,d**). This is in line with only slight structural modifications accompanying this transition by GIXD (**Figure 2.3c,d**) and relatively small changes to birefringence under POM (**Figure 2.2b**). These small changes in structural and optical behavior were also reflected in the modest changes to the optical bandgap between polymorphs I and II (-0.07 eV). This is in stark contrast to the formation of polymorph III, where there is a dramatic broadening and redshift in the absorption spectra, resulting in the lowest bandgap at 1.18 eV measured out of any of the polymorphs, showing a substantial decrease from polymorph II (-0.15 eV) (**Figure 2.4e,m**). In fact, looking at an overlay of the spectra (**Figure 2.4k**), we see similarities in the peak positions between polymorph III and polymorphs I′ and I′′. As discussed previously, these broadened lower energy peaks are likely the result of paracrystalline disorder. Likewise, with polymorph III, we observe the formation of a broad π-π stacking peak and a reduction in the long-range order of the film, exhibited by the reduction in diffraction peaks past -1 Å^{-1} (**Figure 2.3e**), which may account for the broadened optical absorptions. As discussed previously, this disorder would be consistent with increased motion in the alkyl chains at high temperatures.

For evaluating the corresponding electronic properties of each polymorph, a bottom gate top contact (BGTC) OFET structure was fabricated, as specified in the methods section. Films of I’ and I’’ were printed from chloroform (room temperature, 0.1-50 mm s^{-1}) and chlorobenzene (85 °C, 0.1-0.3 mm s^{-1}) respectively, as discussed in the methods. For a LUMO level of -4.44 eV, we chose to deposit gold contacts with a work function of 5.3 eV. Polymorph I devices were obtained via annealing the aforementioned devices in a glovebox for 1 hours at 100 °C and allowed to cool to room temperature. Polymorphs II and III were stabilized using a resistive heater to reach the temperatures that stabilized the respective polymorphs, 170 °C and 195 °C. We note that during device measurements, we determined the II-III transition occurred at a temperature significantly lower than observed under in situ POM and GIXD. There are 2 possibilities for this discrepancy. The first cause may be kinetic, as we must hold the devices at each measured temperature for a long period of time to stabilize the temperature (approx. 30 minutes), and the time it required to measure each of 6 devices (approx. 30 minutes). Holding the films at high temperatures for a long time, coupled with a large energy barrier, may result in a lower observed transition temperature given that the T sweeping rate is much faster for in situ POM and GIXD. Secondly, the introduction of an applied gate bias may lower the transition energy barrier, which would also result in a lower observed transition temperature.

Polymorphs I’ and I’’ exhibited poor current modulation by gate voltage modulation, with typical devices reported in **Figure 2.4f,g**. After measuring and analyzing 130 devices of I’ and 36 devices of I’’ we found that in most devices, no on-state was observed, even upon increasing the gate voltage up to 100V (see output curves in **Figure A9a,b**. Correspondingly, the electron mobilities extracted from transfer curves in the saturation regime are low, which are (3.68 ±2.77) 10^{-4} $cm^2V^{-1}s^{-1}$ and (1.16 ±0.91) 10^{-3} $cm^2V^{-1}s^{-1}$ for polymorphs I’ and I’’ respectively (**Table 2, Figure 2.4n**). Moreover, the I’ devices appeared to exhibit threshold voltages across the measured voltage range and did not accurately represent the electronic characteristics. This may be due to the low modulation coupled with relatively large off current compared to other polymorphs (**Figure 2.4l**) As expected, based on the isotropic nature of polymorph I’, there was no difference in performance between devices fabricated with channels parallel and perpendicular to the printing direction (**Table S2**). Polymorph I’’, by contrast showed a relatively well-defined range for threshold voltage and an increased mobility by one order of magnitude which may be result of the high degree of alignment and increased ordering, relative to polymorph I. Despite the significant alignment of polymorph I'' (**Figure A6**), only a modest difference (by a factor of 2) was observed in the mobility between the 2 directions (**Table S3**).

Upon forming polymorph I via annealing through the I'-I and I''-I transitions, we effectively "turn on" the semiconducting properties of 2DQTT-o-b (**Figure 2.4h**). Polymorph I performs with a much higher mobility of 0.22 $cm^2V^{-1}s^{-1}$, and exhibits clear on and off states. Moreover, the irregular output behavior from polymorph I' seems to disappear upon annealing to polymorph I (**Figure A6c**). Such large changes in electronic properties are consistent with the extensive crystal structural changes previously discussed. On the other hand, devices formed from aligned I'' films only showed moderate anisotropy in the device mobility (**Table S5**). This may be a result of the crosshatched packing motif in polymorph I resulting from the 1-dimensional π-stacks discussed previously. Such packing motif may allow for efficient charge transfer pathways along both in plane directions (with respect to the substrate).

We stabilized 5 devices of polymorphs II and III at high temperatures and observed a unique device characteristic, further adding to the mysterious behaviors in 2DQTT-o-B (**Figure 2.4i,j,n**). Unlike polymorphs I' and I'' that did not appear to have a defined "on" state, polymorph II resisted turning off, even when sweeping down to -60V. Measurements below -60V were avoided due to a propensity for the devices to burn at the higher temperatures. Compared to polymorph I, polymorph II exhibited a significantly decreased mobility (1.67 ± 0.11) 10^{-2} $cm^2V^{-1}s^{-1}$, and a largely shifted threshold voltage of -64 V (**Table 2**). Such a characteristic in the transfer curve would signify a drastic increase in the population of charge carriers in the off state. As we will discuss later, we attribute this device characteristic to a thermally driven quinoidal-to-aromatic population shift that yielded biradical charge carriers at higher temperatures independent of the structural transition. At the same time, we observed a dramatic drop in on current by an order of magnitude that is attributable to the I-II structural transition.

The II-III transition, however, dramatically reduces the electronic performance to exhibit very low current and minimal gate voltage dependence (**Figure 2.4J**). The II-III transition results in a mobility decrease of 3 orders of magnitude, to (5.63 ± 4.75) 10^{-5} cm^2 V s^{-2}(**Table 2**). This low mobility is consistent with the drastic structural transition and the loss of long-range order observed from GIXD and in situ POM and broadening of the absorption peaks discussed previously. Once again, no on state is observed for this polymorph and presented both little to no current modulation across gate voltage.

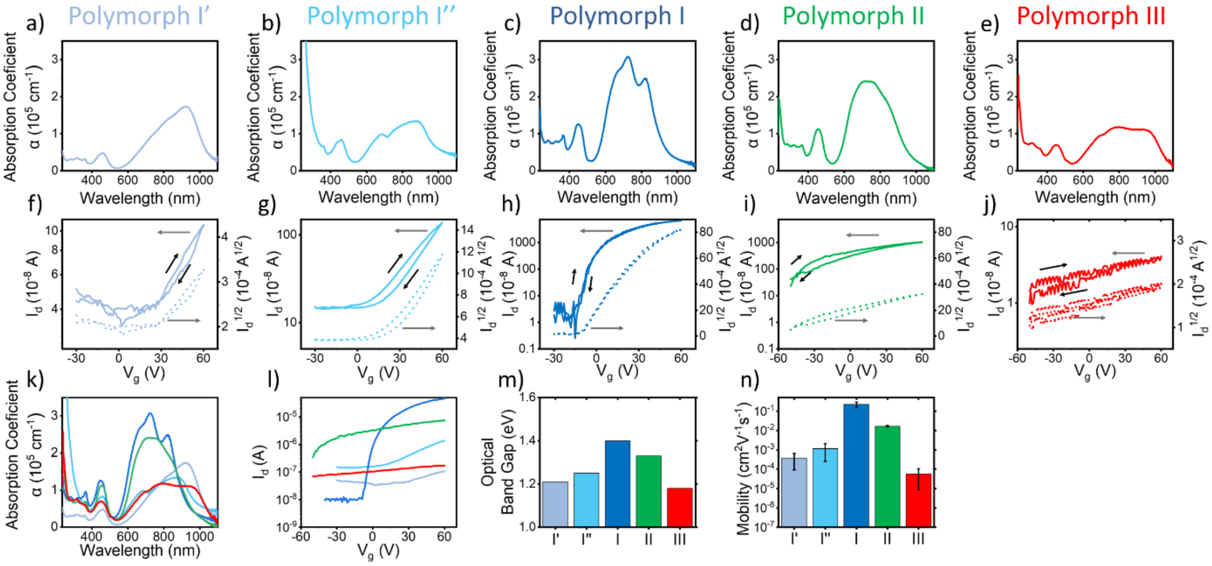

Figure 2.4. Optical absorption spectra and field-effect transistor device performance for each polymorph. Each polymorph I’, I’’, I, II and III are colored grey-blue, light blue, dark blue, green and red respectively. (a-e) Individually plotted absorption spectra for each polymorph. Polymorphs I’, I’’ and I are shown under room temperature conditions. Polymorphs II and III were measured at 170 °C and 219 °C respectively. (f-j) Transfer curves showing changes in device performance with polymorph. Polymorphs I’, I’’ and I were measured at room temperature. (k, l) Comparison of absorption spectra and transfer curves across polymorphs. (m, n) Optical bandgap and mobility comparison across polymorphs. Polymorphs II and III were measured at 170 °C and 195 °C, respectively. Each device was measured at a V_{ds} = 60V.

Table 2.2 Optical and electronic properties of five polymorphs.

Polymorph	Mobility ($cm^2 V^{-1} s^{-1}$)	V_{th}(V)	I_{on}/I_{off}	E_g(eV)
I'	(3.68 ±2.77) 10^{-4}	N/A	N/A	1.21
I''	(1.16 ±0.91) 10^{-3}	-10.1 ± 13.7	N/A	1.25
I	(2.23 ±0.66) 10^{-1}	-17.6 ±5.8	10^4	1.40
II	(1.67 ± 0.11) 10^{-2}	-63.5 ±1.7	10^2	1.33
III	(5.63 ± 4.75) 10^{-5}	N/A	N/A	1.18

2.3.4 In situ investigation of optical and electronic properties

We next performed in situ measurements at incremental temperatures up through each transition to elucidate how polymorph transitions directly impact optical and electronic properties (**Figure 2.5**). We obtained a film of polymorph I by annealing the I’ film as described in the methods, and then systematically heated the films to observe how the optical and electronic properties evolved with increasing temperature. Upon heating of polymorph I thin film but prior to the I-II transition, the 0-0 relative peak intensity decreases while the 0-1 peak rises slightly, forming an isosbestic point in the spectra suggesting thermally controlled populations of 2 different species in the film (**Figure 2.5a**). This pre-transition region requires more than polymorphic transitions to understand. Corresponding to the optical spectra change is the large negative shift in threshold voltage in the same pre-transition region during in situ device measurements (**Figure 2.5e**). At the same time, we observed a slight increase in electron mobility coupled with an increase of the on-current as the temperature increased in the absence of any polymorphic transitions (**Figure 2.5d,h**), though this increase is within the range of error (**Figure A10**). The increase in mobility is likely a result of a hopping mechanism for charge transport. For the change in V_{th}, however, we ascribe this behavior to temperature-induced biradical formation as discussed later.

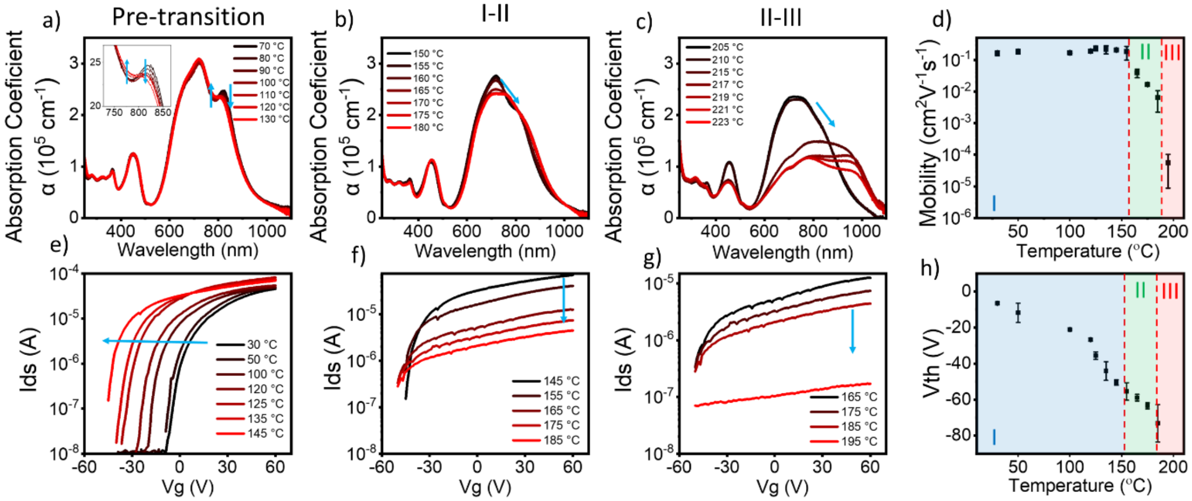

Figure 2.5. In situ investigation of optical and electronic properties as a function of temperature. OFET device transfer curve and absorption spectra for the pre-transition region (a,e), the I-II transition (b,f) and the II-III transition (c,g), representative of the 5 devices tested. The blue arrows indicate direction for increasing temperature, from black to red. Temperature dependent plots for mobility (d) and threshold voltage (h) extracted from the transfer curves. The regions are separated into where polymorph I (dark blue), II (green), and III (red) form upon heating.

In stark contrast to the gradual pre-transition changes, during the I-II phase transition, there is a sharply defined change across the transition temperature of 152 °C, as expected for first-order transitions. For the I-II transition, we observe a sudden drop in the on-current of the devices. This decrease is associated with a clear drop in the electron mobility and slight redshift in the 0-0 peak and decrease in optical bandgap, (**Figure 2.5b,f**). Important to note, we see a "breaking" of the isosbestic point just prior to the phase transition, signifying multiple species are now present – possibly charged species as a result of self-doping to be discussed later. The I-II transition exhibits a sudden decrease in mobility and after the onset of the transition, the mobility further decreases with increasing temperature (**Figure A10**). This trend clearly distinguishes from the slight rising mobility trend prior to the I-II transition, which is solely caused by temperature increase. Surprisingly, despite the disappearance of the isosbestic point and the abrupt change in on-current and mobility, we see a disconcertingly linear trend in the threshold voltage across the I-II transition, suggesting the threshold voltage was unaffected by the phase transition (**Figure 2.5d,h**). Upon returning the device to room temperature from polymorph II, (**Figure A11, Table A5**), we see a recovery of the device performance. However, the threshold voltage remains lower than the initial device, likely due to a long lifetime of residual biradicals.

A similar scenario is shown by the II-III transition, where a second discrete change in the absorption spectra occurs across the transition temperature of 210 °C (**Figure 2.5c**). This transition results in red shift of the 0-0 peak as discussed previously. Different from the I-II case, the absorption spectra continue to evolve post transition, as the 0-0 peak continuously decreases in intensity, possibly due to weakening of the molecular interactions at such high temperatures. As polymorph III forms, we observe another sudden decrease in the on current, this time by 2 orders of magnitude (**Figure 2.5g**). At this point, the transfer curve becomes quite linear, showing no clear on and off states. As a consequence, the mobility also decreases by 3 orders of magnitude and due to the lack of on and off states, a threshold voltage is no longer measurable. Above 195 °C, no signal from the devices is observed, and we note that while our in-situ POM experiments investigating polymorph III films appear to show fully connected thin films (**Figure 2.2c**), over the longer timeframe of the device measurements, sublimation may have resulted in the elimination of device performance at temperatures above 195 °C.

2.3.5 Discussion

The DSC and in situ CPOM data provide a clear picture of the polymorphic phase space which can be summed up in the qualitative free energy diagram (**Figure 2.6**) to represent the thermodynamic relationship among the five polymorphs discovered. Both polymorphs I' and I'' were obtainable at room temperature and underwent irreversible phase transitions to polymorph I. This behavior suggests both I' and I'' are metastable to polymorph I within this temperature range and have a monotropic relationship to polymorph I. This inference is consistent with the heat of transition rule where I'-I transition is exothermic in DSC measurements. In contrast to a highly crystalline polymorph I'', polymorph I' exhibits a distinctively disordered phase, showing only lamella and π-π stacking based on the GIXD pattern. We therefore infer that polymorph I' is the highest free energy (most metastable) form followed by polymorph I''. Given the absence of interconversion between I' and I'', we illustrate their free energy curves with no cross-over within the T range studied. Polymorphs I and II, II and III exhibit a clear enantiotropic relationship, shown by the reversible nature of the two transitions. The free energies of these polymorphs cross at the respective transition temperatures, extracted from DSC as the midpoint temperature between the forward and reverse transitions.

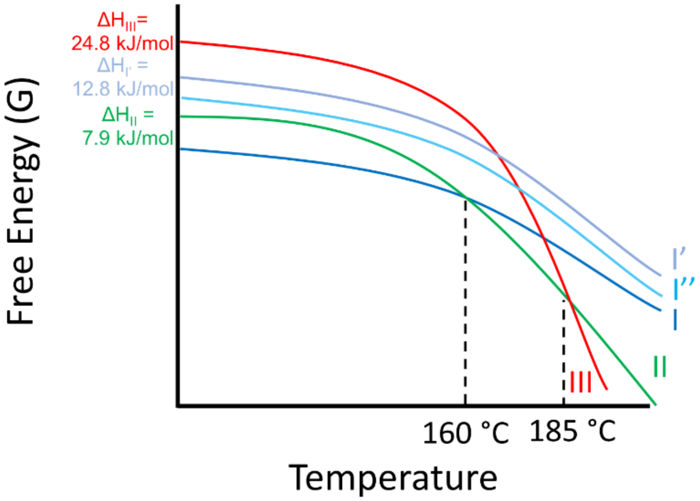

Figure 2.6. Proposed qualitative free energy diagram illustrating the polymorphic phase space of 2DQTT-o-B thin films. Enthalpy differences are based on polymorph I, extracted from the DSC enthalpy of transition. The transition temperatures are the midpoint temperatures between the heating and cooling onset temperatures for each transition.

Based on the unit cells extracted from GIXD, we have been able to gain insight into how the crystal packing may change between polymorphs. We confirmed that I’ appears highly disordered, leading to the irreversible crystallization process from I’ to I. Based on the unit cells obtained, we expect polymorphs I and II to be monoclinic structures and polymorph III may pack in a trigonal crystal structure. While the specific space groups are difficult to assess from GIXD, we can at least see a trend of increasing symmetry as we increase in temperature. Particularly interesting is the I to II transition where the differences in the unit cell were relatively small, mostly changing the angle of β. This together with a small transition temperature hysteresis suggests a possible displacive, martensitic transition[53,55,56] which we are investigating further in a separate work. Despite the small unit cell change, we see a significant decrease in the π-π stacking distance from I to II, associated with a decrease in the length of the b axis, which may also be associated with a change in tilt of the molecules. Overall, in the same system, we can observe a rich diversity of polymorphic flavors: from a disordered polymorph I’, a highly aligned triclinic I’’, highly similar polymorphs I and II, to a high symmetry polymorph III. With such diversity of polymorphs, we are offered a unique opportunity to show how these forms drastically tune the optoelectronic properties via structure control.

And indeed, we see these drastic changes in properties such as switching the optical band gap and tuning electron mobility across 4 orders of magnitude. Polymorph I’, as cast, exhibited a low mobility on the order of 10^{-4} cm^2 V s^{-1} which was modestly improved by one order of magnitude via accessing a highly aligned, ordered, metastable form, I’’. However, neither of these polymorphs exhibited long range order in π-stacking, which we expect prevented efficient charge conducting pathways, and in part resulted in much lower performance than a highly crystalline polymorph I. Moreover, we observed the packing of polymorph I exhibited layers of 1-dimensional π-stacks, which would facilitate those efficient pathways in polymorph I. This is coupled with stacks that alternate tilting direction of the molecules, consistent with the c glide symmetry that likely allows for charge transfer in both the b and c directions. For the changes in the electronic properties of the thermally accessible polymorphs II and III, we require a deeper look into what else is occurring during the transitions. Here we see a decrease in mobility of one order of magnitude and a large negative shift in threshold voltage. Surprisingly, this was quite counter intuitive when considering the structural changes. As previously discussed, polymorph I and II had the smallest differences in unit cells, mainly from changes in the tilt of the molecules and a substantial decrease in the π-π stacking distance. But we must wonder, what would be doping the film with charges upon stabilization of polymorph II?

To begin answering this question requires in situ conditions. We found this threshold voltage change began, in fact, far before the I-II transition. Measuring across the temperature range, we see a monotonic negative shift, strongly correlating with temperature alone. Specifically, at the I-II transition, the negative shift appears to continue in quite a linear fashion, unlike the discontinuous drop in mobility expected from first order phase transitions. Next, we looked at the optical behavior in this pre-transition region, which showed a matching constant shift of the absorption spectra about an isosbestic point, providing further evidence that a new species may be doping the film induced by temperature. This seems to suggest a mechanism similar to that seen in similar molecules resulting in a self-doping effect. This effect was originally reported by Zhang and Wudl et. al., showing a stabilization of charges in the presence of high biradical concentrations, with a strong temperature dependence in similar diradicaloid systems[12,77,83]. They found that systems with a significant population of biradicals would result in doping of OFET based devices. Upon heating from -60 to +60 °C, this doping effect increased resulting in a shift of the threshold voltage while having little impact on the measure mobility, consistent to the observations reported here. This effect would also explain the behavior of cooled devices that retain a slightly shifted threshold voltage after cooling as a lingering population of stabilized charges. Recently, Dafei et. al. showed the small, but measurable concentration of biradicals in a similar 2DQTT system[75]. We suggest that increasing temperature may increase the population of the biradical state which may readily stabilize extra charge carriers causing this negative shift in threshold voltage - a hypothesis to be investigated in our future work.

While polymorphs I and II presented quite interesting electronic behavior, polymorph III offered an exotic crystal structure tied to major changes in absorbance spectra. Yet, this polymorph exhibited extremely low electrical conductivity, no on/off behavior, reducing the electron mobility to the point of being unmeasurable. While we did suggest potential issues with film sublimation after being held at high temperatures for a long time, however at short time scales, it appears the film remains intact as evidenced in **Figure A12**. Under the optical microscope used in tandem with the device measurement, we can clearly see at higher temperatures the film remains, and the film takes on a reddish tinge, associated with the II-III transition. At the same time, during our in situ POM experiments, films of polymorph III still appear to be connected and do not clearly suffer from sublimation on short time scales (~20 minutes of heating), suggesting the reduced performance is indeed the property of polymorph III instead. Perhaps, the trigonal packing mode prevents efficient charge transfer paths to form over the long distances by breaking these 1-dimensional π-stacks. We are left with an enigma of sorts, a structure that behaves quite atypical compared with other electronic materials.

2.4 CONCLUSIONS

Our work has discovered a surprisingly numerous set of polymorphs of 2DQTT-o-B which were accessed through a combination of film process conditions and temperatures. We used DSC, in situ microscopy and temperature-variant grazing incidence X-ray diffraction to fully capture the range of polymorphic structures and the transition behaviors. We were further able to utilize these structures to tune the optical band gap and radically shift the electron mobility across 4 orders of magnitude. Finally, we realized the optical and electronic properties changes may be closely related to the unique quinoidal molecular structure.

These n-type quinoidal structures have gone understudied in recent years and offer an area to significantly expand our understanding of structure-property relationships. We have systematically explored the polymorphic phase space of 2DQTT-o-B and discovered 3 previously unknown polymorphs within this system. We were able to extract unit cells for each polymorph to discover not only does 2DQTT-o-B present many polymorphs, but also a rich diversity in terms of structure and thermodynamic properties. Polymorphs I' appeared to be quite disordered whereas polymorph I'' was highly crystalline, induced only through solution shearing with chlorobenzene, but both were metastable polymorphs at room temperature irreversibly transitioning to polymorph I – the stable polymorph at room temperature. We also discovered reversible thermally induced transitions of polymorph I to II and polymorph II to III. Moreover, we observe the typical trend of increasing crystal symmetry from low to high temperature polymorphs, culminating in a trigonal crystal system in polymorph III which is very unusual for organic semiconductors.

The diverse polymorph structures offered drastic tunability of optical and electronic properties. We observed relatively low electron mobility in the metastable polymorphs I’ and I’’ (on the orders of 10^{-4} and 10^{-3} $cm^2\ V^{-1}\ s^{-1}$, respectively), which increased by 2 or 3 orders of magnitude, respectively, by annealing the films and transforming to polymorph I. Upon heating these devices through the I-II transition, we decreased the mobility from 0.23 to 0.017 $cm^2\ V^{-1}\ s^{-1}$, and simultaneously reducing the threshold voltage by 45 V. Finally, by heating to polymorph III, we were found little dependence of the current on the gate voltage, further reducing our mobility by 3 orders of magnitude to 5.6×10^{-5} $cm^2\ V^{-1}\ s^{-1}$. Upon close examination of the thermally induced phase transition via in situ techniques, we observed a consistent negative shift in threshold voltage and an isosbestic point in the absorption spectra which might results from a thermally induced population of biradical states. How biradical formation impacts polymorphism is an intriguing question that remains to be answered in our future work. The combination of both the prolific polymorphism and unique electronic structure of quinoidal n-type organic semiconductors offers a tantalizing possibility to dynamically modulate electronic device properties from practically an insulator to a field-effect transistor.

2.5 MATERIALS AND METHODS

Materials synthesis. Synthesis of 2DQTT-o-B has been published previously[69].

Thin Film Preparation. Thin film samples of polymorph I’ and I’’ used for experiments described in this work were printed onto trichlor(phenyl)silane(PTS) treated 300 nm SiO_2/Si wafers using solution shearing from 6 mg/mL solutions dissolved in chloroform at room temperature and chlorobenzene at 85 °C, respectively. A shearing speed between 0.1-0.5 mm/s was used in both scenarios with a blade gap of 100 µm. To transition the films to polymorph I, these films would be annealed at 100 °C for 30 minutes in the glovebox, until completely converted. We were also able to produce polymorph I’ films from dichloromethane and toluene solutions. A full table of deposition conditions and outcomes are available in **Table S1**.

Polarized Optical Microscopy. The thin film samples were placed in a Linkam LTS420 heating stage under a Nikon H550S with an Infinity 1 camera. The heating stage was sealed, and heating was performed at 5 °C min^{-1}. The stage temperature was calibrated using a thermocouple to account for the difference in temperature between the resistive heater and the surface of the samples stage. Videos of the annealing process were taken at 1 frame per second under cross-polarizers and image analysis was performed using ImageJ and Python software. The software extracts an average value from a rectangular region of each frame for Intensity (average of RGB), R, G, B, (red, green and blue pixel values respectively) h (hue), s (saturation) , and v (value, or color) values. These values were then plotted across temperature which was interpolated for each frame using the beginning and end temperatures.

Single Crystal X-ray Diffraction. The single crystal structures were collected at NSF's ChemMatCARS (Sector 15) of the Advanced Photon Source, Argonne National Laboratory. Needle crystals grown via slow evaporation from 1:1 dichloromethane and ethyl acetate and measured at room temperature. The beam energy was 30 keV (0.41328 Å), and the beam size at the sample was 0.15 × 0.15 mm^2. 720 frames were taken using a Huber 3 circles diffractometer with a kappa angle offset of 60° and a Pilatus 1M (CdTe) detector. The sample to detector distance was 130 mm and was collected at 2 θ-angles at 0° and ω-angles at -180°, followed by two different kappa angles, 0° and 15° respectively. The ϕ-angle was scanned over the range of 360° using shutterless mode.

The cell refinement and integration of intensity data were carried out with the APEX3 software[84]. Face-indexed absorption corrections were performed numerically with SADABS[85]. For both low temperature and room temperature structures, the initial structure solution was solved with the intrinsic phasing methods SHELXT[86], and refined with the full-matrix least-squares SHELXL program[87]. Details for modeling the disordered alkyl chains are reported in the supplementary information and the structures were added to the Cambridge Crystallography Data Center with deposition number was 2064561. Structural information for the structure was in the **Crystallographic Information File**. The single crystal structure for 2DQTT-o-B was analyzed using Mercury software to produce **Figure A2** and measure the π-π stacking distance[88].

Grazing Incidence X-ray Diffraction and Unit Cell Determination. GIXD was performed at beamline 8-ID-E of the Advanced Photon Source at Argonne National Laboratory[89]. The data were collected at 10.91 keV on a 2D Pilatus 1M detector. Ex situ measurements were conducted for polymorphs I' and I'' under vacuum at room temperature. Films of I'' were annealed as discussed above to form polymorph I which was also measured under vacuum at room temperature. In situ thermal annealing measurements were conducted in a He environment with the sample on a commercial thermal stage (Linkam HFSX350-GI), with the temperature ramped at 10 °C/min and the exposure taken after equilibration at the target temperature for approximately 5 min. GIXD videos (**Movies A5,6**) were obtained via taking continuous exposures at a constant heating of 5 °C/min. GIXSGUI software was used to correct for detector nonuniformity, beam polarization and to reshape the 2D data into the representation q_z vs q_r[82]. The incident angle was set at 0.14° right above the critical angle for total reflectance of the organic thin film. Each peak was fit with a gaussian function to determine the peak positions. We then used a least square error fitting procedure (see also **Figure A4**) to determine best-fit unit cells for each polymorph on the basis of the experimental peak positions (see supp. Info). For the fitting, we defined the out of plane direction, with respect to the substrate, to be the direction of the *a*-axis. The fittings were then further fitted using GIXSGUI to simulate the diffraction patterns under different symmetries. The resulting unit cells were visualized using Vesta software[90].

UV-vis spectroscopy. Absorbance data were collected on an Agilent Cary 60 UV-Vis spectrometer within a wavelength range of 1100 to 200 nm. Polymorph I' was printed from chloroform onto PTS treated glass at 0.3 mm s^{-1} at room temperature. Polymorph I'' was printed from chlorobenzene at 0.1 onto PTS treated glass at 85 °C. To perform in situ measurements, a custom resistive strip heater, designed with an aperture in the center to allow for transmission UV-Vis measurement, was purchased from Rama Corp with 150W power output to heat the sample inside the UV-Vis spectrometer. Data was taken at intervals of 5 °C. The absorption coefficient was calculated by the equation

$$\alpha = \frac{2.303 * A}{t}$$

where A is the absorbance and t is the thickness. Thicknesses of the films were obtained from AFM, shown in **Figure A8**. The absorption coefficient was then used to make Tauc plots for each polymorph by plotting $(\alpha h\nu)^{1/2}$ vs. $h\nu$ where $h\nu$ is the energy of the light in eV. The optical band gap was calculated based on the onset of the Tauc plot by fitting a line to the onset and finding the x-intercept.

Field-effect transistor fabrication and measurements. Using the 6mg mL^{-1} solutions in chloroform and chlorobenzene, films of polymorphs I' and I'' were printed on PTS treated 300 nm SiO_2/Si wafer from chloroform at room temperature and chlorobenzene at 85 °C respectively. A series of speeds from 0.1 to 0.5 mm s^{-1} were used. Top contact bottom gate devices were fabricated using a shadow mask and thermally depositing gold electrodes directly onto the film at a thickness of 35nm (Kurt J. Lesker Nano 36). The channel length and width are 800 µm and 40 µm respectively.

The resulting devices were then measured under a nitrogen atmosphere using a Keysight B1500A semiconductor parameter analyzer. The mobility and threshold voltage were then extracted from the saturation regime using the equation

$$\mu_{sat}=\left(\frac{\partial(I_{ds})^{\frac{1}{2}}}{\partial V_g}\right)^2\frac{2L}{WC_i}$$

where I_{ds} is the drain current, V_g is the gate voltage, L=40µm is the channel length, W = 800 µm is the channel width and C_i = 11pF is the capacitance of the dielectric. A V_{ds} of 60V was used for all cases. In situ measurements were performed with this same setup, using a custom 100W resistive heater from Rama Corp to stabilize the higher temperatures. A glass slide was placed on the heater to isolate the metal heating plate from the devices which caused significant gate current. Thermal paste was used between each layer to ensure good thermal conductivity as well as to hold the setup in place during measurement. A thermal couple was attached to the glass slide using thermal paste. The temperature was incremented every 5 °C and allowed to stabilize for 5 minutes before measurements. At each temperature, the same 6 devices were measured. Devices were analyzed using python programming to extract mobility and threshold voltage from more than 100 devices.

Differential scanning calorimetry. Differential scanning calorimetry (DSC) measurements were performed using a Discovery 2500 DSC. 3-5 mg of powdered sample was loaded into a T0 aluminum pan. Heating rates varied between 5 and 10 °C min^{-1}. Enthalpies were extracted for each transition via peak integration.

CHAPTER 3: A TALE OF TWO TRANSITITIONS

3.1 CHAPTER OVERVIEW

Cooperativity is used by living systems to circumvent energetic and entropic barriers to yield highly efficient molecular processes. Cooperative structural transitions involve the simultaneous, concerted displacement of molecules in a crystalline material, in stark contrast to the more typical molecule-by-molecule nucleation and growth mechanism often breaking the single crystallinity. Cooperative transitions have acquired much attention in the research community for their low transition barriers, ultrafast kinetics, and structural reversibility. On the other hand, cooperative transitions are rarely observed in molecular crystals and the molecular origin is not well understood. Single crystals of 2-dimensional quinoidal terthiophene (2DQTT-o-B), a high-performance n-type organic semiconductor, demonstrate two thermally-activated, reversible phase transitions with one exhibiting a cooperative mechanism and the second exhibiting a nucleation and growth mechanism. In situ microscopy, single crystal and grazing incidence X-ray diffraction (GIXD), along with Raman spectroscopy suggest a reorientation of the alkyl side chains results in a cooperative transition behavior. On the other hand, the nucleation and growth transition is coincident with both side chain melting and the emergence of new spin-spin interactions between conjugated cores, confirmed through in situ electron paramagnetic resonance spectroscopy (EPR). This is the first observation of biradical interactions directly initiating a structural transition. Through studying these fundamental mechanisms, we establish alkyl chain conformation and disorder as integral to rationally controlling these polymorphic behaviors for novel electronic applications.

3.2 INTRODUCTION

A class of emergent phenomenon[91], known as cooperativity, grants the bypassing of large energy barriers in a wide variety of systems, ranging from spin flipping in magnetic materials to protein folding[92–95]. In solid state phase transitions, cooperative mechanisms occur by a concerted displacement of molecules with each molecule retaining its nearest neighbors. This results in ultrafast kinetics and lower energy barriers, relative to typical nucleation and growth type mechanisms, which occur molecule by molecule. The displacive nature of cooperativity, well documented in inorganic martensitic transitions, results in unique behaviors, such as reversible shape changes in the crystal leading to thermosalient motion[41,44,45,96] and shape memory[48,96]. A key distinction from nucleation and growth rises from interactions with defects within the crystal, which results in avalanche behavior due to pinning of the phase boundary[40,94,97–99]. While cooperative behavior has been well documented in metal alloy based martensitic transitions, it has rarely been reported in molecular crystals. As such, the fundamental origin of cooperativity in organic crystals is not well understood and the molecular design inducing this behavior is still unknown.

Recently, cooperative transitions have been observed in key organic semiconductor molecules such as 6,13-bis(triisopropylsilylethnyl) pentacene (TIPS-P), among other p-type semiconductors[44,100,101]. Cooperativity in TIPS-P led to fast switching of the electronics[102] coupled with large recoverable crystal shape change[100], resulting in super- and ferro-elastic mechanical effects[5]. In the case of TIPS-P, the rotation of the TIPS groups played a key role in the observed cooperative phenomena[101,103]. Besides dynamic rotation, other systems have shown the importance of molecular tilting and order-disorder mechanisms to resolve cooperative behaviors[104–106]. The switching of electronic properties coupled with the rapid mechanical effects of cooperative phase transitions presents a wide design space for novel organic electronics such as thermally activated actuators and highly flexible devices[44,107].

However, studies involving structural transitions in n-type counterparts (necessary for full logic design) have severely lagged behind. N-type semiconductors require relatively low lying LUMO levels for efficient electron transport, which are difficult to stabilize under ambient conditions[108–111]. One route to design stable n-type molecules involves forming a quinoidal structure using strong electron withdrawing groups such as cyano groups and attaching long alkyl chains to the core. The cyano groups break the aromaticity of the conjugated core and planarize the molecule by stabilizing the quinoidal resonance structure that exhibits double bonds between the rings. On the other hand, alkyl chains are widely used to impart solution processability and helps prevent reactions with water and oxygen in the solid state[108,112]. At the same time, these quinoidal cores stabilize an exotic biradical ground state that exists in equilibrium with the quinoidal form[17,108,112,113]. The presence of biradicals results in interesting spin-spin interactions[114,115] between the conjugated cores and, in extreme cases, results in formation of "pancake" bonding[18]. These unique interactions are also tunable through slight changes in environment (concentration, temperature etc.). Along with intermolecular interactions, biradical formation appears to have self-doping effects capable of tuning the charge carrier densities and the resulting electronic properties[98,112,116]. While both the quinoidal core and alkyl chains are key to engineering n-type semiconductor molecules, the effect on structural transitions is still unexplored.

In this work, we report an intriguing coexistence of both cooperative and nucleation and growth type mechanisms during polymorphic transitions in single crystals of 2DQTT-o-B, one of the highest performing n-type organic semiconductors to date[108,117]. The I-II phase transition, which exhibits cooperativity, is accompanied by a significant conformational change of the alkyl side chains, showing the importance of side chain flexibility in accessing cooperative phenomena. In stark contrast, the II-III transition shows a nucleation and growth mechanism driven by an increase in core interactions based on biradical formation in combination with melting of the alkyl side chains. This is the first time that both cooperative and non-cooperative transitions are reported in a single system. Further, the phenomenon of biradical interactions directly inducing a polymorphic phase transition has not been reported before. Finally, we demonstrate the use of cooperative behavior through a thermally actuated switching device, a functionality unavailable to a nucleation and growth type mechanisms.

3.3 RESULTS AND DISCUSSION

Polymorph Transition Behaviors. Crystals of 2DQTT-o-B (**Figure 3.1a**) were either grown via drop casting from a 1:1 para-dichlorobenzene and decane mixture or slow evaporation from a 1:1 dichloromethane and ethyl acetate mixture to form both small (50-300µm) and large (1-3mm) crystals, respectively (**Methods Section**). Single crystal X-ray diffraction showed crystals of 2DQTT-o-B packed in a $C_{2/c}$ unit cell with 1-D π-stacks which was designated polymorph I[117]. Based on the BFDH morphology (**Figure B1**), we observe the π-π stacking occurs along the long axis of the crystal (**Figure 3.1b**). These π-stacks then pack into layers separated by the alkyl side chains (**Figure 3.1c**), which results in the thin needle like crystals observed in polarized optical microscopy (POM). We set to investigate two thermally induced structural transitions in single crystals of 2DQTT-o-B using polarized optical microscopy, where we heated and cooled crystals at a constant 5 °C min^{-1}. We observed two reversible phase transitions designated the I-II transition at 164 °C and II-III at 223 °C. The phase transitions were accompanied by modulation of the brightness and color, reflecting changes in the refractive index of the material (**Figure 3.1d,e**, **Movies B1-2,3-4**). We observed distinct transition behavior suggesting a cooperative transition mechanism for the I-II transition as opposed to a nucleation and growth mechanism during the II-III transition. Below we discuss evidence from in situ POM in detail and this inference is further supported by in situ GIXD, Raman spectroscopy and EPR spectroscopy discussed later.

Using python-based image analysis, we were able to select individual crystals and track the progression of the phase transition by calculating an average intensity for each frame. The I-II transition proceeded remarkably fast upon heating (**Figure 3.1d, Movie B1,2**). Across many crystals, the heating transition typically occurred within one frame, less than 0.1 second, providing a lower bound for the propagation speed of at least 2000 µm s^{-1}, implying a cooperative-type mechanism. While difficult to capture under normal circumstances due to the speed, this rapid transition is accompanied by a well-defined phase front propagating through the crystal, distinct from typical diffuse phase boundaries under nucleation and growth mechanisms. Initiation of such phase front typically occurred at the crystal tips, or at cracks within the crystal. Even when the transition initiated at both tips simultaneously, the resulting crystal was a single domain after transition, suggesting a close orientational relationship between the two phases. This is consistent with our earlier work by Chung and Diao et. al.[118] which showed defects facilitated phase boundary initiation in similar cooperative transitions of ditBu-BTBT followed by cooperative propagation.

During cooling the sharp phase boundary becomes much more evident due to avalanche behavior, where the phase boundary became pinned during transition (**Figure 3.1d, Movie B2**). These avalanches follow behavior seen in inorganic martensitic transitions, where defects in the lattice, such as dislocations, create a local free energy minimum and corresponding energy barrier[40,97,119]. The resulting rough free energy landscape causes the boundary to move in a series of jerks and requires thermal fluctuations to jump over the defect barriers. As mentioned, the avalanches were found during cooling, which is clearly observed as plateaus in the crystal intensity during the temperature changes (**Figure 3.1f,g**). This suggests the initial heating transition may be resulting in an increasing number of defect sites within the crystal that cause avalanches in subsequent cycles. However, despite taking several seconds, up to minutes, to become unpinned, this typically does not change the speed of the transition as each avalanche still occurs within less than one frame of the video (**Figure 3.1g)**.

Moreover, the direction of the phase boundary is only observable during these pinning events. In these cases, we observe two main crystallographic directions along which the boundary forms: the (010) and (025) planes both of which are connected to the π-stacking direction. The (010) direction lies perpendicular to the 1-D π-stacks, suggesting the cooperative behavior is transmitted down the π-stacks, similar to a domino effect (**Figure 3.1i**). On the other hand, the (025) plane parallels the conjugated core of the molecule and was indexed to the π-π stacking peak in grazing incidence X-ray diffraction[117]. The crosshatch structure of the π-stacking results in two mirrored directions within the crystal, following the two-phase boundary directions (**Figure B3a-c**). This would suggest a cooperative behavior is transmitted along the 1-D π-stack and is inhibited by dislocations present in those stacks.

In contrast, the II-III phase transition (**Figure 3.1e**, **Movies B3,4**) showed nucleation at several points within the crystal and transformed over several minutes, with polymorph III increasing in brightness under polarized microscopy. The II-III transition exhibited no clear phase boundary, instead we observed a diffuse spreading of the intensely bright polymorph III. The most common nucleation points are near the edges of the crystal, though cracks and other defects will act as nucleation spots (**Figure 3.1e**) as well. By tracking the intensity change over temperature, we observe a quite smooth change, with no avalanche like behavior **(Figure 3.1f,h)**. Upon cooling, the reverse transition began at a temperature below that of the I-II transition, exhibiting a hysteresis of 100 °C, an order of magnitude greater than the I-II transition which showed a hysteresis of only 17 ± 5 °C, confirming a much larger energy barrier for nucleation and growth mechanism. This matches with observations from DSC using powder samples, showing a hysteresis for the I-II and II-III transitions of 6°C and 75 °C, respectively[117]. In single crystals, the hysteresis for the II-III transition varied substantially and, in some cases, the III-I transition did not occur during constant cooling, resulting in the kinetic trapping of polymorph III at room temperature. This suggested a nucleation and growth behavior, shown in **Figure 3.1j**, where nucleation occurred at edges or defects and diffusively spread through the crystal.

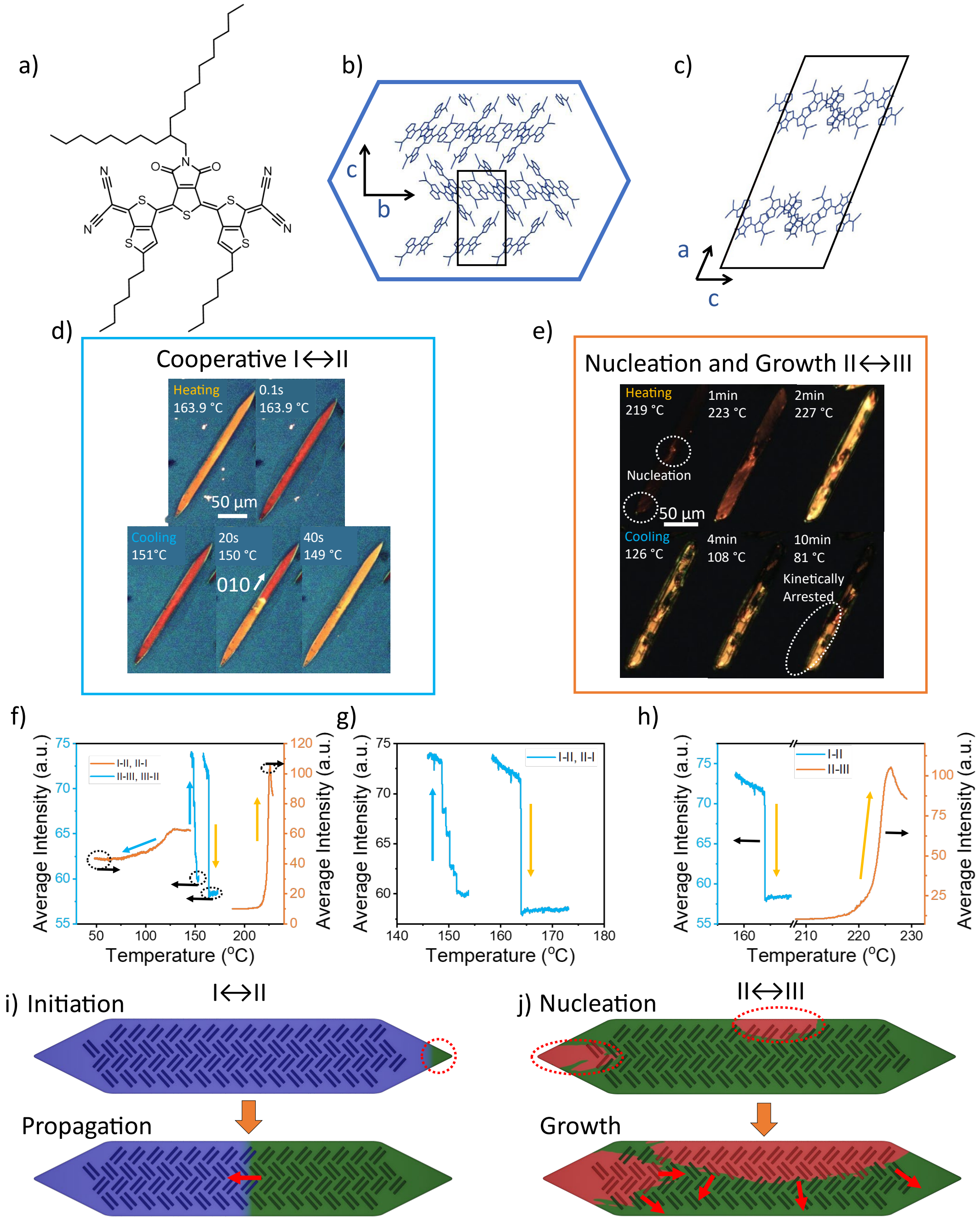

Figure 3.1. Comparison of single crystal transition kinetics. (a) 2DQTT-o-B molecular structure. Crystal packing of polymorph I in the crystal viewed from (b) the top of the crystal (down a*) and (c) along the b-direction. The crystal shape is outlined in blue and the unit cell is outlined in black. In situ POM showing the I-II (d) and II-III (e). (f) By tracking the transition progress via intensity changes of the crystals, we observe the avalanche behavior of the I-II transition (g) and see the stark difference in kinetics (h) between the I-II and II-III heating transitions. The dark blue and red lines indicate the I-II and II-III transitions respectively and the yellow and blue arrows indicate the heating and cooling transitions respectively. Black arrows indicate the axis for each line. Schematic showing the typical modes for initiation and propagation of the (i) I-II and (j) II-III transition.

Thermosalient behavior. Upon undergoing the I-II transition, we found the crystal decreased in length by 3.6 ± 1.3% on average (**Figure 3.2a**, **Table S1**). This change in length was matched quite closely with the 2.9% decrease in the b-direction of the unit cells obtained through fitting the thin film GIXD diffraction patterns (**Figure 3.2b**), as we previously reported[117]. This shape change led to cracking of pinned small crystals of ~100 µm in size (**Figure B2, Movie B5**), which occurs due to the buildup of strain at the phase front caused by the change in shape coupled with crystal-substrate interactions that act to prevent the shape change. In an extreme case, we observed a crystal embedded in a surrounding film that formed during the drying process, which cracked upon transition. This case also resulted in the formation of "bright bands" along the phase boundary, visible in **Figure B4**, which would be consistent with strain induced birefringence we expect from a crystal attempting the I-II transition while trapped in a solid film. On the other hand, for unpinned large crystals (1-3mm), we observed a pronounced thermosalient behavior during the I-II transition (**Figure 3.2c, Movie B6**). While the crystal will bend during the I-II transition, reversing the transition will not recover original shape, implying a plastic deformation. This may be a result of strain buildup at the phase boundary causing the π-stacks within the crystal to irreversibly slip along the greasy alkyl chain layers.

In the II-III transition, however, we observed a slight expansion to the crystal without thermosalient behavior (**Figure 3.2d**). The change did not conform to the unit cell changes, as polymorph III exhibits a vastly different symmetry and unit cell relative to polymorph II (**Figure 3.2e**) and results from thermal expansion during heating. This reconstructive transition also leads to the formation of multiple grain boundaries within the crystal, breaking single crystallinity (**Figure 3.2f**). Formation of these domains mitigate strain build up preventing any thermosalient motion from occurring due to the crystal expansion. These observations are consistent with the understanding that the nucleation and growth mechanism does not incur shape change owing to a single-to-polycrystalline transition[120]. This stands in contrast to the cooperative martensitic transition that preserves single crystallinity and thus exhibits shape reversibility corresponding to the unit cell change.

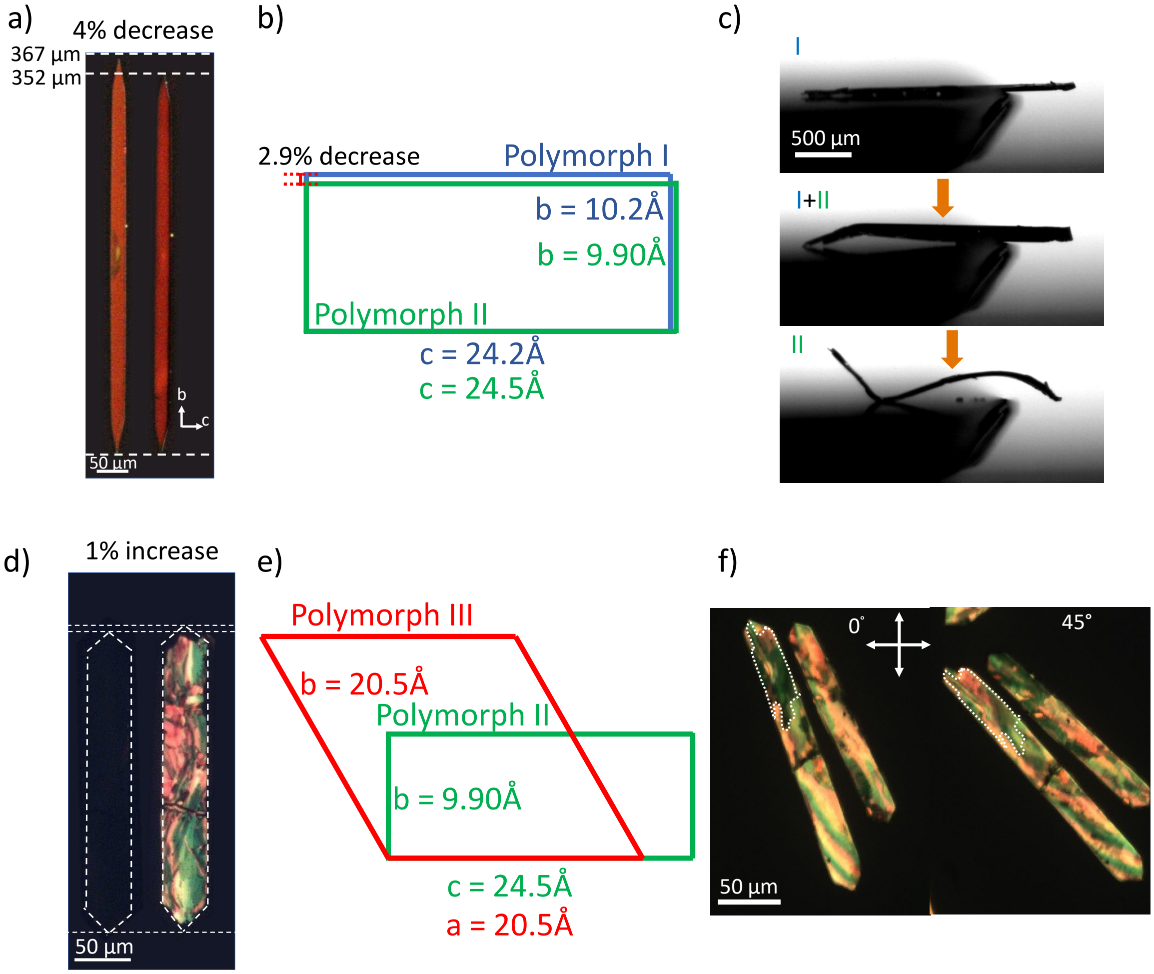

Figure 3.2. Shape change and thermosalient behavior. (a) Crystal shape change associated with the I-II transition and (b) associated in plane unit cell change accounting for the change in crystal length along the b axis of the unit cell (unit cell drew in the same orientation as the crystal in (a)). (c) The resulting thermosalient effect in larger crystals caused by the shape change. (d) Crystal expansion observed in the II-III transition, compared to (e) the unit cell changes, where the unit cell is shown in the same orientation as the crystal in (d)), and observation of (f) birefringence showing multiple domain formation under polarized optical microscopy.

Molecular Origin of Transition Mechanisms. Uncovering the origins of the transition behaviors requires understanding the molecular and structural modifications during the phase transitions. To that end, we performed in situ grazing incidence X-ray diffraction (GIXD) during thermally triggered polymorph transitions. A GIXD video of the I-II transition was obtained by continuous heating at 5 °C min^{-1} and capturing the diffraction pattern every 5 seconds (**Movie B7**). The unit cells for polymorphs I and II were extracted from the GIXD patterns via a regression fitting the diffraction pattern as discussed in previous work[117]. This fitting for polymorph I also matched the single crystal unit cell obtained at room temperature[117]. During the I-II transition, we observed minor changes to the unit cell, showing peak movements in the q_z direction while keeping the Bragg rods in place and maintaining the monoclinic symmetry (**Figure 3.3a,b**). The largest extent of peak shift in the q_z position occurred right before the I-II polymorph transition, similar to pretransition behavior observed by Panda and Naumov et. al.[42,45] (**Figure 3.3c,d**). This pretransition behavior is typical of pretransition regions of critical phenomena[121], such as in the lattice fluctuations necessary to drive the avalanche behavior[122]. Comparing the fitted unit cells for polymorphs I and II (**Figure 3.3a**), there is a significant increase in the β-angle during the I-II transition, consistent with the observed out of plane shift. By comparing single crystal X-ray diffraction with GIXD for polymorph I, we showed this angle reflects the molecular tilt with respect to the substrate, measured to be 66° (**Figure B5**), commensurate with the complement of the β-angle, measured to be 67°[117]. During the I-II transition, the β-angle changed from 113° to nearly 90°, suggesting the molecules standing straight up from a more tilted position, like reverse dominos.

To elucidate the driving force behind this change in tilt, we turned to in situ Raman spectroscopy to provide insight into the molecular changes occurring in the I-II transition (**Figure 3.3d,e**). Raman has shown to be a powerful tool for tracking polymorphic transitions and understanding the molecular changes that occur as a result of these transitions[100,123,124]. Under Raman spectroscopy crystals exhibit both low frequency peaks related to the intermolecular phonon vibrations, sensitive to the crystal structure (< 500 cm^{-1}), as well as intramolecular vibrations related to the conformation and chemical environment of the molecule (900-1800 cm^{-1}). In the phonon region, we observe two key peaks which are associated with lattice vibrational modes, indicated with black arrows in **Figure 3.3f**. We observe a ratio change between these two peaks, as the lowest peak increases in intensity during the I-II transition (**Figure 3.3f**). This is a small effect, indicating modest changes to the lattice packing consistent with our observation of changing molecular tilt from GIXD. Phonon intensity modulation, as opposed to peak shifts or splitting has been shown to be typical in well studied martensitic type cooperative transitions[125,126]. On the other hand, in the intramolecular vibration region (900-1800 cm^{-1}), we observed significant changes to the intensity of the peak at 1409 cm^{-1} relative to the most intense peak at 1387 cm^{-1} indicated by the red and blue arrows in **Figure 3.3g,** respectively and illustrated in **Figure 3.3e**. Based on a combination of DFT calculations (**Figure B6b**) and literature, we assigned the peak at 1387 cm^{-1} to C=C stretching along the backbone, corresponding to the effective conjugation coordinate (ECC) mode for the quinoidal form[127–129] which we denote as $\nu(C=C)_{ECC,Q}$ (**Figure B6c, Movie B8,9**); the peak at 1522 cm^{-1} was assigned to other C=C stretching modes in the backbone (**Figure B6e, Movie B10**); the peak at 1772 cm^{-1} was assigned to C=O stretching **(Figure B6e, Movie B11**). While the peak at 1409 cm^{-1} may correspond to core stretching (**Figure B6d, Movie B12**), this was assigned to CH_2 deformation in the alkyl chains denoted as $\delta(CH_2)$ based on well-established literature[130–133] on alkyl chain vibrations. Along with these peaks, we also tracked the peaks at 1025 and 1063 cm^{-1} which were assigned to C-C stretching of the trans $\nu(C\text{-}C)_T$ and gauche $\nu(C\text{-}C)_G$ isomers in the alkyl chains. The alkyl chain peak assignments ($\delta(CH_2)$, $\nu(C\text{-}C)_T$, $\nu(C\text{-}C)_G$) were confirmed based on Raman spectroscopy measured on a similar molecule with shorter side chains (**Figure B7**). A complete explanation for these assignments can be found in the supplementary information.

To investigate the changes in these vibrational modes during the phase transitions, peaks were fit using OriginPro in both the 1000-1100 cm^{-1} region and 1350-1600 cm^{-1} region (**Figure 3.3g**). Peak line shape was selected as either Gaussian or Lorentzian based on whether the vibrational mode was associated with the quinoidal core or alkyl chains, respectively. Normally, the line shape in solid crystals is expected to follow a Gaussian curve; however peaks associated with the alkyl chains were fit as Lorentzian due to the disorder, causing more liquid like behavior[134–136]. In the 1000-1600 cm^{-1} range, which captures the core and alkyl chain vibrations, we note a significant intensity reduction and redshift of the $\delta(CH_2)$ peak at 1409 cm^{-1} during the I-II transition. We plotted the intensity ratio with respect to $\nu(C=C)_{ECC,Q}$ and the peak position to show this sudden drop in intensity and redshift of 7 cm^{-1} in the $\delta(CH_2)$ at the I-II transition temperature (**Figure 3.3h-i**). This trend was repeated across 3 crystals to ensure this change is representative of the I-II transition (**Figure B8a,b**), though the exact transition temperature varied by 5 °C for each crystal due to avalanche behavior. The redshift is indicative of reduced steric hinderance or an increase in the attractive forces between alkyl chains. The intensity decrease, on the other hand, implies alterations to either the orientation or distribution of vibrational states in the alkyl chains. Taken together, these changes show a substantial reorientation of the alkyl chains occurs during the I-II transition.

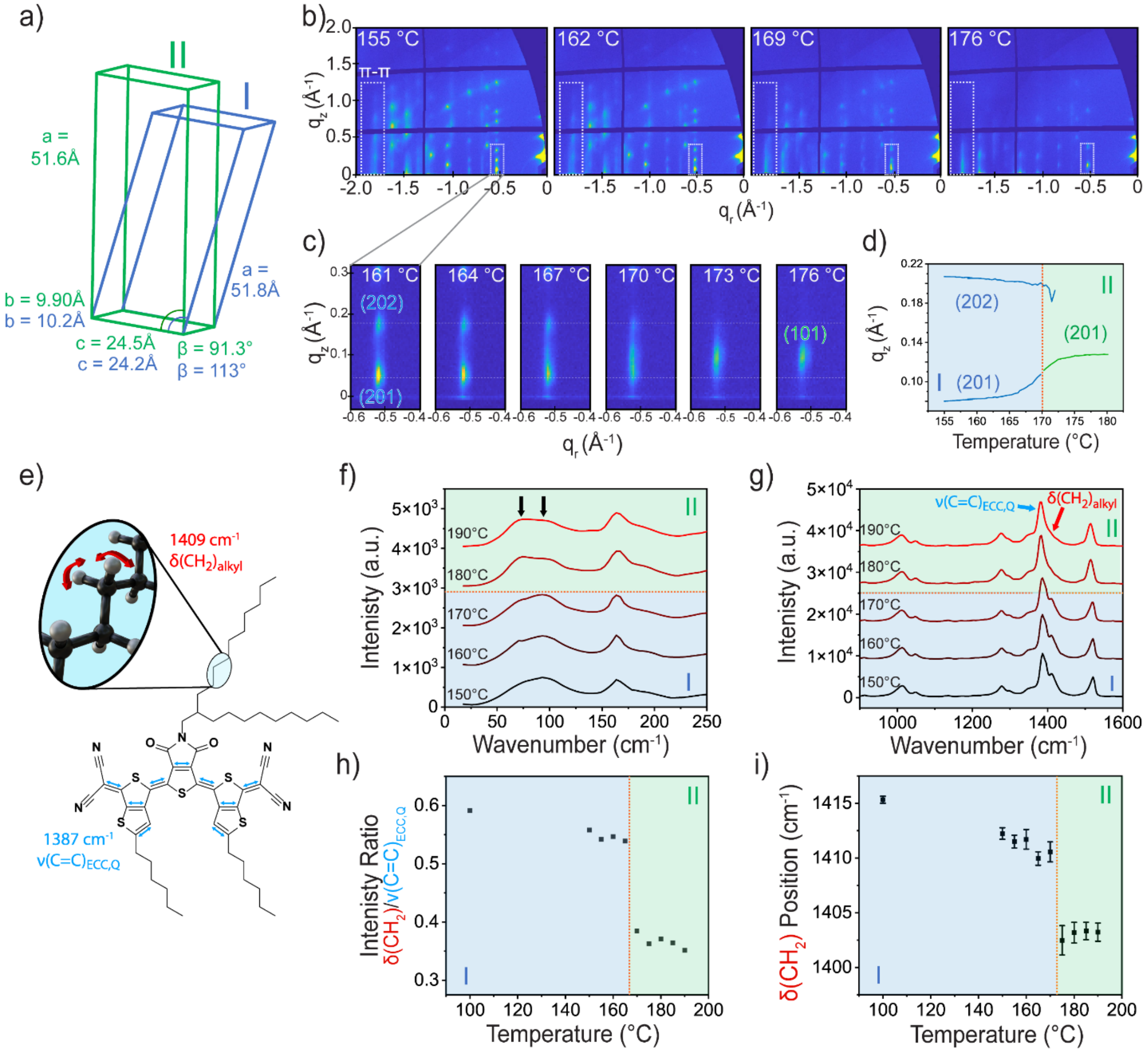

Figure 3.3. Molecular origins of I-II transition. (a) Unit cell changes from polymorph I (blue) to polymorph II (green). (b) Frames from **Movie B7**, showing the out of plane peak motion under grazing incidence X-ray diffraction. (c) Changes to the (10) Bragg rod reflecting the change in the β-angle and (d) associated plot of q_z peak position during the I-II transition. (e) schematic showing the major vibrational modes associated with the CH_2 deformation mode ($\delta(CH_2)$, red) and the ECC mode for the quinoidal core ($\nu(C=C)_{ECC,Q}$, light blue). Evolution of in situ Raman spectra with increasing temperature for the (f) phonon region and the (g) core C=C stretching region. (h) Decrease in the intensity ratio of $\delta(CH_2)$ to $\nu(C=C)_{ECC,Q}$ tracking the change in alkyl chain conformation during the I-II phase transition. (g) $\delta(CH_2)$ peak position change during the I-II phase transition, which redshifts along with the decrease in intensity. Error bars reflect error in the peak fitting and orange dashed lines indicate transition temperatures.

For the II-III polymorph transition, we see large changes in the unit cell, as polymorph III appears to form a likely hexagonal crystal system (**Figure 3.4a**), obtained from the GIXD pattern as discussed in previous work[117]. This is consistent with other previous observations which have shown crystals have a propensity to increase in symmetry at higher temperatures[137]. GIXD video of the II-III transition (**Figure 3.4b**, **Movie B13**) showed the significant reduction in observable peaks, as a result of increased symmetry of the hexagonal lattice as well as reduced long-range order as higher q peaks are no longer measurable (to be discussed later). Despite the reduced diffraction of other Bragg rods at higher q values, the π-stacking peak remains intense and well defined in polymorph III, in line with a continued dominant π-stacking motif. The reconstructive transition is further highlighted by observing the complete disappearance of the polymorph II diffraction peaks at the expense of polymorph III peaks (**Figure 3.4c,d**), with no shift in position prior to transition, which is consistent with a nucleation and growth type mechanism.

Upon investigation of the II-III transition mechanism via Raman spectroscopy, we observed something quite unexpected: we see the marked weakening of the core stretching peak $\nu(C{=}C)_{ECC,Q}$ at 1387 cm^{-1}, while 2 new peaks appear at higher wavenumbers, 1442 and 1497 cm^{-1} (**Figure 3.4e,f**). This indicated a modification to the conjugated core itself. We initially suspected this may be a degradation of the molecule at such high temperatures. However, the temperature at which the peaks appeared were highly correlated with the II-III transition and, moreover, this peak formation was found to be reversible (**Figure B9**). Along with this, we also observed a change in the intensity ratio between the peaks located at 1025 and 1063 cm^{-1}, previously assigned to the trans ($\nu(C\text{-}C)_T$) and gauche ($\nu(C\text{-}C)_G$) isomers, respectively. Based on these observations, we hypothesize a transformation from a quinoidal structure to aromatic structure accompanied by decreased order of the alkyl side chains; such quinoidal to aromatic transitions have been observed in similar systems[98,111,113,138].

Previous work on similar quinoidal systems has revealed the presence of a singlet biradical ground state which affects the molecular structure and, by extension, the intermolecular interactions. Moreover, previous work on these biradical forms showed a sensitivity to temperature offering the intriguing possibility that the II-III transition occurred alongside a quinoidal to aromatic transition[18,98]. The key change in molecular structure between a quinoidal and aromatic form is the alternation between the single and double bonds along the conjugated backbone, which is described by the bond length alternation (BLA) parameter, the average difference between consecutive single and double C-C bonds. A BLA < 0 defines the quinoidal structure whereas a BLA > 0 defines the aromatic form. Because of this change in bond length, Raman spectroscopy is quite sensitive to these biradical forms, due to the difference in vibrational frequency of the ECC mode in the quinoidal and aromatic systems[98,111,113,138]. We simulated the Raman spectrum for this scenario by forcing the BLA into the aromatic form via substituting the cyano groups for methyl groups on the ends of the molecules and compared this to the spectra obtained from polymorph III (**Figure B10**). This allowed us to assign the two new peaks at 1442 and 1497 cm^{-1} to the ECC of the aromatic form $\nu(C=C)_{ECC,A}$ (**Figure B10b, Movie B14**) and asymmetric stretching modes along the conjugated backbone ($\nu(C=C)_{asym}$) (**Figure B10c, Movie B15**) respectively. The complete explanation for these assignments is found in the supplementary information.

Based on this assignment, we plotted the intensity ratio of the 1442 cm^{-1} to the 1387 cm^{-1} peaks, representing the ratio of aromatic to quinoidal forms, as we increased temperature (**Figure 3.4g, top**). We observe a significant increase in the biradical form starting at the II-III transition. Moreover, the intensity ratio of trans to gauche C-C stretching also changed during the transition (**Figure 3.4g, bottom**). As polymorph III formed, this ratio decreases drastically, suggesting significant changes in the alkyl chain dynamics. In previous works, the intensity ratio of these two conformers provide an indication of disorder in the alkyl side chains[130,132,139,140]. As more gauche isomers form in the system, the alkyl chains become bent and twisted within the occupied volume. A complete melting of the alkyl side chains is represented by a ratio of 1, as the chains become free to bend in any direction. In the 2DQTT-o-B system, the intensity ratio of trans to gauche decreases from 8 to 1 across the II-to-III transition. These results strongly suggest that the formation of biradical species and alkyl chain melting are the molecular origins of the II-III phase transition.

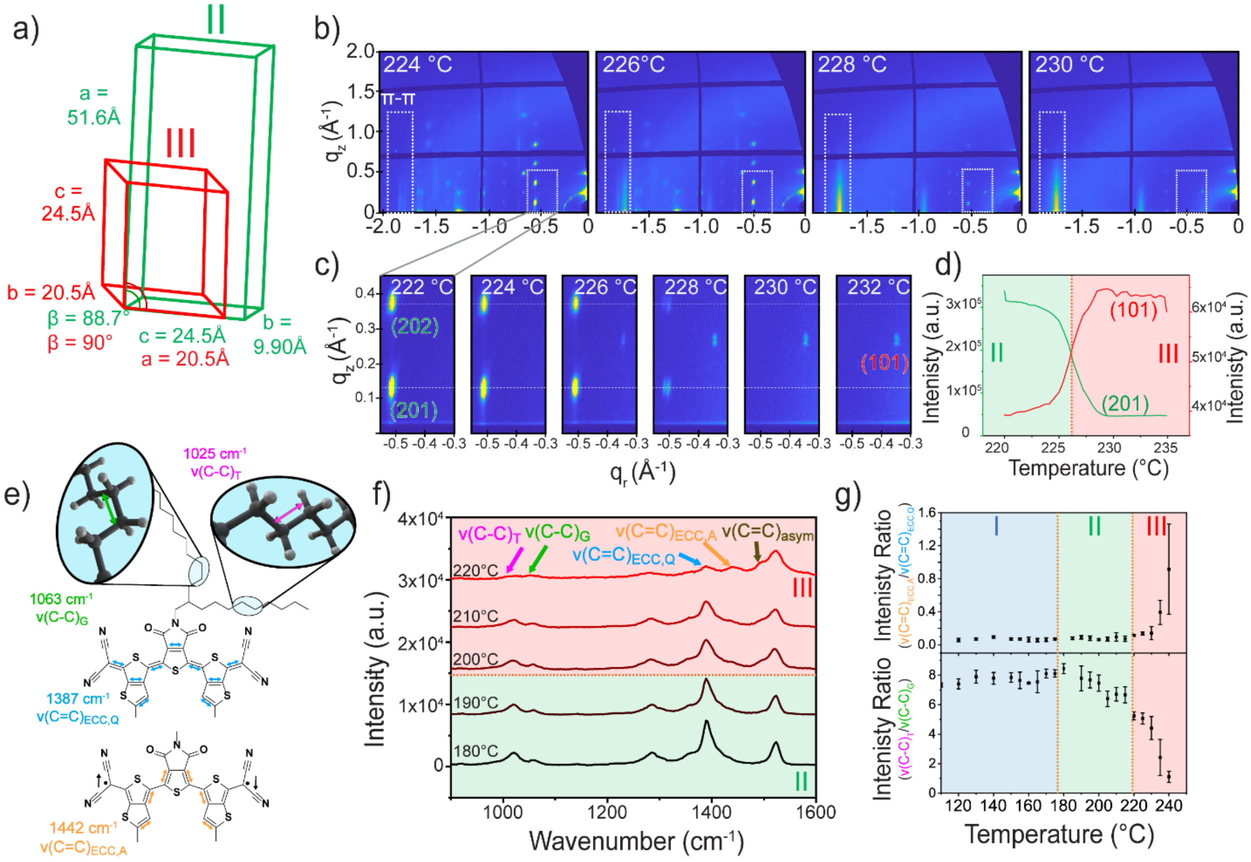

Figure 3.4. Molecular origins of II-III transition. (a) Unit cell changes from polymorph II (green) to polymorph III (red). (b) Frames from (**Movie B13**), showing the diffraction peak evolutions during in situ GIXD. (c) Enlarged view of the (20) (polymorph II) and (10) (polymorph III) Bragg rods and (d) associated plot of q_z peak position during the I-II transition. (e) Main vibrational modes for the peaks assigned to the $v(C=C)_{ECC,Q}$ $v(C=C)_{ECC,A}$. (f) Evolution of in situ Raman spectra with increasing temperature for the core C-C stretching region. (g) Intensity ratio of aromatic conjugated core to quinoidal core increase during II-III phase transition (Top), and corresponding decrease in the trans to gauche intensity ratio (Bottom).

To confirm the formation of biradicals, we also simulated and compared the absorption spectroscopy as well as measured the spin states in the crystals through in situ EPR spectroscopy to directly observe the formation of these biradical states. UV-Vis was simulated for both the quinoidal and aromatic forms via setting the BLA value for each of the systems (see methods). The simulated UV-Vis spectra for the quinoidal molecule showed good agreement with the experimental spectra (**Figure B11a**) though we expect the redshift and vibronic fine features resulting from crystalline packing not to be captured in the simulation. For the aromatic molecule, the simulation showed a significantly red shifted and broadened peak compared to the quinoidal form, similar to the redshift observed in the experimental spectra (**Figure B11b**). Based on Raman, we expect a mixture of quinoidal and aromatic forms, which may account for a smaller extent of red shift observed than predicted by simulation (**Figure B11c,d)**. Nonetheless, the good qualitative match between simulated and experimental spectra suggests that the biradical aromatic form provides a good model for describing the molecular system in polymorph III. Finally, as expected from our hypothesis, in situ EPR showed an increasing presence of spins in our system as we increased temperature (**Figure 3.5a**). EPR directly measures the increasing unpaired spins associated with the biradical state (**Figure 3.5a**) and indeed, we see a dramatic increase in the concentration of spins within the material (40x increase) upon reaching the II-III transition (**Figure 3.5b**). This confirms that the II-III transition not only exhibits a large structural change, but also that a key part of this transition involves accommodating the abruptly increased concentration of biradical species through a reconstructive structural transition (**Figure 3.5c**).

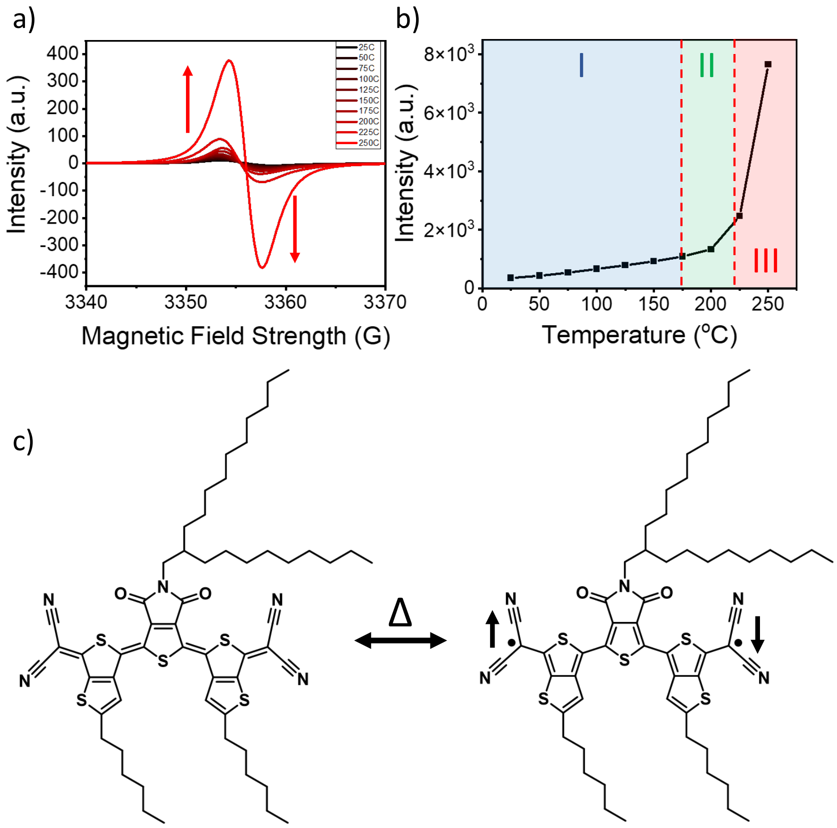

Figure 3.5. (a) In situ EPR spectra (b) doubly integrated intensity across varying temperature showing a substantial increase in number of spins with heating. (c) Proposed schematic for biradical formation associated with the EPR signal.

Proposed Structural Transition Mechanisms. Based on the molecular changes described previously, we suggest the I-II cooperative transition occurs via a change in the tilt in the molecule driven by alkyl side chain conformation change (**Figure 3.6a**). Much like stacks of dominos tilting all at once, molecules along the b-axis of the crystal constituting the 1-D π stacks stand up during the I-II transition. In this case, the tipping of the molecule is caused by a conformation change in the alkyl side chains, which results in the molecule standing upright during heating and allowing the molecule to slip back into a tilted position during cooling. We suggest engineering of these alkyl side chains may be crucial in facilitating the I-II cooperative behavior. While recently rotation of bulky side chains have been shown to be critical for expressing cooperative behavior in molecular crystals[5,100,101], cooperative polymorph transition has rarely been studied in molecules with alkyl side chain motifs – a dominant side chain design in organic crystals[107,141,142]. Until now, their role in facilitating cooperative transitions has not been well understood.

The II-III phase transition, however, was shown to be driven by the formation of biradical species and is facilitated by increased mobility of the alkyl side chains during a melting process. At room temperature, the concentration of biradical cores is quite low, meaning the potential for spin-spin interaction is quite low. However, as the temperature increases through the II-III transition, the biradical concentration abruptly increases conducive to forming new spin-spin interactions[18,111]. Typically, in molecules where the biradical ground state is dominant, the major packing motifs are either face-on dimer pairs when unhindered[17,143] or ladder-like stacking[114,144] when steric hinderance prevents the former. In both cases, the high spin centers (where the radical is most localized) will line up and, in some circumstances, form a pseudo σ-bond[17,18,98,143].

One possibility of molecular packing change during II-III transition is shown in **Figure 3.6b**, where molecules form dimers with the nearest neighbor in the original polymorph II structure. Since the crystal packs in these 1-D π-stacks with dimer-like pairs already, this would be a natural progression. While the dimer formation may be plausible, we cannot say with certainty how those dimers then pack to form polymorph III. Regardless of the new core packing motif, to facilitate the II-III also necessitates alkyl chain melting, indicated by increased gauche conformers. Moreover, this side chain melting is consistent with the kinetic trapping observed (**Figure 3.1e** and **Movie B4).** As we observe upon cooling to 37 °C, the alkyl chains return to a frozen state however there appears to be residual biradicals not yet quenched by cooling, owing to a residual lifetime of the biradical state (**Figure B6**). As a result, polymorph III is trapped and would not return to polymorph I due to freezing the alkyl chains before the conjugated cores rearrange back into polymorph I that may require quenching of biradical species. However, without the full structure of polymorph III, we are left only to postulate possible molecular packings. Nevertheless, we can suggest the nucleation and growth polymorph transition is the result of increased core-core interactions triggered by the biradical formation, and the large packing changes are necessarily facilitated by increased molecular mobility from the melted alkyl side chains.

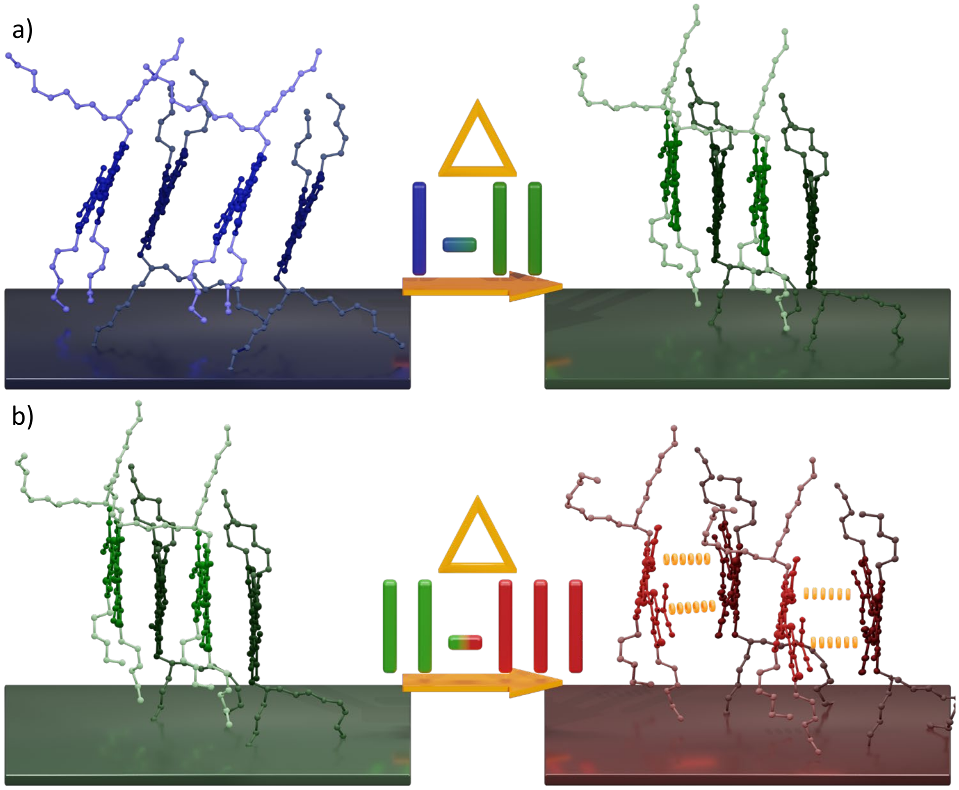

Figure 3.6. Proposed transition mechanisms. for the (a) I-II and (b) II-III transitions.

Electronic and device properties. We worked to demonstrate the control and design of organic electronics utilizing these transition mechanisms. We fabricated single crystal devices to measure the two-point-probe conductivity of each polymorph (**Figure 3.7a,b**). The crystals were pre-bent fixed at two ends by PEDOT:PSS electrodes. When heated to trigger I-II transition, the crystal would straighten from the pre-bent state due to shape change shown in **Figure 3.2a**. We observed a 6-fold decrease in conductivity at the I-II transition, with good recoverability during cooling albeit with a hysteresis. Moreover, we see a moderate increase in conductivity upon polymorph II-III transition. We suspect this recovery of conductivity may be a result of charge carrier doping through the presence of biradicals, similar to Wudl et. al., which showed a self-doping effect[116]. This self-doping process may compete with the reduction in charge transfer pathways due to structural transitions.

We then were able to harness the shape change discovered in the I-II transition for reliable thermal actuation (**Figure 3.7c,d**). For the device, we attached a crystal at both ends using PEDOT:PSS and upon heating, the crystal became dislodged on one side due to the cooperative shape change. This allowed for switching on and off the device by cycling between polymorphs I and II, exhibiting an on/off ratio of 500 and effectively reaching the noise floor for device measurement in the off state. Because the crystal became detached in the polymorph II state, we observed no conductivity and cooling back to polymorph I reforms the contact between the crystal and the PEDOT:PSS, turning the device back on. This provided quite reliable cycling for several cycles until out of plane bending prevented stable contact between the PEDOT:PSS contacts.

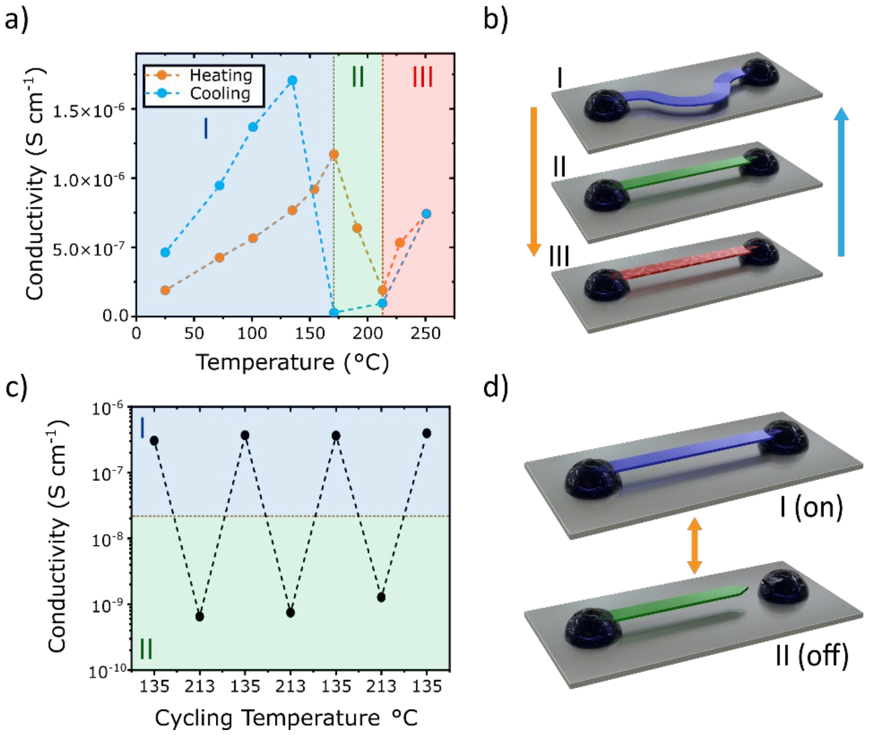

Figure 3.7. Cooperative transition driven actuator device. (a) in situ temperature variable conductivity measurements showing modulation of the conductance based on polymorph and (b) corresponding device architecture. (c) Cycling of single crystal actuator device and (d) corresponding device architecture.

3.4 CONCLUSIONS

We observed both cooperative and nucleation and growth behavior within the 2DQTT-o-B system, allowing for direct comparison of molecular origins of these transitions in a single material. We discovered the I-II transition exhibited cooperative behavior, resulting in a rapid, shape changing transition dominated by avalanches as defects were introduced. The transition was found to be driven by changes in the alkyl side chain confirmation, as revealed by Raman spectroscopy. This was in striking contrast with the slow, smooth II-III transition showing clear nucleation and growth behaviors. Unlike the I-II transition, the II-III transition was driven by changes in spin-spin interactions through biradical formation which is the observation of biradical interactions triggering a polymorphic phase transition.

We then harnessed cooperative behaviors for the design and application of novel organic electronic switching behavior. Not only were we able to tune the conductivity by orders of magnitude via the structural changes, but we could also use the mechanical effects to sever the connection with one of the PEDOT:PSS contacts. By taking advantage of the mechanical effects of the cooperative shape change, we could switch on and off a single crystal device through rapid temperature actuation. This opens the door for fusing the novel mechanical effects of cooperative transitions with device architecture for new functionality. Ultimately, understanding the origin of these transition mechanisms offers pathways to rationally designing organic semiconductors to access cooperative transitions with these exciting properties.

3.5 MATERIALS AND METHODS

Materials synthesis. Synthesis of 2DQTT-o-B has been published in Reference [108].

Single crystal fabrication. Single crystals of 2DQTT-o-B were fabricated through a dropcasting method. Solutions with concentrations between 10-15 mg mL^{-1} of 2DQTT-o-B dissolved in a 1:1 mixture of dichlorobenzene and decane were heated to 100 °C. 5-15 µL were dropped onto PTS-treated silicon wafers (SiO_2/Si) and allowed to dry overnight. For large crystals (SCXRD and Raman experiments), 2DQTT-o-B was dissolved in a 1:1 mixture of dichloromethane and ethyl acetate at 1 mg mL^{-1} in a 30 mL vial (up to about 15 mL of solution was used). The solution was then capped with parafilm and 1-5 holes were created in the film using a needle. The vial was then placed in a glove bag under nitrogen atmosphere for slow evaporation over a few weeks. The nitrogen in the glove bag was refilled every other day to prevent oxygen from reacting with the molecule and ensure saturation of solvent vapors did not occur.

Polarized optical microscope. Single crystals grown under the dropcasting procedure were placed on a Nikon H550S with a high-speed camera (Infinity 1) and heating stage (Linkam 402). The chamber was sealed with a magnetic lid and O-ring during heating. The temperature ramp was kept at a constant 5 °C min^{-1}. Videos were recorded at framerates ranging from 1 to 7.5 fps. Video analysis was performed using a python program to obtain an average intensity value of a given crystal at each frame.

Grazing incidence X-ray Diffraction. GIXD was performed at beamline 8-ID-E of the Advanced Photon Source at Argonne National Laboratory[145]. The data were collected at 10.91 keV on a 2D Pilatus 1M detector. Films of polymorph I were obtained by solution coating from a solution of 2DQTT-o-B dissolved in chloroform and chlorobenzene at 6 mg mL^{-1} onto SiO_2 treated with trichloro(phenyl)silane (PTS). Solution coating was performed at 85 °C at a blade speed of 0.3 mm s^{-1} and a blade gap of 100 µm. These films were annealed under nitrogen atmosphere for 30 minutes at 100 °C to convert the films to polymorph I. In situ thermal annealing measurements were conducted in a He environment with the sample on a commercial thermal stage (Linkam HFSX350-GI), with the temperature ramped at 10 °C min^{-1} and the exposure taken after equilibration at the target temperature for approximately 5 min. GIXD videos (**Movies B7,13**) were obtained via taking continuous exposures at a constant heating of 5 °C min^{-1}. GIXSGUI software was used to correct for detector nonuniformity, beam polarization and to reshape the 2D data into the representation q_z vs q_r[146]. The incident angle was set at 0.14° right above the critical angle for total reflectance of the organic thin film. Unit cells were extracted based on the discussion in the previous paper by Davies and Diao et. al., 2021.

Raman Spectroscopy. A Raman confocal imaging microscope with a 532 nm laser (Laser Quantum Ventus 532 with max power 50 mW) and 50× long working distance objective lens (HORIBA LabRAM HR 3D) equipped with HORIBA Synapse back-illuminated deep-depletion CCD camera was used to collect spectra. Using a 300 g mm^{-1} grating, we used a scan exposure time of between 20-60 s. An optical density filter of OD = 0.2 was used (OD = log(power transmission factor)), and no beam damage was observed only at the highest temperatures after prolonged periods of laser exposure (>5min). To eliminate this effect, each spectrum was recorded in a new position on the crystal to prevent overexposure of any particular area. For variable-temperature experiments, the samples were collected using a Linkam THMS600 heating stage with a closed chamber. The heating and cooling rate was kept at 10 °C min^{-1}. Each temperature was equilibrated until the temperature reading stabilized and the Raman laser was refocused to account for substrate thermal expansion (approximately 5 minutes).

Electron Paramagnetic Resonance Spectroscopy. Crystals of Polymorph I were grown via the slow evaporation method from DCM and EA described in the crystal fabrication above, were dried out and then placed in an EPR tube. The crystal sample was then measured on an EMXplus running the Xenon software with variable temperature (part no. E0000071) for in situ EPR measurements. The temperature was stepped by 25 °C up through the II-III phase transition. The Intensity at each temperature was then doubly integrated and plotted vs temperature.

Electronic properties. For single crystal devices, large needle like crystals were grown from a 1 mg mL^{-1} solution of 1:1 mixture of dichloromethane and ethyl acetate. These crystals were pre-bent and attached to a glass substrate, using conductive PEDOT:PSS. Pre-bending allowed for the devices to be heated through the I-II transition without cracking or breaking the device. The device was measured in air using a Keysight B1500A semiconductor parameter analyzer. The current through the crystal was measured by contacting the PEDOT:PSS with 2 probes and current was obtained as a function of source-drain voltage.

Actuator devices were fabricated by attaching the crystal with PEDOT:PSS without pre-bending the crystal. During the first cycle of the I-II transition, one end becomes detached from the PEDOT:PSS due to the crystal shape change. This device can then be cycled multiple times as once cooled down, the crystal reconnects with the PEDOT:PSS contact.

DFT calculations. Ground-state geometries of isolated molecules were optimized at the DFT level using the ωB97X-D functional and def2TZVPP basis set. IR and Raman frequencies were calculated at the same level of theory. For the quinoidal form, the original molecule was used, however for the aromatic form, the cyano-groups were cleaved. This allowed for fully relaxed structures to be used in both simulations while capturing the correct bond length alternation observed in each conjugated core. The UV-Vis absorption spectra were likewise calculated at the same level of theory, using the 10 lowest singlet and triplet states in the TD-DFT calculation. All calculations were performed using Gaussian16 Rev. B. Side chains were removed for computational efficiency. In this case, the quinoidal geometry optimization was allowed to relax fully, while for the aromatic geometry the carbon atoms along the backbone were fixed to enforce the proper aromatic single-double bond alternation pattern (i.e., that opposite the quinoidal bonding pattern) and the result of the structure was allowed to relax.

CHAPTER 4: CONTROLLING POLYMORPHIC PHASE TRANSITIONS THROUGH ALKYL CHAIN ENGINEERING

4.1 CHAPTER OVERVIEW

Control of polymorphic behavior is crucial for designing functional organic semiconductor devices as even slight structural difference may translate to dramatically different electronic properties and is ubiquitous in organic molecules. One route to controlling polymorphism is through phase transitions, which allow for stabilizing a particular crystal structure. However, despite advances in predicting polymorphic structures, these transitions are still typically found through serendipitous investigations and the molecular design characteristics governing the polymorphic behavior remains largely unknown. Here, we systematically investigate a series of molecules with varying alkyl side chain lengths and observe modulation of two previously reported phase transitions that exhibited distinct transition mechanisms. In the three molecular systems, we observe that shortening the alkyl chain past a critical length suppresses a cooperative phase transition by eliminating the alkyl chain potential to drive the transition. On the other hand, the nucleation and growth transition temperature was modulated based on the melting point of the tethered alkyl chains, increasing the temperature with decreasing chain length. This was also found to modulate the associated quinoidal to aromatic biradical switching that drives the transition, suggesting a synergy between the crystal structure and electronic structure. Ultimately depending on the exact mechanism of the phase transition, adjusting the alkyl chain length may lead to minor tuning of the phase transition temperature or suppression of the transition altogether. This offers a potential molecular design rule to target a particular transition mechanism based on the desired behavior for the system.

4.2 INTRODUCTION

The correlation between polymorph discovery and the time and effort spent researching a compound was famously proposed by McCrone in 1965[147]. Since then, the time and effort of countless graduate students has been devoted to identifying an innumerable catalog of crystal structures (see CCDC[148]). While tremendous progress has been made in the prediction and access of various crystal structures, even today polymorphism is often found serendipitously. The importance of these structures is critical: polymorph selection in a crystal can dramatically modulate properties such as solubility of pharmaceuticals[149], electronic properties of semiconductors[25,102,150] and mechanical properties of metal alloys[5,94,151]. Accessing polymorphic structures in a controlled and predictable way is necessary to realizing next generation material properties. Polymorphic transitions, induced by external stimuli (e.g. heat[100,103], light[152,153], mechanical[5,37]) is one method to control the crystal structure. Understanding how these transitions occur and how the molecular design impacts them offers the potential for developing molecular design rules to encourage, tune or even suppress this polymorphic behavior.

Polymorphic transitions not only provide a route to polymorphic selection for a particular desired property, but also allow for incorporation switching behavior based on transition related effects related to the underlying mechanism (reversibility[103,154], rapid switching[107,151], mechanical changes[96,107,155]). Transitions may occur by two different mechanisms: either via a nucleation and growth transition[156,157], where the molecules move individually across a phase boundary, or by cooperative transition[43,118,158,159], in which molecular motion is displacive and concerted. Typically, nucleation and growth transitions exhibit large changes in molecular packing and slow kinetics[37], making it promising for the kinetic stabilization of a particular metastable polymorph. Cooperativity on the other hand, exhibits rapid transition kinetics[97,151] and low energy barriers[94,99], and is coupled with intriguing mechanical properties[5,100,107], offering pathways to novel, reversible switching devices. By controlling the presence of these transitions, we may provide a method of rationally designing new switching devices.

Previously, Cooperative transition mechanisms have typically involved rotational[5,100,118], or sliding within the crystal system[96,107,158]. In organic molecules, this motion has typically been facilitated by the side chains of the molecules which have shown to go through a rotational order-disorder[100,106] transition or undergo a conformation change in the case of alkyl chains[160]. In our recent work[117,160], we observed 2DQTT- C_8C_{10} undergoes two thermally accessible phase transitions, the I-II (cooperative) and II-III (nucleation and growth) transitions. The I-II cooperative was driven by a change in alkyl chain conformation, causing a change in the tilt of the molecules along the π-stacking direction, in a domino like effect. Whereas the II-III nucleation behavior was driven by biradical formation, a unique electronic ground state formed in quinoidal molecules[161–163] and results in unique intermolecular interactions[17–19,98]. This change in the core-core interactions was facilitated vial melting of the alkyl chains, which allowed increased mobility. In both cases, the alkyl chains played a key, yet distinct, role in the phase transition, suggesting a potential route to controlling the behavior via adjusting the structure of the alkyl chains.

In this work, we report the control of polymorphism in 2-Dimensional quinoidal terthiophene (2DQTT) via tuning the chain length of the branched alkyl group. In the case of the I-II cooperative transition, when the side chains hit a critical length below C_6C_8, the transition is no longer observed. Raman spectroscopy and single crystal X-ray diffraction (SCXRD) showed the C_2C_4 molecule packed in a polymorph II like structure at room temperature, eliminating the driving force behind the transition. On the other hand, the II-III nucleation and growth transition temperature increases with shorter side chain length due to a higher melting temperature for shorter tethered alkyl chains in the solid state. Finally, we observed a synergistic effect between the polymorph III crystal structure and biradical formation, which seems to be mediated via the alkyl chain melting, providing a new way to modulate biradical stability.

4.3 RESULTS AND DISCUSSION

Polymorphic Transitions of 2DQTT Systems. Previous work[117] on 2DQTT- C_8C_{10} showed two thermally induced phase transitions, occurring at 164 °C and 223 °C, designated I-II and II-III respectively. While the I-II exhibited a cooperative type mechanism and the II-III transition showed nucleation and growth behavior, both transitions relied on key changes in the alkyl chains.

A series of 2DQTT molecules with different branched alkyl chain lengths were synthesized (**Figure 4.1**) were synthesized according to previous work to elucidate the molecular design criteria governing the polymorphic behavior observed in the C_8C_{10} system. From the original C_8C_{10} molecule, the side chains were systematically shortened to C_6C_8 and C_2C_4, decreasing the bulkiness and flexibility of the chains in the process. Single crystals of each molecule were crystallized into the stable polymorph at room temperature for all three systems. We note that while the C_8C_{10} and C_6C_8 molecules were grown from a mixture of DCM and EA, in the C_2C_4 system, this method produced a metastable polymorph previously reported. To access the stable form, slow growth from tetralin was used instead.

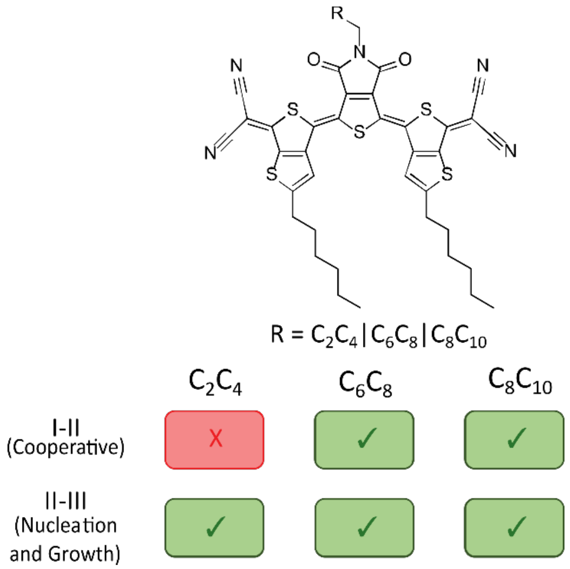

	C_2C_4	C_6C_8	C_8C_{10}
I-II (Cooperative)	X	✓	✓
II-III (Nucleation and Growth)	✓	✓	✓

Figure 4.1. Schematic of 2DQTT with a summary of the polymorphic transitions observed in each target alkyl chain motif.

Crystals of each molecule were investigated under hot stage polarized optical microscopy (POM). We observed both the I-II and II-III transitions in the C_6C_8 and C_8C_{10} crystals, but only a single transition was found in the C_2C_4 crystals, which was assigned to the II-III transition, as discussed later. The I-II transition occurred at similar temperatures in the C_6C_8 and C_8C_{10} crystals (169 °C and 163 °C for C_6C_8 and C_8C_{10}, respectively) and showed the rapid kinetics as well as sharp phase boundaries that are hallmarks of the cooperative behavior (**Figure 4.2a,b, Movie C1,2**). However, crystals of C_2C_4 showed no transition in the temperature region expected suggesting the shorter side chains suppressed the cooperative I-II transition altogether (**Movie C3**).

On the other hand, the II-III transition persisted across all three molecular system. The nucleation and growth behavior clearly showed in the diffusive phase boundary and formation of multiple phase boundaries (**Figure 4.3a-c, Movie C4-6** respectively). The characteristic increase in brightness was also observed in each of the crystals, however the transition temperature is significantly higher in the C_2C_4 molecule (~20 °C), relative to the longer molecules. Initially, this difference in temperature coupled with the lack of a I-II transition may suggest this so called "II-III" transition was completely different structural behavior was found in the C_2C_4 system, unrelated to the II-III transition in the longer alkyl chain molecules. While such a shift in transition temperature is substantial, similar effects have been observed for transitions involving alkyl chain melting. In a tethered state, the shorter alkyl chains reduce steric hinderance in the crystal and allow for stronger forces such as π-π interactions between the cores to dominate. The C_2C_4 transition still bears a qualitative resemblance to the II-III transition in the C_6C_8 and C_8C_{10} molecules suggesting these transitions still share the same underlying mechanism.

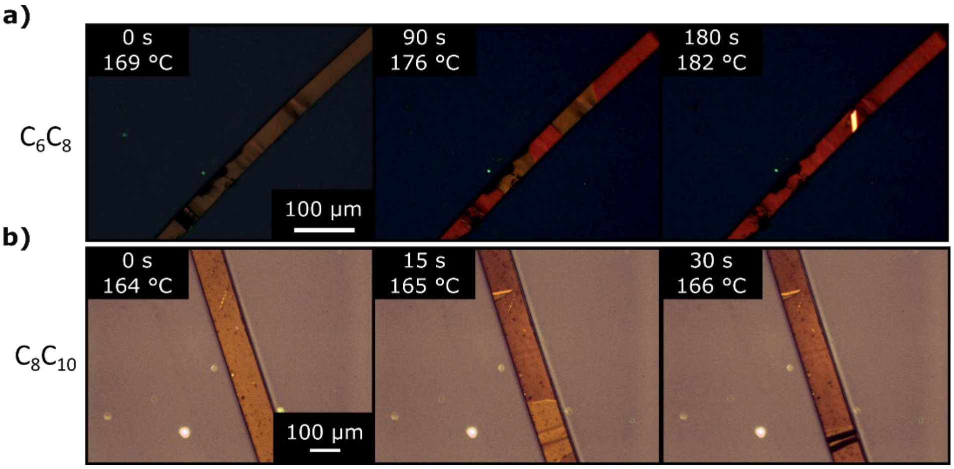

Figure 4.2. In situ POM images during the I-II transition in the C_6C_8 (a) and C_8C_{10} (b) crystals.

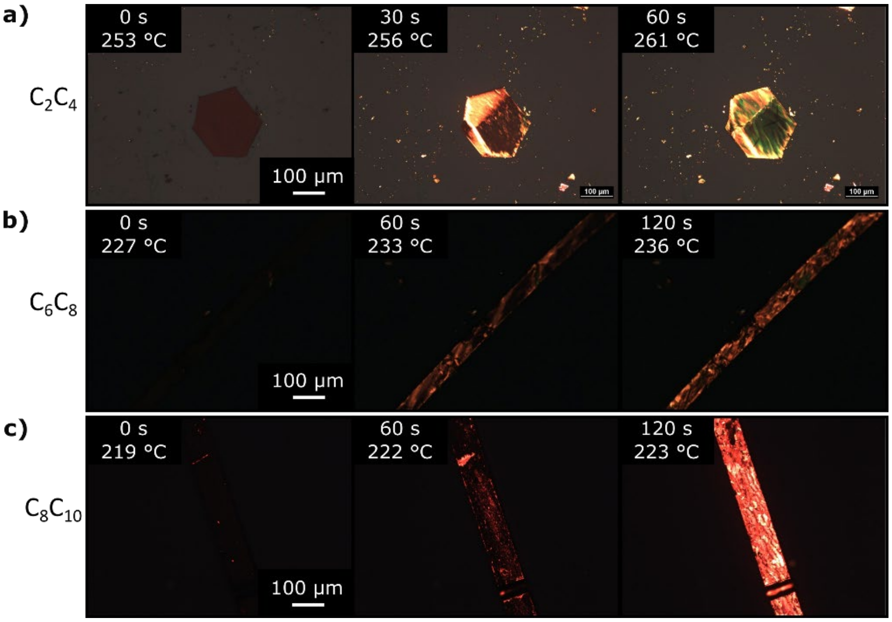

Figure 4.3. In situ POM images from the II-III transition observed in crystals of C_2C_4 (a), C_6C_8 (b) and C_8C_{10} (c).

Suppression of Cooperativity in the I-II transition. To investigate the underlying reason for the loss of the I-II cooperative transition, single crystal structures were compared for each molecule system. Both the C_6C_8 and C_8C_{10} formed a C2/c unit cell, with a glide plane perpendicular to the b direction, while The C_2C_4 crystal packs in a $C2_1/c$ unit cell, adding an additional screw symmetry not found in the other systems. In all three cases, the conjugated core forms 1-D π-stacking along the b-direction of the unit cell (**Figure 4.4a-c**). This also results in a layered structure, separated by greasy layers, when viewed from the side (**Figure 4.4d-f**) and based on the BFDH morphology, we expect this stacking to occur out of plane relative to the substrate (**Figure C1**). Upon closer inspection of the C_2C_4, we notice the conjugated core when viewed in **Figure 4.4a** appears to have a higher tilt with respect to the substrate as compared to the C_6C_8 and C_8C_{10} structures (**Figure 4.4 b,c**). In fact, by measuring the angle between the average plane of the conjugated core and the (100) plane (or the (001) for C_2C_4), we see that the C_6C_8 and C_8C_{10} molecules pack at a tilt of 66° and 67°, respectively, whereas the C_2C_4 molecule is tilted to 88°, nearly perpendicular to the substrate (**Figure C2**). In previous work, I-II the mechanism proposed an increase in the tilt angle driven by a change in the alkyl chain conformation. The room temperature crystal structure of the C_2C_4 molecule suggests the packing may already be similar to that of polymorph II found in the C_6C_8 and C_8C_{10} systems without the transition. We hypothesized that perhaps the reduced bulkiness of the shorter chains allowed the alkyl chains to initially adopt the polymorph II conformation at room temperature.

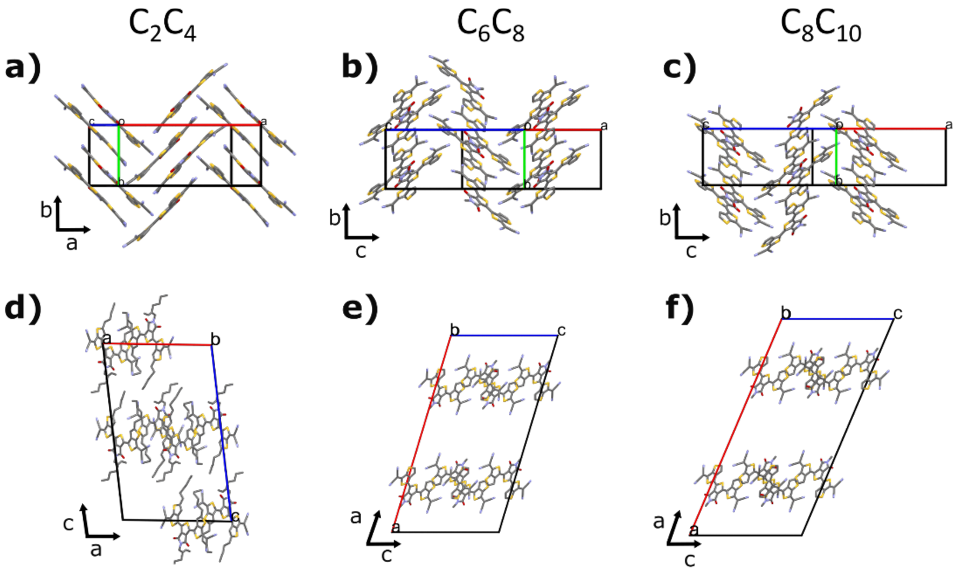

Figure 4.4. Molecular packing of the 2DQTT systems. 1-D π-stacks form along the b direction for all 3 systems (a-c). Similar out of plain layering of the molecules, where the alkyl chains (omitted for clarity) fit in between the layers of 1-D stacks (d-f).

Assessing the conformation requires understanding the behavior of the alkyl chains in each of these systems. Raman spectroscopy provides detailed information on the chemical environment of the molecules in the crystal structure and was performed on the crystals during heating. Previous work[160] on the I-II transition showed significant changes in the peak at 1409 cm^{-1}, which was assigned to the CH_2 deformation vibrational mode($\delta(CH_2)_{alkyl}$), located in the alkyl chains (**Figure 4.5a,b** red). The peak at 1387 cm^{-1} on the other hand, was assigned to the effective conjugation coordinate (ECC) mode of the quinoidal core, providing a consistent reference for comparison (**Figure 4.5a,b** blue). With this assignment, we tracked the $\delta(CH_2)_{alkyl}$ in each system. Despite the similar packing motifs for each molecules, the room temperature spectra for the C_2C_4 crystal shows a significantly reduced intensity of the $\delta(CH_2)_{alkyl}$ peak, as compared to the other systems (**Figure 4.5b**), suggesting a very different starting environment for the alkyl chains in the C_2C_4 structure. As expected from the lack of transitions observed during in situ POM experiments, no significant changes occurred to the C_2C_4 Raman spectra during heating up to 250 °C (**Figure 4.5c**).

In the C_6C_8 we see clear changes to the Raman spectra similar to the C_8C_{10} crystals previously studied (**Figure 4.5d,g**). In both cases, there appears to be a decrease in the intensity of the $\delta(CH_2)_{alkyl}$ peak during transition. We note that the C_6C_8 crystal transitions at a temperature of

140 °C, significantly lower than observed under in situ POM, however we expect this is due to local heating from the laser. On the other hand, the C_8C_{10} sample matched the POM transition closely because the crystal was formed via dropcasting, resulting in a much smaller crystal and less laser absorption. We fit the $\delta(CH_2)_{alkyl}$ and $\nu(C{=}C)_{ECC,Q}$ peaks to track the intensity ratio (based on peak area) during the transition. Indeed, for the I-II transition, both the C_6C_8 and C_8C_{10} systems shows a sudden drop in the intensity of the CH_2 deformation peak ($\delta(CH_2)_{alkyl}$), relative to the conjugated core stretching mode ($\nu(C{=}C)_{ECC,Q}$) (**Figure 4.5e,h**). This is also coupled by a simultaneous redshift in the $\delta(CH_2)_{alkyl}$, indicative of the significantly different chemical environment of the alkyl chains in polymorph II. This confirms that the cooperative behavior observed in both crystals undergoes an identical transition mechanism in both molecular systems.

Comparing this behavior to the C_2C_4 case, the Raman spectra collected from C_6C_8 and C_8C_{10} crystals bear a remarkable resemblance to the room temperature C_2C_4 spectra. Particularly, the reduced intensity of the $\delta(CH_2)_{alkyl}$ signifies a similar environment of the alkyl chains between polymorph II (in C_6C_8 and C_8C_{10} crystals) and polymorph I in C_2C_4 crystals. This is coupled with the previous discussion of the single crystal structure showing a much larger tilt angle in polymorph I of the C_2C_4 crystals, another key feature of Polymorph II in C_6C_8 and C_8C_{10} crystals. This suggests the extra bulkiness of the longer alkyl chains (C_6C_8, C_8C_{10}) forces a smaller tilt angle, preventing the molecules from standing up, like loading a spring. Then once a high enough temperature is reached, that spring is released as the alkyl chains rearrange into the polymorph II conformation and the core is allowed to tilt up. This scenario is thus impossible in the shorter C_2C_4 side chain that already allows for this packing in the initial crystal structure.

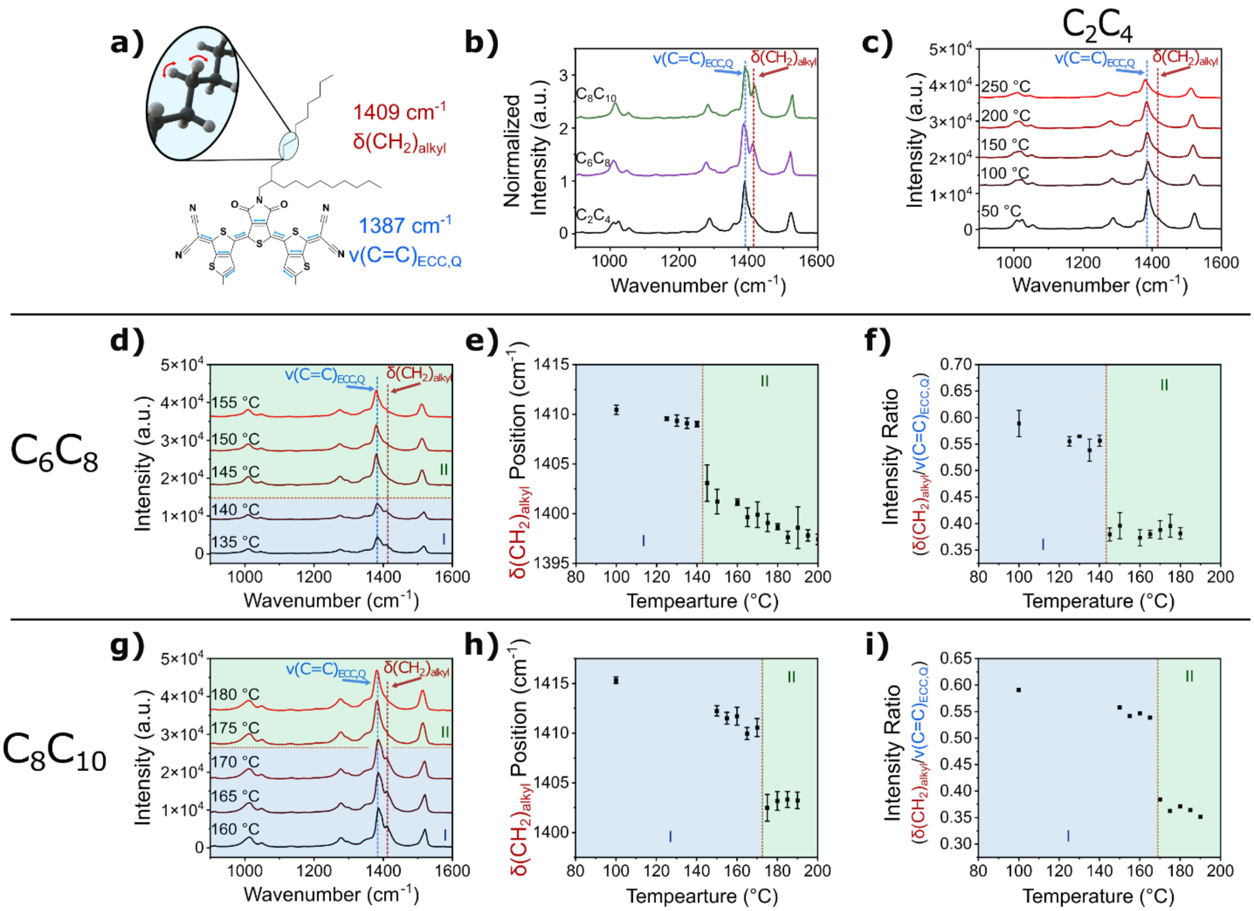

Figure 4.5. In Situ Raman spectroscopy during the I-II transition. (a) Raman spectra of C_2C_4 crystals showing no significant change in the range 50-250 °C that would contain the I-II transition. Comparison of the $\delta(CH_2)_{alkyl}$ peak for the C_2C_4 (black), C_6C_8 (purple), and C_8C_{10} (green) crystals. (c) Schematic showing the $\nu(C=C)_{ECC,Q}$ and $\delta(CH_2)_{alkyl}$ vibrational modes associated with the 1387 and 1409 cm^{-1}, respectively. Raman spectra of the C_6C_8 (d) and C_8C_{10} (g) crystals during their respective I-II transition. Change in the $\delta(CH_2)_{alkyl}$ relative intensity (e,h) and peak position (f,i) for the C_6C_8 and C_8C_{10} crystals, respectively.

Modulation of II-III transition. Where reducing the length of the alkyl chains disrupted the I-II transition mechanism, preventing observation of the cooperative behavior, a nucleation and growth transition was observed in all three systems. In analysis of the II-III transition mechanism in the C_8C_{10} crystals, four Raman peaks clearly described what was happening in the crystal. The two peaks at 1025 and 1063 cm^{-1} were assigned to C-C stretching of the trans and gauche conformers in the alkyl chains (Figure 4.6a pink and green). These peaks have been well studied in alkane molecules, and the intensity ratio between these peaks represents the disorder in the alkyl chain, where a ratio of 1 represents freely moving and rotating chains in a disordered state. The II-III transition also exhibits a quinoidal-to-aromatic transition within the conjugated core, stabilizing a biradical ground state[160], which is represented by the peaks at 1387 and 1442 cm^{-1}.

The peak at 1387 cm^{-1}, as discussed previously represents the quinoidal ECC mode of the core C=C stretching ($\nu(C{=}C)_{ECC,Q}$), whereas the 1442 cm^{-1} was shown to be the ECC mode for the aromatic core C=C stretching ($\nu(C{=}C)_{ECC,A}$) (Figure 4.6a blue and orange). In previous work, this ratio was shown to correlate with an increase in concentration of spins observed under electron paramagnetic resonance (EPR) spectroscopy and provides a ratio between the quinoidal and biradical species within the system.

Raman spectroscopy from the transitions in the C_2C_4 and C_6C_8 molecules follow similar changes to the vibrational modes observed in the C_8C_{10} molecule (Figure 4.6 b,e,h), confirming our expectations from in situ POM. Indeed, in all three systems, the alkyl chains become more disordered during the II-III transition, as the ratio of the trans (pink) to gauche (green) conformers approach 1 (Figure 4.6c,f,i). This further confirmed the clear shift in the II-III transition temperature observed under POM, which matched the temperature of the alkyl chain melting. Despite the differing initial structure of the C_2C_4 molecule, this transition still follows an identical pathway as the II-III transition in the C_6C_8 and C_8C_{10} molecules. We suspect the alkyl chain modification does not impede the biradical driving force beyond the necessity of increased molecular mobility from the melted alkyl chains.

What was unexpected, however, was the biradical formation behavior. In our previous work, we showed that the II-III transitioned is accompanied by a shift in the aromatic, biradical nature of the molecule with temperature. This change in π-π interactions was expected to be the driving force for this transition, which could be accommodated by the increased mobility from the melted side chains. The stabilization of the biradical form has been observed with increasing temperatures previously, but the key factor in stabilization is the extent of conjugation. The longer the conjugated core, the more stable the terminal radicals become and can further be tuned by adding various electron donating or withdrawing groups[17,98,111,161]. Interestingly, in all 3 cases, the formation of the aromatic core (orange), relative to the quinoidal core (blue), occurs simultaneously with the melting of the side chains. This results in the temperature for stabilizing the aromatic biradical form to increase to higher temperatures, despite no changes to the conjugated core of the molecule. To account for this, there must be a synergistic effect between the crystal structure and stabilization of the radicals. While such intermolecular interactions from biradicals have shown to be dominant, directing the crystal structure formation[164,165], which can lead to a competition between pseudo sigma bond and radical stabilization, it has been unclear whether the reverse is true in the solid state. Our results suggest that forming the right crystal structure can, in turn, stabilize radicals in a material that would otherwise exhibit a mostly quinoidal ground state.

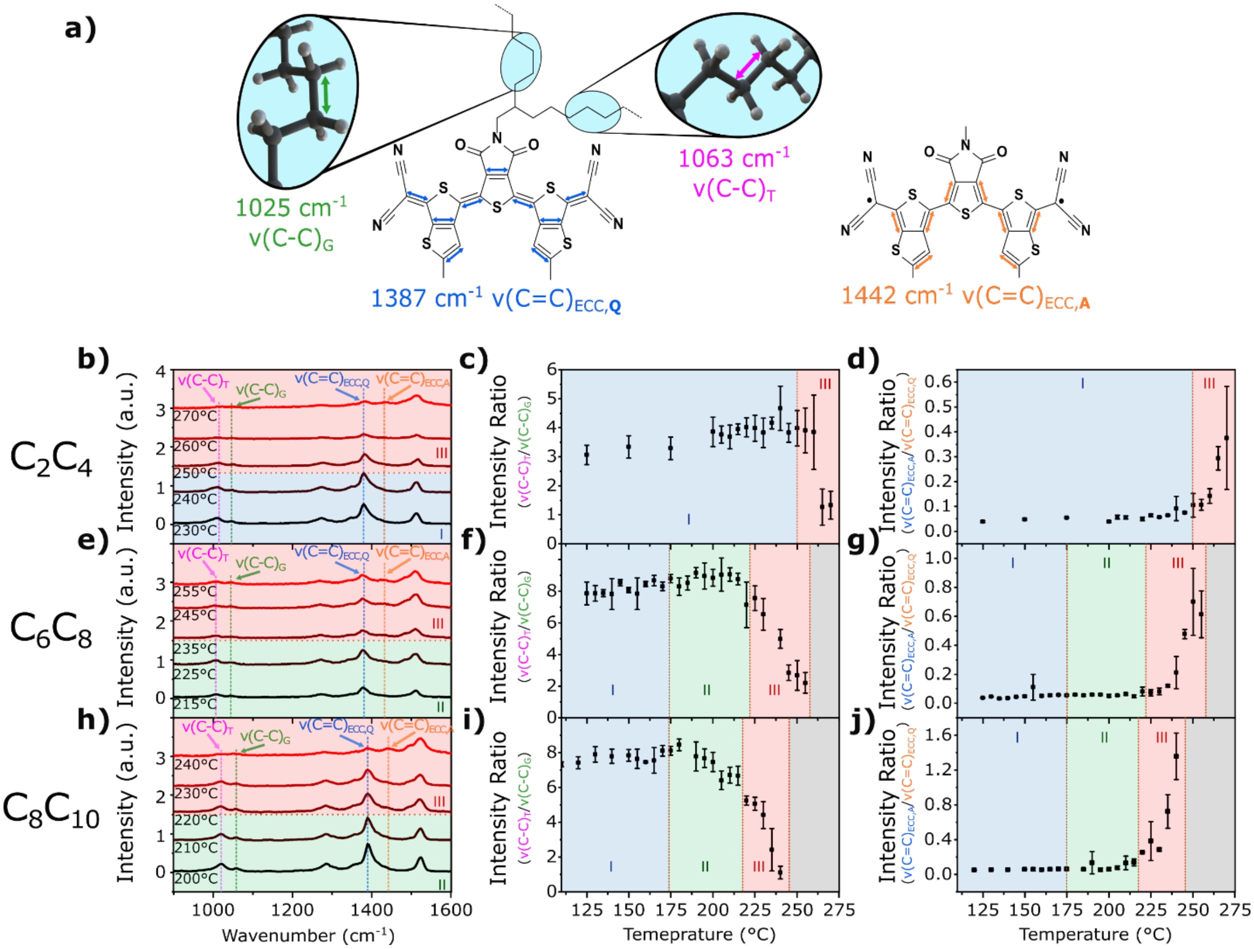

Figure 4.6. In Situ Raman spectroscopy during the II-III transition. (a) Schematic showing the vibrational modes for the C-C stretching in the trans (v(C-C)T, 1063 cm-1) and gauche (v(C-C)G, 1025 cm-1) conformers as well as the C=C stretching of the quinoidal (v(C=C)ECC,Q, 1387 cm-1) and aromatic (v(C=C)ECC,A, 1342 cm-1) forms. In situ Raman spectra during the II-III transition (b,e,h), for each crystal system, showing the changes in the trans and gauche peaks as well as formation of the aromatic peak. The trans to gauche intensity ratio approaches 1 for each system (c,f,i), showing the melting of the alkyl chains and is coupled with the aromatic to quinoidal intensity ratio increasing (d,f,j), indicating a synergy between the polymorph III structure and biradical formation.

4.4 CONCLUSIONS

The I-II and II-III transition behavior observed in the 2DQTT could be modified in distinct ways via tuning the branched alkyl chain length. Reducing the length of the alkyl chains effectively “turned off” the cooperative I-II transition by allowing a greater tilt in the molecule and forming a polymorph II like structure at room temperature. We observed the alkyl chains already packed in the expected conformation for polymorph II, eliminating the potential driving force of transition. On the other hand, reducing the chain length increased the “melting” point of the tethered alkyl chains. This shifted the II-III transition to higher temperatures and coupled the quinoidal to biradical electronic structure change. Such a synergy between structural transition and electronic transition provides novel modes of modulating the radical stabilization, beyond traditional tuning of conjugation length. Our results suggest that in the case of these branched chains, adjustments to the alkyl chain length can disrupt the observed cooperativity, while simultaneously tuning the nucleation and growth transition temperature, providing a route to targeting these transition behaviors.

4.5 MATERIALS AND METHODS

Materials synthesis. Synthesis of 2DQTT-o-B has been published in Reference 25 [108].

Single crystal fabrication. Single crystals of C_2C_4 were grown via slow evaporation from a 0.5 mg mL^{-1} tetralin solution to obtain hexagonal plates. Crystals of C_6C_8 and C_8C_{10} were grown via slow evaporation from a 1 mg mL^{-1} 1:1 mixture of dichloromethane and ethyl acetate. The solutions were then capped with parafilm and 1-5 holes were created in the film using a needle. The vials were then placed in a glove bag under nitrogen atmosphere for slow evaporation over a few weeks. The nitrogen in the glove bag was refilled every other day to prevent oxygen from reacting with the molecule and ensure saturation of solvent vapors did not occur. Crystals were removed from the mother liquid prior to complete drying. Crystals of C_8C_{10} for Raman spectroscopy were grown via drop casting 5-15 µL of 10-15 mg mL^{-1} of 2DQTT-o-B dissolved in a 1:1 mixture of dichlorobenzene and decane, heated to 100 °C. Dropcasting was done onto PTS-treated silicon wafers (SiO_2/Si) and allowed to dry overnight.

Polarized optical microscope. Single crystals grown under the slow evaporation procedure were placed under a Nikon H550S with a high-speed camera (Infinity 1) and heating stage (Linkam 402). The chamber was sealed with a magnetic lid and O-ring during heating. The temperature ramp was kept at a constant 5 °C min^{-1}. Videos were recorded at framerates ranging from 1 to 7.5 fps.

Raman Spectroscopy. A Raman confocal imaging microscope with a 532 nm laser (Laser Quantum Ventus 532 with max power 50 mW) and 50× long working distance objective lens (HORIBA LabRAM HR 3D) equipped with HORIBA Synapse back-illuminated deep-depletion CCD camera was used to collect spectra. Using a 300 g mm^{-1} grating, we used a scan exposure time of between 20-60 s. An optical density filter of OD = 1 was used (OD = log(power transmission factor)), and no beam damage was observed except at only the highest temperatures after prolonged periods of laser exposure (>5min). To eliminate this effect, each spectrum was recorded in a new position on the crystal to prevent overexposure of any particular area. For variable-temperature experiments, the samples were collected using a Linkam THMS600 heating stage with a closed chamber. The heating and cooling rate was kept at 10 °C min^{-1}. Each temperature was equilibrated until the temperature reading stabilized and the Raman laser was refocused to account for substrate thermal expansion (approximately 5 minutes in total).

Single Crystal X-ray Diffraction. The Single crystal structure for the C_6C_8 crystal was collected at NSF’s ChemMatCARS (Sector 15) of the Advanced Photon Source, Argonne National Laboratory. Needle crystals grown via slow evaporation from 1:1 dichloromethane and ethyl acetate and measured at room temperature. The beam energy was 30 keV (0.41328 Å), and the beam size at the sample was 0.15 × 0.15 mm2. 720 frames were taken using a Huber 3 circles diffractometer with a kappa angle offset of 60° and a Pilatus 1M (CdTe) detector. The sample to detector distance was 130 mm and was collected at 2 θ-angles at 0° and ω-angles at -180°, followed by two different kappa angles, 0° and 15° respectively. The ϕ-angle was scanned over the range of 360° using shutterless mode. The single crystal structure was analyzed using Mercury software to calculate the tilt of the conjugated core with respect to the (100) or (001) plane.

CHAPTER 5: LASER WRITING OF POLYMORPHIC TRANSITIONS FOR NEUROMORPHIC COMPUTING

5.1 CHAPTER OVERVIEW

Neuromorphic devices offer a potential low energy alternative to tradition Von Neumann architecture for accelerating AI and deep learning algorithms. These devices are based on memristor systems to act as neural synapses, providing a method to tune and remember the conductance of the devices to many potential levels, effectively encoding the weight into the conductance state. We utilize kinetic trapping of the II-III transition in 2DQTT-o-B, an n-type organic semiconductor, to access a metastable polymorph IV which shows distinct symmetry and packing as observed through grazing incidence X-ray diffraction (GIXD) with >2 orders of magnitude lower conductance than polymorph I with no required gate voltage. Using a laser in conjunction with the PolyChemPrint platform, we direct the local heating to recover the IV-I transition. This is confirmed via a combination of GIXD and Raman spectroscopy. Moreover, we observe formation of an optically induced biradical state in the polymorph I structure which causes a self-doping effect, switching polymorph I into more metal like behavior. Finally, we show using a phase change memory device, we can tune the conductance state via controlling the number laser lines written, allowing for reliable, laser written memristor devices.

5.2 INTRODUCTION

Neuromorphic computing has emerged as an efficient competitor to traditional Von Neuman architectures. The umbrella of neuromorphic devices tends to capture a wide diversity of potential alternative architectures, such as synaptic neural networks that encompass spiking based devices or more classical artificial neural networks[166–168]. However, all of these devices take inspiration from biological behavior through the implementation of memristors, as opposed to transistors, and delocalization of memory in a synapse-like structure[169]. This has become particularly relevant with the proliferation of machine learning algorithms, capable of taking advantage of these synapse-like architectures for extremely efficient inference calculations.

Development of materials for these memristors is critical to defining how these neuromorphic devices operate in terms of resistive state reading and writing, as well as stability and cycling. One promising method is the use of phase change memory, which utilizes amorphous-to-crystal transitions observed in many inorganic systems based on Ge, Sb or Te[166,170–172]. These setups use a series of voltage or laser pulses to adjust the conversion between the two states which exhibit conductance changes across several orders of magnitude. However, the distribution of conductance after pulsing has significant variability in the set state, causing difficulties in reliable definition of multiple states.

Organic electronic materials offer the opportunity of solution processing and compatibility with flexible substrates. Recently, a number of potential memristive mechanisms[168] have been reported in organic semiconductors, from conductive filament formation[173] to electrochemical doping using solid or liquid based electrolytes[174], allowing for a continuum of conductive states. However, most of these opportunities suffer from poor state retention time, lasting on the order of minutes to hours. On the other hand, organic molecules also exhibit ubiquitous polymorphism, with the ability to tune electronic properties by orders of magnitude[23,102,117]. This polymorphism can even be tuned via the vast molecular design space, such as side chain engineering, allowing for unique opportunities to rationally design transitions for phase change memory. The potential for these materials has been previously demonstrated via by Ribbierre and Aoyama et. al. (2010)[74,175] by inducing a phase transition in an quinoidal oligothiophene based molecule using laser writing for local heating, which switched between p- and n-type performance.

Recently, 2-dimensional quinoidal terthiophene (2DQTT-o-B) has shown promise for dynamic phase change electronics, exhibiting a diverse set of polymorphic transitions[80,108,111,112,117,160]. Utilizing the I-II cooperative shape change, a thermally induced switchable actuator was presented. On the other hand, the II-III transition exhibited a large hysteresis, allowing for the potential of kinetic trapping by quenching polymorph III. Moreover, the structure of polymorph III results from the formation of a unique biradical ground state observed in quinoidal systems, substantially altering the electronic properties. This high energy barrier, coupled with a 5 orders difference in electron mobility between polymorphs I and III provides an ideal opportunity for developing stable organic phase change devices.

Here, we report the use of the polymorphism observed in 2DQTT-o-B as a phase change based memristor. Utilizing quenching of polymorph III to room temperature, we accessed a structurally similar, symmetrically broken structure designated polymorph IV, with substantially different electronic properties. Using the PolyChemPrint platform[176], with a modified with a laser setup, local heating initiated the recovery polymorph IV to polymorph I transition, changing the conductance by 2 orders of magnitude with no gating voltage necessary. Decoupling the phase transition from the voltage application allows for direct control of where the transition occurs and limits relaxation from device operation allowing for reliable, well-defined states. This lasing also had the added effect of optically inducing a biradical state, offering further tuning of the optoelectronic properties of these quinoidal molecules. Via tuning of the laser power and exposure, coupled with the 3-axis control of a 3D printer, precise laser writing of polymorph I into a film of trapped polymorph IV allowed for fabrication of an 8 state memristor device.

5.3 RESULTS AND DISCUSSION

Kinetic Trapping and Characterization of Polymorph IV

Previous work showed that 2-dimensional quinoidal terthiophene (2DQTT-o-B) (**Figure 4.5.1a**) exhibits two reversible phase transitions. The II-III transition was found to have a large hysteresis of 75 °C by differential scanning calorimetry (DSC), with the reverse transition occurring below that of the initial I-II transition (**Figure 4.5.1b**), allowing for the potential kinetic trapping of this polymorph at room temperature under the confinement conditions of thin films. Thin films printed from chloroform at speeds 0.03-0.3 mm/s were printed according to the methods. Using polarized optical microscopy (POM) with a hot stage for in situ monitoring, films of 2DQTT-o-B were heated until the II-III transition was observed, indicated by the increased brightness and bright red color. After the intensity stopped changing, the film was removed from the microscope and immediately placed on a cool table, quenching the sample to room temperature. Upon cooling, the sample retained the high intensity from the original polymorph III, suggesting kinetic trapping (**Figure 5.1c**). These samples, when heated to 130 °C underwent a phase transition, significantly decreasing in intensity, suggesting reforming polymorph I, as suggested by DSC.

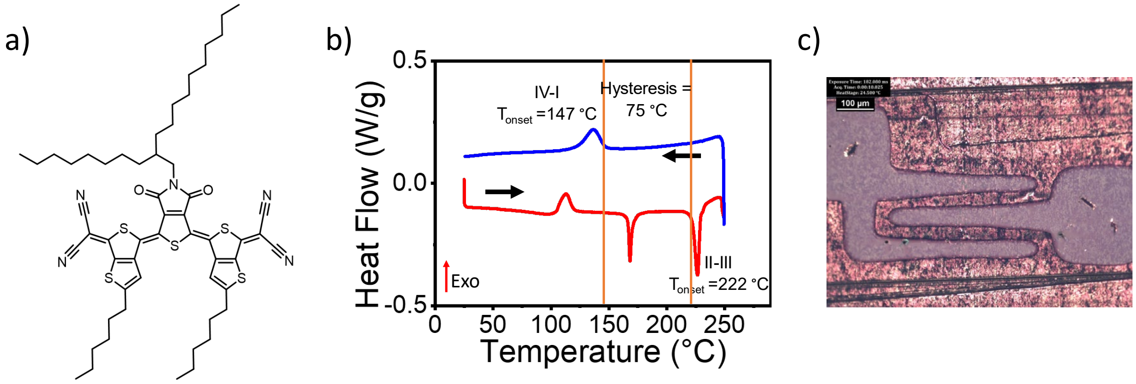

Figure 5.1. (a) Schematic of 2DQTT-o-B. (b) DSC showing the large 75 °C hysteresis for the II-III transition. (c) Trapped polymorph IV at room temperature.

To confirm this observation under in situ POM, we investigated the crystalline packing of these thin films using grazing incidence X-ray diffraction (GIXD). In previous work, polymorph III was characterized and a hexagonal unit cell was fit to the diffraction pattern (**Figure 5.2a,c**). To obtain the diffraction pattern of the trapped film, samples fabricated as discussed in the methods were heated under hot stage microscopy until the II-III transition was complete and quench cooled. While under typical laboratory conditions of 25 °C, the films are stable for several days, the temperature in the hutch at the synchrotron was higher at around 30 °C. These conditions compounded with energy from the X-ray beam to rapidly convert back to polymorph I before beam alignment could be completed. To combat this effect, samples were stored in freezer conditions up until the point of measurement, at which point the films were removed from the freezer and immediately measure after the alignment process, resulting in measurements at temperatures somewhere between 0 and 25 °C (**Figure 5.2b**). Despite these precautions, we note the weak presence of rods at q = 0.51 $Å^{-1}$ which appears to be the (02l) Bragg rod from polymorph I, slightly shifted due to the measurement occurring slightly below room temperature.

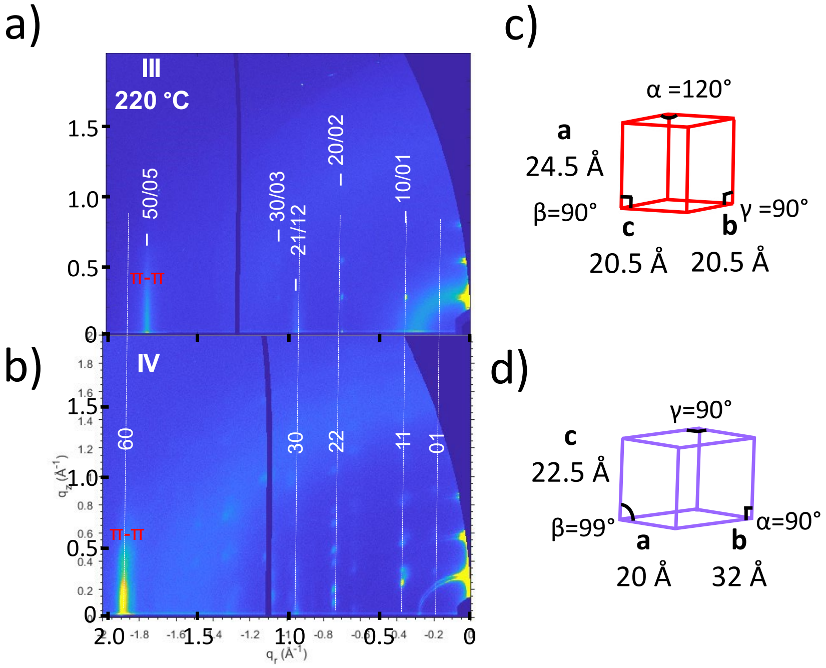

Figure 5.2. GIXD diffraction pattern for polymorphs (a) III and (b) IV. Extracted unit cells for polymorphs (c) III and (d) IV showing the symmetry breaking upon cooling to room temperature.

Comparing the diffraction pattern of the trapped films, designated polymorph IV, there appears to be substantially different symmetry from the polymorph III pattern (**Figure 5.2a,b**). We can see that while the (10l), (20l) and (21l) rods remain in similar locations (the only clearly observable rods from polymorph III), the peaks begin to split in the out of plane direction. Moreover, there is an appearance of a new rod at smaller q values suggesting a breaking of the trigonal symmetry. The resulting unit cell for polymorph was extracted using polymorph III as a starting point, making slight adjustments to the unit cell parameters and simulating the new unit cell until the simulation and experimental peaks matched (**Figure D1**). Under the redefinition of the unit cell based on the new monoclinic symmetry, the new rod appears to be the (01l) and the previous rods become the (11l), (22l) and (30l) rods respectively. This reduction in symmetry upon lowering temperature is typical but appears to occur without a clearly observed first order transition under either DSC or in situ POM. Additionally, we also observed significant changes in the π-π stacking distance, reducing from 3.56 Å in polymorph III to 3.33 Å in polymorph IV. While a decrease in distance is expected due to thermal contraction, particularly due to the lower than room temperature measurement, such a small π-stacking distance is quite uncharacteristic for

2DQTT-o-B. Previously, the smallest π-stacking distance observed was 3.45 Å in polymorph II, still substantially higher than the 3.33 Å in polymorph IV.

Laser setup, operation and optimization

Once kinetically trapped, we utilized a 6W, 450 nm laser diode from OptLaser, to induce local heating to recover the polymorph I state, per previous work. For this operation, PolyChemPrint developed by Patel and Diao et. al. (2021) offered a versatile, hardware agnostic platform to develop the laser writing technique[176]. Previous work showed the versatility of printing polymers from both melt and solution states via setting up an extruder and syringe pump. The printer is capable of directing position to the and with the addition of a laser engraver in place of the print head, provides laser writing capabilities as well. We modified the print head to hold an OptLasers PLH3D-6W 450 nm wavelength engraving laser head, which was compatible with most 3D printers (**Figure 5.3a**). A custom power supply was designed capable of interfacing with the PolyChemPrint software and incrementing the laser intensity in 0.1% increments. This setup allowed for detailed over several critical parameters determining the laser performance such as power, laser height, exposure time, print head speed, and number of exposure events.

In order to successfully write Utilizing the PolyChemPrint gcode software, a number of optimization programs designed to explore these different variables with the key of matching the local heating with kinetics of the IV-I phase transition. This entails accessing temperatures of ~130 °C for several seconds. In the process of this investigation, we observed substantial dependence on the thickness of the film, in which films printed at speeds >0.1 mm s^{-1} resulted in either no effect or sublimation and no clear conditions that result in transition. On the other hand, thicker films, printed <0.05 mm $^{-1}$ showed certain conditions that would access local transition to polymorph I in the region surrounding the exposed location (**Figure 5.3b,c**). Under the right conditions at 80% power 300 mm min^{-1} and 75passes, the emergence of a dark green polymorph I is quite apparent against the bright red polymorph IV (**Figure 5.3c**).

This structure was confirmed via GIXD by laser writing substrate long stripes across the substrate. Lines of the proper condition were drawn across the entire length of the substrate at regular intervals of 0.75 mm. These lasered lines were then aligned in the direction of the X-ray beam during measurement and GIXD images were taken at 0.25 mm intervals to show the changes between when the lasered regions were measured versus the non-lasered region. To prevent further conversion during the measurement process, a temperature stage was cooled to 0 °C using liquid nitrogen to reduce the IV-I transition rate. When measuring regions that remained unlasered, we clearly obtain a mixture of polymorphs I and IV, which occurs due to the edges of the substrate converting slightly over time (**Figure 5.3d,e**). This edge conversion likely results from either thickness differences from edge effects of printing, or increased nucleation from higher defect rates in the film near the substrate edge. Once the X-ray beam is aligned with the lasered lines, the low q Bragg rods associated with polymorph IV disappear showing pure polymorph I has been recovered.

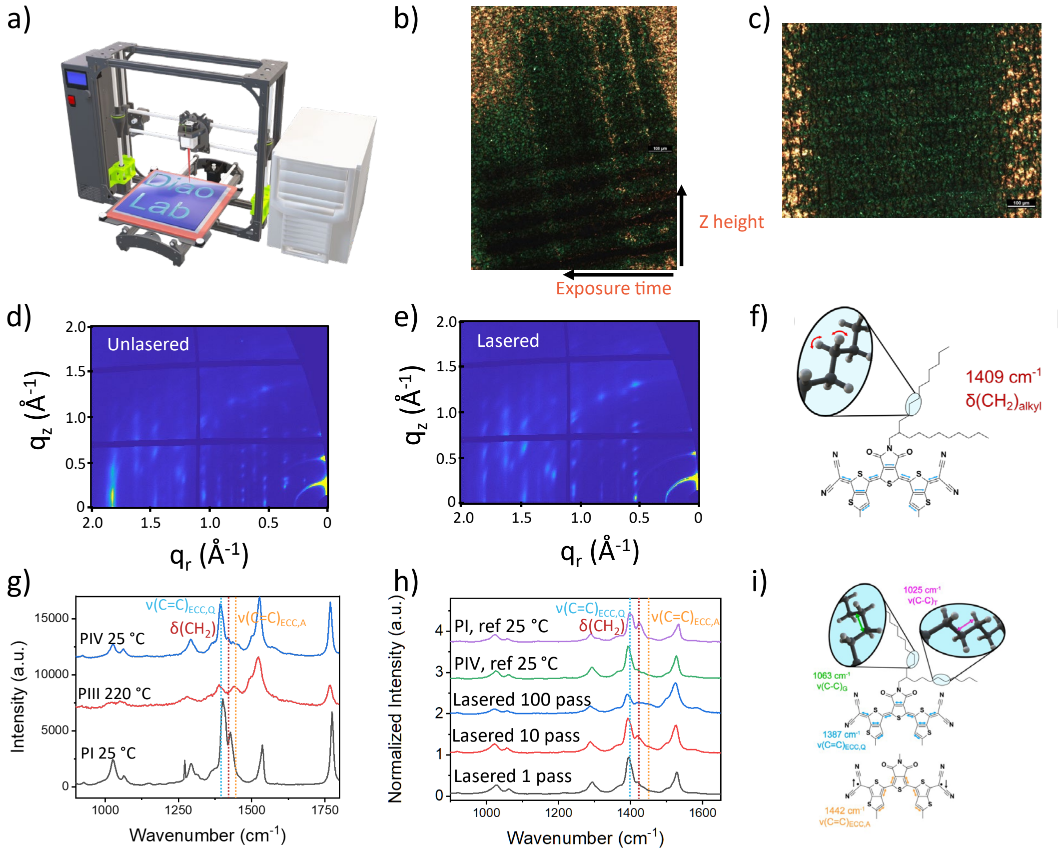

Figure 5.3. (a) Schematic showing the PolyChemPrint laser writing platform. POM images demonstrating the (b) parameter testing procedure and (c) working lasing parameters at 80% power, 75 passes and 300 mm min^{-1}. GIXD patterns of an (d) unlasered region showing a mixture of polymorph I and IV and (e) a lasered region showing the formation of pure polymorph I. Raman spectra (g) comparing polymorphs I, III and IV at their stabilized temperatures and (h) comparing changes with increasing laser exposure showing optical biradical formation. Illustrations depicting (f) the δ(CH$_2$)$_{alkyl}$ vibrational mode and (i) ν(C=C)$_{ECC,Q}$ and ν(C=C)$_{ECC,A}$ vibrational modes identified in the Raman spectra.

Additionally, we investigated the laser induced transition via ex situ Raman spectroscopy. Originally, Polymorph III was observed to have an increased biradical concentration that drove the II-III transition, but it was unclear how cooling to polymorph IV would affect this molecular structure. Based on our previous peak assignments for $\nu(C{=}C)_{ECC,Q}$ representing the quinoidal core stretching, $\delta(CH_2)$ indicating the CH_2 deformation, and $\nu(C{=}C)_{ECC,A}$ aromatic biradical stretching (**Figure 5.3f,i** 1387 cm^{-1} blue, 1409 cm^{-1} red, and 1442 cm^{-1} orange, respectively), we can analyze both the polymorph formation as well as biradical formation. Initially we characterized the Raman spectrum for the trapped polymorph IV film and compared with polymorphs I and III (**Figure 5.3g**). In polymorph IV the $\delta(CH_2)$ peak retains a reduced intensity similar to polymorphs II and III during in situ measurements. On the other hand, the biradical state clearly reduces as the $\nu(C{=}C)_{ECC,A}$ intensity returns to a low intensity as well. However, there are perhaps some residual aromatic biradical states not observed in polymorph I.

We also investigated the effects of laser inducing the IV to I transition to observe any potential degradation. Consistent with GIXD measurements, upon lasing across 10 passes, the $\delta(CH_2)$ starts to return to the polymorph I intensity (**Figure 5.3h**), implying successful transition back to polymorph I. However, at the same time, we show that with increasing number of lasing events (passes), there is a substantial increase in the aromatic vibrational mode at 1440 cm^{-1}. This results in a modest biradical residual at 10 passes, but increases substantially at 100 passes. This suggests an optical induction of the biradical form, which has been observed previously in several molecules[177–179]. Moreover, these radicals can additionally be extremely long lasting, with a half-life observed in 2-dimensional quinoidal quarter thiophene (2DQQT) up to 262 hours[180]. While we have yet to determine the half-life in this circumstance, the biradical state is clearly observable even after a few hours between lasing the sample and measuring the Raman spectra.

Phase Change Based Transistor and Memristor Device

Based on the results from GIXD showing significant differences in symmetry and extremely close π-stacking distance, we suspected very different electronic properties from polymorph IV. Initial tests investigated the single transistor devices. And indeed, we observed substantial improvement to device performance after quench cooling (**Figure 5.4a**). Polymorph IV showed more definition between the on and off states, but still exhibited much worse transistor performance than polymorph I, despite the significantly reduced π-stacking distance. On the other hand, the threshold voltage was significantly shifted more positive, results low current observed near a gate voltage of 0 V relative to that of polymorph I. This provides the ideal scenario for accessing at least two to three orders of magnitude in conductance states between these two polymorphs without the need for device gating, offering a low power phase change memory.

We then tested the recovery of device performance upon using the laser to induce the IV-I transition. Bottom contact devices were used to ensure that the entire channel region would be exposed and converted by the laser, which can be seen under non polarized microscopy in the trapped polymorph IV state (**Figure 5.4b**). Once again, we see high performance from polymorph I and reduction of performance upon trapping polymorph IV (**Figure 5.4d**) . Upon lasering of transistor devices based on the optimization process discussed above, we expected to see recovery of the transistor performance (**Figure 5.4c,d**). Interestingly, while the on state was almost completely recovered, the off state of the transistor showed a similar high off current behavior to polymorph II suggesting an increased population of stable radicals at room temperature. Based on previous work, recoverability from the high off current observed from polymorph II was shown via cycling through the I-II transition. Thus, we posit this effect must come from the laser induced biradicals resulting self-doping of the material.

The successful recovery of polymorph I allows for tuning the conductance state by tuning the number of laser lines written. To allow for the maximum number of states, devices based on a structure shown in **Figure 5.4e**, with long parallel contacts were fabricated and the beam width was focused to ~100 µm, the limit of the x-y resolution of the printer. The conductance was measured via two-point probe I-V measurements starting with a film completely converted to polymorph IV (**Figure D2**). Annealing to polymorph IV and trapping occurred in a glove box under nitrogen atmosphere. For each conductance state, the laser was manually aligned and incrementally moved along the device contacts and at each approximately 100 µm interval, a new line was laser written and the device was subsequently measured. This allowed for writing and measuring 8 unique states, shown in Figure 5.4f, and follows the expected trend for a device with two resistances in parallel, with the fraction of reach resistance slowly adjusted by lasing. This device covered two orders of magnitude of conductance without the need for additional gating of the device, utilizing only the conductivity change between polymorphs IV and I.

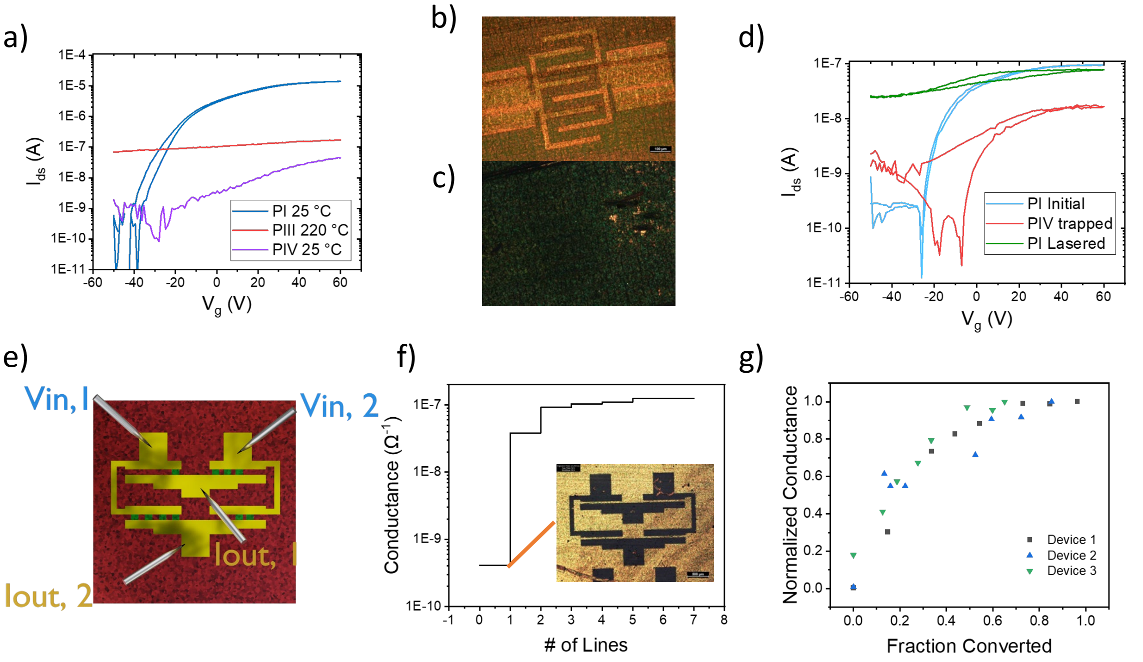

Figure 5.4. (a) Transistor performance comparison between polymorphs I (blue), III (red) and IV (purple) in top contact devices. (b) Non polarized optical microscope image showing a bottom contact device in the trapped polymorph IV state. (c) polarized optical microscope after lasing from polymorph IV to polymorph I. (d) device performance of bottom contact device before trapping (blue), after trapping polymorph IV (red) and after lasing to polymorph I (green) showing the recovery of the on state performance and self doping effect causing the high off current. (e) Schematic of artificial neural network matrix multiplier. (f) conductance states for a memristor device depicted in the inset. (g) Normalized characterization of 3 devices showing the potential for reliable conductance states once fabrication and alignment procedures are accounted for.

Moreover, this was repeated in two other devices. We note the differences in film quality (thickness, roughness, scratches etc.) and issues in precision of manually aligning the laser limited the replicability of each state based on the number of lines. However, once the conductance is normalized to the final fully converted state and the fraction of conversion is calculated based on the width of the channel (1000 µm) and the length of polymorph I converted in each state (**Figure 5.4g**), we can see each device reliably follows a similar trend. This confirms the use of laser writing in this device geometry for directing memristor states. Simply by operating the device at temperatures slightly below room temperature, reliable and stable conductance states can be established.

5.4 CONCLUSIONS

We investigated the potential of trapping polymorph III at room temperature through quench cooling. This led to the observation of significant changes to the symmetry related to the thermal contraction during cooling and on this basis was designated polymorph IV. The extraction of the unit cell revealed similar packing, but subsequent breaking of the higher hexagonal symmetry, likely resulting from relaxation of the molecules in the reduced temperature state. However, no first or second order phase transition was clearly observed during cooling under DSC or in situ POM. The characterization of this polymorph IV showed a modestly higher mobility of XX over high temperature polymorph III. At a V_g of 0V, the transistor device still showed significantly lower current, ideal for the memristive device.

Upon lasering of films with trapped polymorph IV, we recovered the structure of polymorph I, however a long lasting biradical state was also triggered through optical generation. This was able to recover a significant amount of the polymorph I conductance without need for gating. Ultimately this allowed for the formation of an 8 state memristor, promising stable well-defined states with further development of precision lasing and device fabrication.

5.5 MATERIALS AND METHODS

Thin Film Preparation. Thin film samples of polymorph I’ and I’’ used for experiments described in this work were printed onto trichlor(phenyl)silane(PTS) treated 300 nm SiO_2/Si wafers using solution shearing from 6 mg/mL solutions dissolved in chloroform at room temperature and chlorobenzene at 85 °C, respectively. A shearing speed between 0.1-0.5 mm/s was used in both scenarios with a blade gap of 100 µm. To transition the films to polymorph I, these films would be annealed at 100 °C for 30 minutes in the glovebox, until completely converted. We were also able to produce polymorph I’ films from dichloromethane and toluene solutions. A full table of deposition conditions and outcomes are available in **Table S1**.

Polarized Optical Microscopy. The thin film samples were placed in a Linkam LTS420 heating stage under a Nikon H550S with an Infinity 1 camera. Accessing the II-III transition, heating stage was left unsealed, and heating was performed at 20 °C min^{-1} up until approximately 270 °C (depending on ambient conditions), until transformation is complete. Upon complete transition, films were immediately removed and placed on the table, allowing the film to rapidly cool to room temperature and forming trapped polymorph IV films. Images of devices were obtained at room temperature under standard POM. Videos showing the change in transition behavior after transition were obtained via sealing the heating chamber and heating at 5 °C min^{-1} through the IV-I transition (147 °C) and II-III (222 °C) and videos recorded at 1 frame per second.

Raman Spectroscopy. A Raman confocal imaging microscope with a 532 nm laser (Laser Quantum Ventus 532 with max power 50 mW) and 50× long working distance objective lens (HORIBA LabRAM HR 3D) equipped with HORIBA Synapse back-illuminated deep-depletion CCD camera was used to collect spectra. Using a 300 g mm^{-1} grating, we used a scan exposure time of between 30 s. An optical density filter of OD = 1 was used (OD = log(power transmission factor)), and no beam damage was observed at room temperature. To eliminate any possibility, each spectrum was recorded in a new position on the film to prevent overexposure of any particular area.

Grazing Incidence X-ray Diffraction and Unit Cell Determination. GIXD was performed at beamline 8-ID-E of the Advanced Photon Source at Argonne National Laboratory[89]. The data were collected at 10.91 keV on a 2D Pilatus 1M detector. Ex situ measurements were conducted for polymorphs I' and I'' under vacuum at room temperature. Films of polymorph I were annealed as discussed above to access trapped polymorph IV samples. These films were stored in a cooler during transport and then in a freezer until measurement. Films were place on the sample holder and measured as quickly as possible to reduce the effect from the IV to I transition.

Lasered samples were obtained from films of trapped polymorph IV. Laser writing conditions were tested at laser powers from 80-95%, print speeds of 50-300 mm/min, laser height of 5.5-6.5 cm and 25-100 passes. Polymorph I was successfully converted at 6.5 cm, 80-95% power and print speeds 100-300 mm. Measuring these samples under GIXD required in situ measurements a low temperature to prevent the IV-I transition. The tests were conducted in a He environment with the sample on a commercial thermal stage (Linkam HFSX350-GI). The stage was set to 15 °C before removing the lasered samples from freezing conditions. Once on the Linkam stage, the temperature ramped at 20 °C/min to 0 °C and scans across the sample were performed at 0.5

mm increments to match the laser increments. GIXSGUI software was used to correct for detector nonuniformity, beam polarization and to reshape the 2D data into the representation q_z vs q_r[82]. The incident angle was set at 0.14° right above the critical angle for total reflectance of the organic thin film. Simulation of the unit cell and successive alterations were used to determine best-fit unit cells for Polymorph IV on the basis of the experimental peak positions (see supp. Info). The resulting unit cells were visualized using Vesta software[90].

Field-effect transistor fabrication and measurements. Using the 6mg mL^{-1} solutions in chloroform films of polymorph I' were printed on PTS treated 300 nm SiO_2/Si wafer from. A series of speeds from 0.03 to 0.05 mm s^{-1} were used. Top contact bottom gate devices were fabricated using a shadow mask and thermally depositing gold electrodes directly onto the film at a thickness of 35nm (Kurt J. Lesker Nano 36). The channel length and width are 800 µm and 40 µm respectively. Bottom contact devices were made using prefabricated gold contacts on 300 nm SiO_2/Si wafer silicon wafers. Prefabricated wafers were treated with PTS prior to printing from chloroform to produce films of polymorph I'. These devices were then annealed to polymorph I and measured for an initial state. Then they were annealed, either under in situ POM as discussed above or in the glove box on a hot plate set to 220 °C to undergo the II-III transition and then were rapidly quenched via removal from the hot stage to form polymorph IV devices. These were then subsequently lasered to produce the recovered polymorph I devices.

The resulting devices were then measured under a nitrogen atmosphere using a Keysight B1500A semiconductor parameter analyzer. The mobility and threshold voltage were then extracted from the saturation regime using the equation

$$\mu_{sat} = \left(\frac{\partial (I_{ds})^{\frac{1}{2}}}{\partial V_g} \right)^2 \frac{2L}{WC_i}$$

where I_{ds} is the drain current, V_g is the gate voltage, L=40µm is the channel length, W = 800 µm is the channel width and C_i = 11pF is the capacitance of the dielectric. A V_{ds} of 60V was used for all cases.

Memristor based fabrication and measurements. Similar to the transistor device performance, films of I' were printed on pts treated 300 nm SiO2/Si wafer. A memristor shadow mask was used to deposit 35 nm of gold contacts (Kurt J. Lesker Nano 36). The channel has a width of 50 µm and width of 1000 µm. The conductance was then measured under a nitrogen atmosphere using a Keysight B1500A semiconductor parameter analyzer in a two-point probe configuration measuring the I-V curves from -1 to 1 V and fitting the slope with a linear fit.

CHAPTER 6: CONCLUSIONS

While polymorphism has significant impact on the electronic and optical properties of organic semiconductors, the control over this behavior still proves elusive, particularly in understudied n-type systems. In this thesis, we explored the polymorphism of 2DQTT-o-B, a high performing n-type organic semiconductor and uncovered at least 5 previously unreported polymorphs with a diverse range of both structural and electronic characteristics. Utilizing in situ POM and DSC, I mapped out the polymorphic phase space in the thin film state showing 2 metastable forms at room temperature accessible via different solvents. Moreover, we showed two reversible phase transitions accessed through heating of the film. This allowed for the tuning of electron mobility by 5 orders of magnitude through polymorph selection. As n-type organic semiconductors are integral to developing full logic gates, understanding the polymorphic behavior of these systems is necessary for manufacturing high performance devices.

Along with a rich diversity of structures, we observed and compared both a nucleation and growth mechanism and a cooperative mechanism. I compared the kinetics of these 2 transitions in depth via in situ POM videos of the single crystal transitions. Classic cooperative behaviors such as thermosalient motion and avalanches in the phase boundary were clearly evident in the I-II transition. While the II-III showed typical nucleation and growth behavior such as This allowed us to identify the molecular origins of those transitions using Raman spectroscopy, showing the importance of the alkyl chains in driving the cooperative behavior in the I-II transition. On the other hand, using I showed the formation of biradicals drives the nucleation and growth behavior of the II-III transition. This transition highlights the complex interdependence between electronic structure, molecular structure, and crystal structure. Identifying these key aspects driving the transitions potentially unlocks new ways to control the presence of these transitions.

I was able to show the power of this design rule through adjusting the length of the alkyl chains in the 2DQTT molecule. By shortening the side chains, I showed the packing of the crystals remained in a similar 1-dimensional π-stacks. Despite the similar packing motif, I found the cooperative behavior could be suppressed in the molecule with a C_2C_4 molecule whereas the molecules with longer alkyl chains exhibited the I-II transition. Moreover, the II-III transition temperature can be tuned, following a higher temperature with shorter side chains. While Raman spectroscopy showed identical mechanisms for each molecule, the temperature for transition increases as the side chain length is reduced. Along with the transition temperature, this affected the presence of the biradical state, providing a novel way to tune the stability of this state. The difference in effect of the alkyl chain length on the I-II and II-III indicates the necessity of understanding the transition mechanism to predict the effect on polymorph behavior.

Finally, I explored the potential of utilizing a laser to direct the polymorph transitions to write the electronic properties into a film. By quenching polymorph III to room temperature, we found a significant change in the structure, despite the lack of a first order phase transition. I developed a laser toolhead to work within the PolyChemPrint universal printing system. Utilizing the local heating from the laser, I successfully recovered the polymorph I structure in specified regions of the film. This resulted in observation of light induced biradical formation, showing a persistent self doping effect even at room temperature with stabilization time greater than several hours. Ultimately the recovery of polymorph I provided a platform to create stable resistance modes based on number of lines lasered. Utilizing these many states, I was able to demonstrate the operation of a memristor device for future neuromorphic devices.

REFERENCES

(1) Diao, Y.; Zhou, Y.; Kurosawa, T.; Shaw, L.; Wang, C.; Park, S.; Guo, Y.; Reinspach, J. A.; Gu, K.; Gu, X.; Tee, B. C. K.; Pang, C.; Yan, H.; Zhao, D.; Toney, M. F.; Mannsfeld, S. C. B.; Bao, Z. Flow-Enhanced Solution Printing of All-Polymer Solar Cells. *Nature Communications* **2015**, *6*, 7955–7955. https://doi.org/10.1038/ncomms8955.

(2) Rigas, G.-P.; Payne, M. M.; Anthony, J. E.; Horton, P. N.; Castro, F. A.; Shkunov, M. Spray Printing of Organic Semiconducting Single Crystals. *Nature Communications* **2016**, *7*, 13531–13531. https://doi.org/10.1038/ncomms13531.

(3) Handa, S.; Miyazaki, E.; Takimiya, K.; Kunugi, Y. Solution-Processible n-Channel Organic Field-Effect Transistors Based on Dicyanomethylene-Substituted Terthienoquinoid Derivative. **2007**, 11684–11685. https://doi.org/10.1021/ja074607s.

(4) Le, M. N.; Baeg, K.-J.; Kim, K.-T.; Kang, S.-H.; Choi, B. D.; Park, C.-Y.; Jeon, S.-P.; Lee, S.; Jo, J.-W.; Kim, S.; Park, J.-G.; Ho, D.; Hong, J.; Kim, M.; Kim, H.-K.; Kim, C.; Kim, K.; Kim, Y.-H.; Park, S. K.; Kim, M.-G. Versatile Solution-Processed Organic–Inorganic Hybrid Superlattices for Ultraflexible and Transparent High-Performance Optoelectronic Devices. *Advanced Functional Materials* **2021**, *31* (29), 2103285. https://doi.org/10.1002/adfm.202103285.

(5) Park, S. K.; Sun, H.; Chung, H.; Patel, B. B.; Zhang, F.; Davies, D. W.; Woods, T. J.; Zhao, K.; Diao, Y. Super- and Ferroelastic Organic Semiconductors for Ultraflexible Single-Crystal Electronics. *Angewandte Chemie International Edition* **2020**, *59* (31), 13004–13012. https://doi.org/10.1002/anie.202004083.

(6) Hasija, A.; Chopra, D. Potential and Challenges of Engineering Mechanically Flexible Molecular Crystals. *CrystEngComm* **2021**. https://doi.org/10.1039/D1CE00173F.

(7) Huang, R.; Wang, C.; Wang, Y.; Zhang, H. Elastic Self-Doping Organic Single Crystals Exhibiting Flexible Optical Waveguide and Amplified Spontaneous Emission. *Advanced Materials* **2018**, *30* (21), 1800814. https://doi.org/10.1002/adma.201800814.

(8) Briseno, A. L.; Tseng, R. J.; Ling, M.-M.; Falcao, E. H. L.; Yang, Y.; Wudl, F.; Bao, Z. High-Performance Organic Single-Crystal Transistors on Flexible Substrates. *Advanced Materials* **2006**, *18* (17), 2320–2324. https://doi.org/10.1002/adma.200600634.

(9) Zhai, Y.; Wang, Z.; Kwon, K.-S.; Cai, S.; Lipomi, D. J.; Ng, T. N. Printing Multi-Material Organic Haptic Actuators. *Advanced Materials* **2021**, *33* (19), 2002541. https://doi.org/10.1002/adma.202002541.

(10) Tsumura, A.; Koezuka, H.; Ando, T. Macromolecular Electronic Device: Field-effect Transistor with a Polythiophene Thin Film. *Appl. Phys. Lett.* **1986**, *49* (18), 1210–1212. https://doi.org/10.1063/1.97417.

(11) Schweicher, G.; Garbay, G.; Jouclas, R.; Vibert, F.; Devaux, F.; Geerts, Y. H. Molecular Semiconductors for Logic Operations: Dead-End or Bright Future? *Advanced Materials* **2020**, *32* (10), 1905909. https://doi.org/10.1002/adma.201905909.

(12) Zhang, Y.; Zheng, Y.; Zhou, H.; Miao, M.-S.; Wudl, F.; Nguyen, T.-Q. Temperature Tunable Self-Doping in Stable Diradicaloid Thin-Film Devices. *Advanced Materials* **2015**, *27* (45), 7412–7419. https://doi.org/10.1002/adma.201502404.

(13) Baumgarten, M. Tuning the Magnetic Exchange Interactions in Organic Biradical Networks. *Phys. Status Solidi B* **2019**, *256* (9), 1800642. https://doi.org/10/gjm2zn.

(14) Molčanov, K.; Milašinović, V.; Kojić-Prodić, B. Contribution of Different Crystal Packing Forces in π-Stacking: From Noncovalent to Covalent Multicentric Bonding. *Crystal Growth & Design* **2019**, *19* (10), 5967–5980. https://doi.org/10/gjpb7m.

(15) Koshihara, S.; Tokura, Y.; Iwasa, Y.; Koda, T. Inverse Peierls Transition Induced by Photoexcitation in Potassium Tetracyanoquinodimethane Crystals. *Phys. Rev. B* **1991**, *44* (1), 431–434. https://doi.org/10.1103/PhysRevB.44.431.

(16) Tomkiewicz, Y.; Andersen, J. R.; Taranko, A. R. Relative Stability of Donor and Acceptor Stacks against Peierls Distortion in the Tetrathia- and Tetraselenafulvalene-Tetracyanoquinodimethane Family of Organic Metals. *Phys. Rev. B* **1978**, *17* (4), 1579–1591. https://doi.org/10.1103/PhysRevB.17.1579.

(17) Zafra, J. L.; Qiu, L.; Yanai, N.; Mori, T.; Nakano, M.; Alvarez, M. P.; Navarrete, J. T. L.; Gómez-García, C. J.; Kertesz, M.; Takimiya, K.; Casado, J. Reversible Dimerization and Polymerization of a Janus Diradical To Produce Labile C−C Bonds and Large Chromic Effects. *Angewandte Chemie International Edition* **2016**, *55* (47), 14563–14568. https://doi.org/10.1002/anie.201605997.

(18) Mou, Z.; Kertesz, M. Pancake Bond Orders of a Series of π-Stacked Triangulene Radicals. *Angewandte Chemie (International ed. in English)* **2017**, *56* (34), 10188–10191. https://doi.org/10.1002/anie.201704941.

(19) Bogdanov, N. E.; Milašinović, V.; Zakharov, B. A.; Boldyreva, E. V.; Molčanov, K. Pancake-Bonding of Semi-quinone Radicals under Variable Temperature and Pressure Conditions. *Acta Cryst B* **2020**, *76* (2), 285–291. https://doi.org/10/gjpb6s.

(20) Takamuku, S.; Nakano, M. Theoretical Study on Second Hyperpolarizabilities of Intramolecular Pancake-Bonded Diradicaloids with Helical Scaffolds. *ACS Omega* **2019**, *4* (2), 2741–2749. https://doi.org/10/gjpb7j.

(21) Marcus, R. A. Electron Transfer Reactions in Chemistry. Theory and Experiment. *Rev. Mod. Phys.* **1993**, *65* (3), 599–610. https://doi.org/10.1103/RevModPhys.65.599.

(22) Malagoli, M.; Brédas, J. L. Density Functional Theory Study of the Geometric Structure and Energetics of Triphenylamine-Based Hole-Transporting Molecules. *Chemical Physics Letters* **2000**, *327* (1), 13–17. https://doi.org/10.1016/S0009-2614(00)00757-0.

(23) Chung, H.; Diao, Y. Polymorphism as an Emerging Design Strategy for High Performance Organic Electronics. *J. Mater. Chem. C* **2016**, *4* (18), 3915–3933. https://doi.org/10.1039/C5TC04390E.

(24) Brédas J. L.; Calbert J. P.; da Silva Filho D. A.; Cornil J. Organic Semiconductors: A Theoretical Characterization of the Basic Parameters Governing Charge Transport. *Proceedings of the National Academy of Sciences* **2002**, *99* (9), 5804–5809. https://doi.org/10.1073/pnas.092143399.

(25) Coropceanu, V.; Cornil, J.; da Silva Filho, D. A.; Olivier, Y.; Silbey, R.; Bredas, J.-L. Charge Transport in Organic Semiconductors. *Chemical Reviews* **2007**, *107* (4), 926–952. https://doi.org/10.1021/cr050140x.

(26) Stahly, G. P. Diversity in Single- and Multiple-Component Crystals. The Search for and Prevalence of Polymorphs and Cocrystals. *Crystal Growth & Design* **2007**, *7* (6), 1007–1026. https://doi.org/10.1021/cg060838j.

(27) Allen, F. H. The Cambridge Structural Database: A Quarter of a Million Crystal Structures and Rising. *Acta Cryst B* **2002**, *58* (3), 380–388. https://doi.org/10.1107/S0108768102003890.

(28) Brog, J.-P.; Chanez, C.-L.; Crochet, A.; Fromm, K. M. Polymorphism, What It Is and How to Identify It: A Systematic Review. *RSC Adv.* **2013**, *3* (38), 16905–16931. https://doi.org/10.1039/C3RA41559G.

(29) Bernstein, J.; Davey, R. J.; Henck, J.-O. Concomitant Polymorphs. *Angewandte Chemie International Edition* **1999**, *38* (23), 3440–3461. https://doi.org/10.1002/(SICI)1521-3773(19991203)38:23<3440::AID-ANIE3440>3.0.CO;2-#.

(30) Chung, S.-Y.; Kim, Y.-M.; Kim, J.-G.; Kim, Y.-J. Multiphase Transformation and Ostwald's Rule of Stages during Crystallization of a Metal Phosphate. *Nature Phys* **2009**, *5* (1), 68–73. https://doi.org/10/cpf7qc.

(31) Hedges, L. O.; Whitelam, S. Limit of Validity of Ostwalds Rule of Stages in a Statistical Mechanical Model of Crystallization. *Journal of Chemical Physics* **2011**, *135* (16). https://doi.org/10.1063/1.3655358.

(32) OSTWALD, W. Studies on the Formation and Change of Solid Matter. *Z. Phys. Chem.* **1897**, *22*, 289–302.

(33) Dunitz, J. D.; Bernstein, J. Disappearing Polymorphs. *Accounts of Chemical Research* **1995**, *28* (4), 193–200. https://doi.org/10.1021/ar00052a005.

(34) Bernstein, J. *Polymorphism in Molecular Crystals*; Oxford University Press: Oxford, 2007. https://doi.org/10.1093/acprof:oso/9780199236565.001.0001.

(35) Diao, Y.; Lenn, K. M.; Lee, W. Y.; Blood-Forsythe, M. A.; Xu, J.; Mao, Y.; Kim, Y.; Reinspach, J. A.; Park, S.; Aspuru-Guzik, A.; Xue, G.; Clancy, P.; Bao, Z.; Mannsfeld, S. C. B. Understanding Polymorphism in Organic Semiconductor Thin Films through Nanoconfinement. *Journal of the American Chemical Society* **2014**, *136* (49), 17046–17057. https://doi.org/10.1021/ja507179d.

(36) Jin, M.; Sumitani, T.; Sato, H.; Seki, T.; Ito, H. Mechanical-Stimulation-Triggered and Solvent-Vapor-Induced Reverse Single-Crystal-to-Single-Crystal Phase Transitions with Alterations of the Luminescence Color. *J. Am. Chem. Soc.* **2018**, *140* (8), 2875–2879. https://doi.org/10/gcz353.

(37) Ito, H.; Muromoto, M.; Kurenuma, S.; Ishizaka, S.; Kitamura, N.; Sato, H.; Seki, T. Mechanical Stimulation and Solid Seeding Trigger Single-Crystal-to-Single-Crystal Molecular Domino Transformations. *Nature Communications* **2013**, *4* (1), 2009. https://doi.org/10/gbdmt5.

(38) Neuhaus, J.; Petry, W.; Krimmel, A. Phonon Softening and Martensitic Transformation in α-Fe. *Physica B: Condensed Matter* **1997**, *234–236*, 897–899. https://doi.org/10.1016/S0921-4526(96)01185-4.

(39) Pérez-Reche, F. J.; Vives, E.; Mañosa, L.; Planes, A. Athermal Character of Structural Phase Transitions. *Physical Review Letters* **2001**, *87* (19), 195701. https://doi.org/10.1103/PhysRevLett.87.195701.

(40) Tuszynski, J. A.; Sept, D.; Molak, A.; Lehnen, P.; Dec, J.; Kleemann, W.; Parker, T. J.; Burfoot, J. C. Jerky Phase-Front Motion in PbTiO 3 Crystals Comments on Phase-Front Propagation in Ferroelectrics Athermal Martensitic Behaviour Enhanced in Sodium

Niobate by Mn Dopant and Axial Compression The Influence of Magnetic Fields on the Interphase Boundary Dyn. *J. Phys* **1988**, *21*, 1257–1263.

(41) Commins, P.; Desta, I. T.; Karothu, D. P.; Panda, M. K.; Naumov, P. Crystals on the Move: Mechanical Effects in Dynamic Solids. *Chem. Commun.* **2016**, *52* (97), 13941–13954. https://doi.org/10.1039/C6CC06235K.

(42) Panda, M. K.; Centore, R.; Causà, M.; Tuzi, A.; Borbone, F.; Naumov, P. Strong and Anomalous Thermal Expansion Precedes the Thermosalient Effect in Dynamic Molecular Crystals. *Sci Rep* **2016**, *6* (1), 29610. https://doi.org/10.1038/srep29610.

(43) Clapp, P. C. How Would We Recognize a Martensitic Transformation If It Bumped into Us on a Dark \& Austy Night? *Journal De Physique Iv* **1995**, *5* (C8, Part 1), 11–19. https://doi.org/10.1051/jp4:1995802.

(44) Khalil, A.; Ahmed, E.; Naumov, P. Metal-Coated Thermosalient Crystals as Electrical Fuses. *Chemical Communications* **2017**, *53* (60), 8470–8473. https://doi.org/10.1039/C7CC04251E.

(45) Panda, M. K.; Runčevski, T.; Chandra Sahoo, S.; Belik, A. A.; Nath, N. K.; Dinnebier, R. E.; Naumov, P. Colossal Positive and Negative Thermal Expansion and Thermosalient Effect in a Pentamorphic Organometallic Martensite. *Nature Communications* **2014**, *5* (1), 4811–4811. https://doi.org/10.1038/ncomms5811.

(46) Gomez-Cortes, J. F.; No, M. L.; Lopez-Ferreno, I.; Hernandez-Saz, J.; Molina, S. I.; Chuvilin, A.; San Juan, J. M. Size Effect and Scaling Power-Law for Superelasticity in Shape-Memory Alloys at the Nanoscale. *Nat Nanotechnol* **2017**, No. May, 1–8. https://doi.org/10.1038/nnano.2017.91.

(47) Patriarca, L.; Abuzaid, W.; Carlucci, G.; Belelli, F.; Casati, R. Pseudoelasticity in FeMnNiAl Shape Memory Alloy Lattice Structures Produced by Laser Powder Bed Fusion. *Materials Letters* **2021**, *302*, 130349. https://doi.org/10.1016/j.matlet.2021.130349.

(48) Takamizawa, S.; Takasaki, Y. Shape-Memory Effect in an Organosuperelastic Crystal. *Chem. Sci.* **2016**, *7* (2), 1527–1534. https://doi.org/10/gjm2s3.

(49) Sasaki, T.; Sakamoto, S.; Engel, E. R.; Takamizawa, S. An Organosuperelastic Mechanism with Bending Molecular Chain Bundles. *Crystal Growth & Design* **2021**, *21* (5), 2920–2924. https://doi.org/10/gjv32r.

(50) Engel, E. R.; Takamizawa, S. Versatile Ferroelastic Deformability in an Organic Single Crystal by Twinning about a Molecular Zone Axis. *Angew. Chem.* **2018**, *130* (37), 12064–12068. https://doi.org/10/gjm2sp.

(51) Seki, T.; Feng, C.; Kashiyama, K.; Sakamoto, S.; Takasaki, Y.; Sasaki, T.; Takamizawa, S.; Ito, H. Photoluminescent Ferroelastic Molecular Crystals. *Angew. Chem. Int. Ed.* **2020**, *59* (23), 8839–8843. https://doi.org/10/gjm2rp.

(52) Park, S. K.; Sun, H.; Chung, H.; Patel, B. B.; Zhang, F.; Davies, D. W.; Woods, T. J.; Zhao, K.; Diao, Y. Super- and Ferroelastic Organic Semiconductors for Ultraflexible Single-Crystal Electronics. *Angewandte Chemie International Edition* **2020**, *59* (31), 13004–13012. https://doi.org/10.1002/anie.202004083.

(53) Chung, H.; Dudenko, D.; Zhang, F.; D'Avino, G.; Ruzié, C.; Richard, A.; Schweicher, G.; Cornil, J.; Beljonne, D.; Geerts, Y.; Diao, Y. Rotator Side Chains Trigger Cooperative Transition for Shape and Function Memory Effect in Organic Semiconductors. *Nature Communications* **2018**, *9* (1), 278. https://doi.org/10.1038/s41467-017-02607-9.

(54) Narayan, A.; Campos, L. A.; Bhatia, S.; Fushman, D.; Naganathan, A. N. Graded Structural Polymorphism in a Bacterial Thermosensor Protein. *Journal of the American Chemical Society* **2017**, *139* (2), 792–802. https://doi.org/10.1021/jacs.6b10608.

(55) Chung, H.; Chen, S.; Patel, B.; Garbay, G.; Geerts, Y. H.; Diao, Y. Understanding the Role of Bulky Side Chains on Polymorphism of BTBT-Based Organic Semiconductors. *Crystal Growth & Design* **2020**, *20* (3), 1646–1654. https://doi.org/10.1021/acs.cgd.9b01372.

(56) Chung, H.; Chen, S.; Sengar, N.; Davies, D. W.; Garbay, G.; Geerts, Y. H.; Clancy, P.; Diao, Y. Single Atom Substitution Alters the Polymorphic Transition Mechanism in Organic Electronic Crystals. *Chemistry of Materials* **2019**, *31* (21), 9115–9126. https://doi.org/10.1021/acs.chemmater.9b03436.

(57) Shalev, O.; Raghavan, S.; Mazzara, J. M.; Senabulya, N.; Sinko, P. D.; Fleck, E.; Rockwell, C.; Simopoulos, N.; Jones, C. M.; Schwendeman, A.; Mehta, G.; Clarke, R.; Amidon, G. E.; Shtein, M. Printing of Small Molecular Medicines from the Vapor Phase. *Nature Communications* **2017**, *8* (1), 711. https://doi.org/10.1038/s41467-017-00763-6.

(58) Smirnov, M. B.; Kazimirov, V. Yu.; Baddour-Hadjean, R.; Smirnov, K. S.; Pereira-Ramos, J.-P. Atomistic Mechanism of α–β Phase Transition in Vanadium Pentoxide. *Journal of Physics and Chemistry of Solids* **2014**, *75* (1), 115–122. https://doi.org/10.1016/j.jpcs.2013.09.007.

(59) Hörter, D.; Dressman, J. B. Influence of Physicochemical Properties on Dissolution of Drugs in the Gastrointestinal Tract. *Advanced Drug Delivery Reviews* **2001**, *46* (1–3), 75–87. https://doi.org/10.1016/S0169-409X(00)00130-7.

(60) Bernstein, J.; Davey, R. J.; Henck, J.-O. Concomitant Polymorphs. *Angewandte Chemie International Edition* **1999**, *38* (23), 3440–3461. https://doi.org/10.1002/(SICI)1521-3773(19991203)38:23<3440::AID-ANIE3440>3.0.CO;2-#.

(61) Yu, L.; Niazi, M. R.; Ngongang Ndjawa, G. O.; Li, R.; Kirmani, A. R.; Munir, R.; Balawi, A. H.; Laquai, F.; Amassian, A. Programmable and Coherent Crystallization of Semiconductors. *Science Advances* **2017**, *3* (3), e1602462. https://doi.org/10.1126/sciadv.1602462.

(62) Yu, L. Polymorphism in Molecular Solids: An Extraordinary System of Red, Orange, and Yellow Crystals. *Accounts of Chemical Research* **2010**, *43* (9), 1257–1266. https://doi.org/10.1021/ar100040r.

(63) Galindo, S.; Tamayo, A.; Leonardi, F.; Mas-Torrent, M. Control of Polymorphism and Morphology in Solution Sheared Organic Field-Effect Transistors. *Advanced Functional Materials* **2017**, *1700526*, 1–9. https://doi.org/10.1002/adfm.201700526.

(64) Zhao, Y.; Guo, Y.; Liu, Y. 25th Anniversary Article: Recent Advances in n-Type and Ambipolar Organic Field-Effect Transistors. *Advanced Materials* **2013**, *25* (38), 5372–5391. https://doi.org/10.1002/adma.201302315.

(65) Suzuki, Y.; Miyazaki, E.; Takimiya, K. ((Alkyloxy)Carbonyl)Cyanomethylene-Substituted Thienoquinoidal Compounds: A New Class of Soluble n-Channel Organic Semiconductors for Air-Stable Organic Field-Effect Transistors. *Journal of the American Chemical Society* **2010**, *132* (30), 10453–10466. https://doi.org/10.1021/ja103171y.

(66) Kang, K.; Watanabe, S.; Broch, K.; Sepe, A.; Brown, A.; Nasrallah, I.; Nikolka, M.; Fei, Z.; Heeney, M.; Matsumoto, D.; Marumoto, K.; Tanaka, H.; Kuroda, S.; Sirringhaus, H. 2D Coherent Charge Transport in Highly Ordered Conducting Polymers Doped by Solid

State Diffusion. *Nature Materials* **2016**, *15* (8), 896–902. https://doi.org/10.1038/nmat4634.

(67) Chernyshov, I. Y.; Vener, M. V.; Feldman, E. V.; Paraschuk, D. Y.; Sosorev, A. Y. Inhibiting Low-Frequency Vibrations Explains Exceptionally High Electron Mobility in 2,5-Difluoro-7,7,8,8-Tetracyanoquinodimethane (F2-TCNQ) Single Crystals. *Journal of Physical Chemistry Letters* **2017**, *8* (13), 2875–2880. https://doi.org/10.1021/acs.jpclett.7b01003.

(68) Casado, J.; Ponce Ortiz, R.; López Navarrete, J. T. Quinoidal Oligothiophenes: New Properties behind an Unconventional Electronic Structure. *Chemical Society Reviews* **2012**, *41* (17), 5672–5686. https://doi.org/10.1039/C2CS35079C.

(69) Zhang, C.; Zang, Y.; Zhang, F.; Diao, Y.; McNeill, C. R.; Di, C.; Zhu, X.; Zhu, D. Pursuing High-Mobility n-Type Organic Semiconductors by Combination of “Molecule-Framework” and “Side-Chain” Engineering. *Advanced Materials* **2016**, *28* (38), 8456–8462. https://doi.org/10.1002/adma.201602598.

(70) Zhang, C.; Zang, Y.; Gann, E.; McNeill, C. R.; Zhu, X.; Di, C.; Zhu, D. Two-Dimensional π-Expanded Quinoidal Terthiophenes Terminated with Dicyanomethylenes as n-Type Semiconductors for High-Performance Organic Thin-Film Transistors. *Journal of the American Chemical Society* **2014**, *136* (46), 16176–16184. https://doi.org/10.1021/ja510003y.

(71) Casado, J.; López Navarrete, J. T. The Longest Quinoidal Oligothiophene: A Raman Story. *The Chemical Record* **2011**, *11* (1), 45–53. https://doi.org/10.1002/tcr.201000022.

(72) Ponce Ortiz, R.; Casado, J.; Rodríguez González, S.; Hernández, V.; López Navarrete, J. T.; Viruela, P. M.; Ortí, E.; Takimiya, K.; Otsubo, T. Quinoidal Oligothiophenes: Towards Biradical Ground-State Species. *Chemistry – A European Journal* **2010**, *16* (2), 470–484. https://doi.org/10.1002/chem.200902037.

(73) Ribierre, J.-C.; Watanabe, S.; Matsumoto, M.; Muto, T.; Nakao, A.; Aoyama, T. Reversible Conversion of the Majority Carrier Type in Solution-Processed Ambipolar Quinoidal Oligothiophene Thin Films. *Advanced Materials* **2010**, *22* (36), 4044–4048. https://doi.org/10.1002/adma.201001170.

(74) Ribierre, J. C.; Fujihara, T.; Watanabe, S.; Matsumoto, M.; Muto, T.; Nakao, A.; Aoyama, T. Direct Laser Writing of Complementary Logic Gates and Lateral P-n Diodes in a Solution-Processible Monolithic Organic Semiconductor. *Advanced Materials* **2010**, *22* (15), 1722–1726. https://doi.org/10.1002/adma.200903152.

(75) Yuan, D.; Huang, D.; Rivero, S. M.; Zhu, D.; Casanova, D.; Yuan, D.; Huang, D.; Rivero, S. M.; Carreras, A.; Zhang, C. Cholesteric Aggregation at the Quinoidal-to- Diradical Border Enabled Stable n -Doped Conductor. *CHEM* **2019**, *5* (4), 964–976. https://doi.org/10.1016/j.chempr.2019.02.010.

(76) Casado, J.; Ponce Ortiz, R.; López Navarrete, J. T. Quinoidal Oligothiophenes: New Properties behind an Unconventional Electronic Structure. *Chemical Society Reviews* **2012**, *41* (17), 5672–5686. https://doi.org/10.1039/c2cs35079c.

(77) Yang, K.; Zhang, X.; Harbuzaru, A.; Wang, L.; Wang, Y.; Koh, C.; Guo, H.; Shi, Y.; Chen, J.; Sun, H.; Feng, K.; Ruiz Delgado, M. C.; Woo, H. Y.; Ortiz, R. P.; Guo, X. Stable Organic Diradicals Based on Fused Quinoidal Oligothiophene Imides with High Electrical Conductivity. *Journal of the American Chemical Society* **2020**, *142* (9), 4329–4340. https://doi.org/10.1021/jacs.9b12683.

(78) Averkiev, B.; Isaac, R.; Jucov, E. V; Khrustalev, V. N.; Kloc, C.; McNeil, L. E.; Timofeeva, T. V. Evidence of Low-Temperature Phase Transition in Tetracene–Tetracyanoquinodimethane Complex. *Crystal Growth & Design* **2018**, *18* (7), 4095–4102. https://doi.org/10.1021/acs.cgd.8b00501.

(79) Curtis, F.; Wang, X.; Marom, N. Effect of Packing Motifs on the Energy Ranking and Electronic Properties of Putative Crystal Structures of Tricyano-1,4-Dithiino[c]-Isothiazole. *Acta Crystallographica Section B: Structural Science, Crystal Engineering and Materials* **2016**, *72* (4), 562–570. https://doi.org/10.1107/S2052520616009227.

(80) Yuan, D.; Huang, D.; Zhang, C.; Zou, Y.; Di, C. A.; Zhu, X.; Zhu, D. Efficient Solution-Processed n-Type Small-Molecule Thermoelectric Materials Achieved by Precisely Regulating Energy Level of Organic Dopants. *ACS Applied Materials and Interfaces* **2017**, *9* (34), 28795–28801. https://doi.org/10.1021/acsami.7b07282.

(81) Mannsfeld, S. C. B.; Virkar, A.; Reese, C.; Toney, M. F.; Bao, Z. Precise Structure of Pentacene Monolayers on Amorphous Silicon Oxide and Relation to Charge Transport. *Advanced Materials* **2009**, *21* (22), 2294–2298. https://doi.org/10.1002/adma.200803328.

(82) Jiang, Z. {\it GIXSGUI}: A MATLAB Toolbox for Grazing-Incidence X-Ray Scattering Data Visualization and Reduction, and Indexing of Buried Three-Dimensional Periodic Nanostructured Films. *Journal of Applied Crystallography* **2015**, *48* (3), 917–926. https://doi.org/10.1107/S1600576715004434.

(83) Yuan, D.; Guo, Y.; Zeng, Y.; Fan, Q.; Wang, J.; Yi, Y.; Zhu, X. Air-Stable n-Type Thermoelectric Materials Enabled by Organic Diradicaloids. *Angewandte Chemie International Edition* **2019**, *58* (15), 4958–4962. https://doi.org/10.1002/anie.201814544.

(84) Bruker. APEX3. Bruker AXS, Inc.: Madison, Wisconsin, USA 2018.

(85) Krause, L.; Herbst-Irmer, R.; Sheldrick, G. M.; Stalke, D. Comparison of Silver and Molybdenum Microfocus X-Ray Sources for Single-Crystal Structure Determination. *Journal of Applied Crystallography* **2015**, *48* (1), 3–10. https://doi.org/10.1107/S1600576714022985.

(86) Sheldrick, G. M. SHELXT - Integrated Space-Group and Crystal-Structure Determination. *Acta Crystallographica Section A* **2015**, *71* (1), 3–8. https://doi.org/10.1107/S2053273314026370.

(87) Sheldrick, G. M. Crystal Structure Refinement with SHELXL. *Acta Crystallographica Section C* **2015**, *71* (1), 3–8. https://doi.org/10.1107/S2053229614024218.

(88) Macrae, C. F.; Sovago, I.; Cottrell, S. J.; Galek, P. T. A.; McCabe, P.; Pidcock, E.; Platings, M.; Shields, G. P.; Stevens, J. S.; Towler, M.; Wood, P. A. Mercury 4.0: From Visualization to Analysis, Design and Prediction. *Journal of Applied Crystallography* **2020**, *53* (1), 226–235. https://doi.org/10.1107/S1600576719014092.

(89) Jiang, Z.; Li, X.; Strzalka, J.; Sprung, M.; Sun, T.; Sandy, A. R.; Narayanan, S.; Lee, D. R.; Wang, J. The Dedicated High-Resolution Grazing-Incidence X-Ray Scattering Beamline 8-ID-E at the Advanced Photon Source. *Journal of Synchrotron Radiation* **2012**, *19* (4), 627–636.

(90) Momma, K.; Izumi, F. VESTA3 for Three-Dimensional Visualization of Crystal, Volumetric and Morphology Data. *Journal of Applied Crystallography* **2011**, *44* (6), 1272–1276. https://doi.org/10.1107/S0021889811038970.

(91) Anderson, P. W. More Is Different. *Science* **1972**, *177* (4047), 393–396. https://doi.org/10/c7tv4m.

(92) Whitty, A. Cooperativity and Biological Complexity. *Nature chemical biology* **2008**, *4* (8), 435–439. https://doi.org/10.1038/nchembio0808-435.

(93) van den Ende, J. a.; Ensing, B.; Cuppen, H. M. Energy Barriers and Mechanisms in Solid–Solid Polymorphic Transitions Exhibiting Cooperative Motion. *CrystEngComm* **2016**, *18* (23), 4420–4430. https://doi.org/10.1039/C5CE02550H.

(94) Pérez-Reche, F. J.; Vives, E.; Mañosa, L.; Planes, A. Athermal Character of Structural Phase Transitions. *Physical Review Letters* **2001**, *87* (19), 195701–195701. https://doi.org/10.1103/PhysRevLett.87.195701.

(95) Vesely, S. L.; Dolci, S. R.; Vesely, A. A.; Dolci, C. A. Cooperativity as an Emergent Phenomenon. In *2019 IEEE Radio and Antenna Days of the Indian Ocean (RADIO)*; 2019; pp 1–2.

(96) Karothu, D. P.; Weston, J.; Desta, I. T.; Naumov, P. Shape-Memory and Self-Healing Effects in Mechanosalient Molecular Crystals. *J. Am. Chem. Soc.* **2016**, *138* (40), 13298–13306. https://doi.org/10/gmfdbc.

(97) Mañosa, L.; Planes, A.; Rouby, D.; Morin, M.; Fleischmann, P.; Macqueron, J. L. Acoustic Emission Field during Thermoelastic Martensitic Transformations. *Applied Physics Letters* **1989**, *54* (25), 2574–2576. https://doi.org/10.1063/1.101053.

(98) Yang, K.; Zhang, X.; Harbuzaru, A.; Wang, L.; Wang, Y.; Koh, C.; Guo, H.; Shi, Y.; Chen, J.; Sun, H.; Feng, K.; Ruiz Delgado, M. C.; Woo, H. Y.; Ortiz, R. P.; Guo, X. Stable Organic Diradicals Based on Fused Quinoidal Oligothiophene Imides with High Electrical Conductivity. *Journal of the American Chemical Society* **2020**, *142* (9), 4329–4340. https://doi.org/10.1021/jacs.9b12683.

(99) Bi, D.; Henkes, S.; Daniels, K. E.; Chakraborty, B. The Statistical Physics of Athermal Materials. *Annu. Rev. Condens. Matter Phys* **2015**, *6*, 63–83. https://doi.org/10.1146/annurev-conmatphys-031214-014336.

(100) Chung, H.; Dudenko, D.; Zhang, F.; D’Avino, G.; Ruzié, C.; Richard, A.; Schweicher, G.; Cornil, J.; Beljonne, D.; Geerts, Y.; Diao, Y. Rotator Side Chains Trigger Cooperative Transition for Shape and Function Memory Effect in Organic Semiconductors. *Nature Communications* **2018**, *9* (1), 278–278. https://doi.org/10.1038/s41467-017-02607-9.

(101) Chung, H.; Chen, S.; Patel, B.; Garbay, G.; Geerts, Y. H.; Diao, Y. Understanding the Role of Bulky Side Chains on Polymorphism of BTBT-Based Organic Semiconductors. *Crystal Growth & Design* **2020**, *20* (3), 1646–1654. https://doi.org/10.1021/acs.cgd.9b01372.

(102) Diao, Y.; Lenn, K. M.; Lee, W. Y.; Blood-Forsythe, M. A.; Xu, J.; Mao, Y.; Kim, Y.; Reinspach, J. A.; Park, S.; Aspuru-Guzik, A.; Xue, G.; Clancy, P.; Bao, Z.; Mannsfeld, S. C. B. Understanding Polymorphism in Organic Semiconductor Thin Films through Nanoconfinement. *Journal of the American Chemical Society* **2014**, *136* (49), 17046–17057. https://doi.org/10.1021/ja507179d.

(103) Chung, H.; Chen, S.; Sengar, N.; Davies, D. W.; Garbay, G.; Geerts, Y. H.; Clancy, P.; Diao, Y. Single Atom Substitution Alters the Polymorphic Transition Mechanism in Organic Electronic Crystals. *Chemistry of Materials* **2019**, *31* (21), 9115–9126. https://doi.org/10.1021/acs.chemmater.9b03436.

(104) Panzer, F.; Bässler, H.; Köhler, A. Temperature Induced Order-Disorder Transition in Solutions of Conjugated Polymers Probed by Optical Spectroscopy. *Journal of Physical Chemistry Letters* **2017**, *8* (1), 114–125. https://doi.org/10.1021/acs.jpclett.6b01641.

(105) Su, S.-Q.; Kamachi, T.; Yao, Z.-S.; Huang, Y.-G.; Shiota, Y.; Yoshizawa, K.; Azuma, N.; Miyazaki, Y.; Nakano, M.; Maruta, G.; Takeda, S.; Kang, S.; Kanegawa, S.; Sato, O. Assembling an Alkyl Rotor to Access Abrupt and Reversible Crystalline Deformation of a Cobalt(II) Complex. *Nature Communications* **2015**, *6* (1), 8810–8810. https://doi.org/10.1038/ncomms9810.

(106) Sato, O. Dynamic Molecular Crystals with Switchable Physical Properties. *Nature Chemistry* **2016**, *8* (7), 644–656. https://doi.org/10.1038/nchem.2547.

(107) Dharmarwardana, M.; Pakhira, S.; Welch, R. P.; Caicedo-Narvaez, C.; Luzuriaga, M. A.; Arimilli, B. S.; McCandless, G. T.; Fahimi, B.; Mendoza-Cortes, J. L.; Gassensmith, J. J. Rapidly Reversible Organic Crystalline Switch for Conversion of Heat into Mechanical Energy. *J. Am. Chem. Soc.* **2021**, *143* (15), 5951–5957. https://doi.org/10.1021/jacs.1c01549.

(108) Zhang, C.; Zang, Y.; Zhang, F.; Diao, Y.; McNeill, C. R.; Di, C.; Zhu, X.; Zhu, D. Pursuing High-Mobility n-Type Organic Semiconductors by Combination of “Molecule-Framework” and “Side-Chain” Engineering. *Advanced Materials* **2016**, *28* (38), 8456–8462. https://doi.org/10.1002/adma.201602598.

(109) Zhao, Y.; Guo, Y.; Liu, Y. 25th Anniversary Article: Recent Advances in n-Type and Ambipolar Organic Field-Effect Transistors. *Advanced Materials* **2013**, *25* (38), 5372–5391. https://doi.org/10.1002/adma.201302315.

(110) Suzuki, Y.; Miyazaki, E.; Takimiya, K. ((Alkyloxy)Carbonyl)Cyanomethylene-Substituted Thienoquinoidal Compounds: A New Class of Soluble n-Channel Organic Semiconductors for Air-Stable Organic Field-Effect Transistors. *Journal of the American Chemical Society* **2010**, *132* (30), 10453–10466. https://doi.org/10.1021/ja103171y.

(111) Yuan, D.; Huang, D.; Rivero, S. M.; Carreras, A.; Zhang, C.; Zou, Y.; Jiao, X.; McNeill, C. R.; Zhu, X.; Di, C.; Zhu, D.; Casanova, D.; Casado, J. Cholesteric Aggregation at the Quinoidal-to-Diradical Border Enabled Stable n-Doped Conductor. *Chem* **2019**, *5* (4), 964–976. https://doi.org/10.1016/j.chempr.2019.02.010.

(112) Yuan, D.; Guo, Y.; Zeng, Y.; Fan, Q.; Wang, J.; Yi, Y.; Zhu, X. Air-Stable n-Type Thermoelectric Materials Enabled by Organic Diradicaloids. *Angewandte Chemie International Edition* **2019**, *58* (15), 4958–4962. https://doi.org/10.1002/anie.201814544.

(113) Ortiz, R. P.; Casado, J.; Gonzµlez, R.; Hernµndez, V.; Navarrete, T. L.; Viruela, P. M.; Ortí, E.; Takimiya, K.; Otsubo, T. Quinoidal Oligothiophenes: Towards Biradical Ground-State Species. *Chemistry – A European Journal* **2010**, *16* (2), 470–484. https://doi.org/10.1002/chem.200902037.

(114) Shimizu, A.; Uruichi, M.; Yakushi, K.; Matsuzaki, H.; Okamoto, H.; Nakano, M.; Hirao, Y.; Matsumoto, K.; Kurata, H.; Kubo, T. Resonance Balance Shift in Stacks of Delocalized Singlet Biradicals. *Angewandte Chemie International Edition* **2009**, *48* (30), 5482–5486. https://doi.org/10.1002/anie.200901382.

(115) Kubo, T.; Shimizu, A.; Uruichi, M.; Yakushi, K.; Nakano, M.; Shiomi, D.; Sato, K.; Takui, T.; Morita, Y.; Nakasuji, K. Singlet Biradical Character of Phenalenyl-Based Kekulé

Hydrocarbon with Naphthoquinoid Structure. *Organic Letters* **2006**, *9* (1), 81–84. https://doi.org/10.1021/ol062604z.

(116) Zhang, Y.; Zheng, Y.; Zhou, H.; Miao, M.-S.; Wudl, F.; Nguyen, T.-Q. Temperature Tunable Self-Doping in Stable Diradicaloid Thin-Film Devices. *Advanced Materials* **2015**, *27* (45), 7412–7419. https://doi.org/10.1002/adma.201502404.

(117) Davies, D. W.; Park, S. K.; Kafle, P.; Chung, H.; Yuan, D.; Strzalka, J. W.; Mannsfeld, S. C. B.; Wang, S. G.; Chen, Y.-S.; Gray, D. L.; Zhu, X.; Diao, Y. Radically Tunable N-Type Organic Semiconductor via Polymorph Control. *Chemistry of Materials* **2021**, *33* (7), 2466–2477. https://doi.org/10.1021/acs.chemmater.0c04678.

(118) Chung, H.; Ruzié, C.; Geerts, Y.; Diao, Y. Hybrid Mechanism of Nucleation and Cooperative Propagation in a Single-Crystal-to-Single-Crystal Transition of a Molecular Crystal. *Crystal Growth & Design* **2018**, *18* (8), 4245–4251. https://doi.org/10.1021/acs.cgd.8b00452.

(119) Planes, A.; Mañosa, L.; Vives, E. Acoustic Emission in Martensitic Transformations. *Journal of Alloys and Compounds* **2013**, *577*, S699–S704. https://doi.org/10/fnqdrw.

(120) Park, S. K.; Diao, Y. Martensitic Transition in Molecular Crystals for Dynamic Functional Materials. *Chem. Soc. Rev.* **2020**, *49* (22), 8287–8314. https://doi.org/10.1039/D0CS00638F.

(121) Fleury, P. A. Phase Transitions, Critical Phenomena, and Instabilities. *Science* **1981**, *211* (4478), 125–131. https://doi.org/10.1126/science.211.4478.125.

(122) Cook, H. E.; Suezawa, M.; Kajitani, T.; Rivaud, L. Pretransition Phenomena. *J. Phys. Colloques* **1977**, *38* (C7), C7-439. https://doi.org/10.1051/jphyscol:1977786.

(123) Tandon, P.; Förster, G.; Neubert, R.; Wartewig, S. Phase Transitions in Oleic Acid as Studied by X-Ray Diffraction and FT-Raman Spectroscopy. *Journal of Molecular Structure* **2000**, *524* (1), 201–215. https://doi.org/10.1016/S0022-2860(00)00378-1.

(124) Wood, S.; Rigas, G.-P.; Zoladek-Lemanczyk, A.; Blakesley, J. C.; Georgakopoulos, S.; Mas-Torrent, M.; Shkunov, M.; Castro, F. A. Precise Characterisation of Molecular Orientation in a Single Crystal Field-Effect Transistor Using Polarised Raman Spectroscopy. *Sci Rep* **2016**, *6* (1), 33057. https://doi.org/10/gjm2r9.

(125) Pan, M.; Liu, J.; Zhong, H.; Wang, S.; Li, Z.; Chen, X.; Lu, W. Raman Study of the Phase Transition in VO2 Thin Films. *Journal of Crystal Growth* **2004**, *268* (1), 178–183. https://doi.org/10.1016/j.jcrysgro.2004.05.005.

(126) Mintairov, A. M.; Merz, J. L.; Vlasov, A. S.; Vinokurov, D. V. Observation of a Martensitic Transition in the Raman Spectra of Spontaneously Ordered GaInP Alloys. *Semicond. Sci. Technol.* **1998**, *13* (10), 1140–1147. https://doi.org/10.1088/0268-1242/13/10/015.

(127) Casado, J.; Ponce Ortiz, R.; López Navarrete, J. T. Quinoidal Oligothiophenes: New Properties behind an Unconventional Electronic Structure. *Chemical Society Reviews* **2012**, *41* (17), 5672–5686. https://doi.org/10.1039/C2CS35079C.

(128) Castiglioni, C.; Lopez Navarrete, J. T.; Zerbi, G.; Gussoni, M. A Simple Interpretation of the Vibrational Spectra of Undoped, Doped and Photoexcited Polyacetylene: Amplitude Mode Theory in the GF Formalism. *Solid State Communications* **1988**, *65* (7), 625–630. https://doi.org/10.1016/0038-1098(88)90352-3.

(129) Ferrari, A. C.; Robertson, J.; Castiglioni, C.; Tommasini, M.; Zerbi, G. Raman Spectroscopy of Polyconjugated Molecules and Materials: Confinement Effect in One and Two Dimensions. *Philosophical Transactions of the Royal Society of London. Series A:*

Mathematical, Physical and Engineering Sciences **2004**, *362* (1824), 2425–2459. https://doi.org/10.1098/rsta.2004.1448.

(130) Venkataraman, N. V.; Bhagyalakshmi, S.; Vasudevan, S.; Seshadri, R. Conformation and Orientation of Alkyl Chains in the Layered Organic–Inorganic Hybrids: (CnH2n+1NH3)2PbI4 (n = 12,16,18). *Physical Chemistry Chemical Physics* **2002**, *4* (18), 4533–4538. https://doi.org/10.1039/B204983J.

(131) G. Brown, K.; Bicknell-Brown, Ellen.; Ladjadj, Meriem. Raman-Active Bands Sensitive to Motion and Conformation at the Chain Termini and Backbones of Alkanes and Lipids. *The Journal of Physical Chemistry* **2002**, *91* (12), 3436–3442. https://doi.org/10.1021/j100296a066.

(132) J. Orendorff, C.; W. Ducey, M.; E. Pemberton, J. Quantitative Correlation of Raman Spectral Indicators in Determining Conformational Order in Alkyl Chains. *The Journal of Physical Chemistry A* **2002**, *106* (30), 6991–6998. https://doi.org/10.1021/jp014311n.

(133) Luz-Lima, C.; Borges, J. A.; Moura, J. V. B.; Pinheiro, G. S.; Viana, B. C.; Mendes-Filho, J.; Freire, P. T. C. α-l-Glutamic Acid under High Pressure: Phase Transitions Studied by Raman Spectroscopy. *Vibrational Spectroscopy* **2016**, *86*, 343–349. https://doi.org/10.1016/j.vibspec.2016.08.012.

(134) Pelikan, P.; Ceppan, M.; Liska, M. *Applications of Numerical Methods in Molecular Spectroscopy*; CRC Press: Boca Raton, 1993; p Chap. 1.

(135) Schweizer, K. S.; Chandler, D. Vibrational Dephasing and Frequency Shifts of Polyatomic Molecules in Solution. *J. Chem. Phys.* **1982**, *76* (5), 2296–2314. https://doi.org/10.1063/1.443302.

(136) Bradley, M. S.; Krech, J. H. High-Pressure Raman Spectra of the Acetone Carbonyl Stretch in Acetone-Methanol Mixtures. *J. Phys. Chem.* **1993**, *97* (3), 575–580. https://doi.org/10.1021/j100105a009.

(137) Filatov, S. K. General Concept of Increasing Crystal Symmetry with an Increase in Temperature. *Crystallography Reports* **2011**, *56* (6), 953–961. https://doi.org/10.1134/S1063774511060083.

(138) Casado, J.; Ortiz, R. P.; Navarrete, J. T. L. Quinoidal Oligothiophenes: New Properties behind an Unconventional Electronic Structure. *Chem. Soc. Rev.* **2012**, *41* (17), 5672–5686. https://doi.org/10/gj7kkw.

(139) Kotula, A. P.; Walker, A. R. H.; Migler, K. B. Raman Analysis of Bond Conformations in the Rotator State and Premelting of Normal Alkanes. *Soft Matter* **2016**, *12* (22), 5002–5010. https://doi.org/10.1039/C6SM00182C.

(140) Jin, Y.; Kotula, A. P.; Walker, A. R. H.; Migler, K. B.; Lee, Y. J. Phase-Specific Raman Analysis of n-Alkane Melting by Moving-Window Two-Dimensional Correlation Spectroscopy. *Journal of Raman Spectroscopy* **2016**, *47* (11), 1375–1384. https://doi.org/10.1002/jrs.4967.

(141) Smets, M. M. H.; Kalkman, E.; Krieger, A.; Tinnemans, P.; Meekes, H.; Vlieg, E.; Cuppen, H. M. On the Mechanism of Solid-State Phase Transitions in Molecular Crystals – the Role of Cooperative Motion in (Quasi)Racemic Linear Amino Acids. *IUCrJ* **2020**, *7* (2), 331–341. https://doi.org/10.1107/S2052252520001335.

(142) Smets, M. M. H.; Brugman, S. J. T.; van Eck, E. R. H.; van den Ende, J. A.; Meekes, H.; Cuppen, H. M. Understanding the Solid-State Phase Transitions of Dl-Norleucine: An in

Situ DSC, Microscopy, and Solid-State NMR Study. *Crystal Growth & Design* **2015**, *15* (10), 5157–5167. https://doi.org/10.1021/acs.cgd.5b01188.

(143) Brown, J. T.; Zeller, M.; Rosokha, S. V. Effects of Structural Variations on π-Dimer Formation: Long-Distance Multicenter Bonding of Cation-Radicals of Tetrathiafulvalene Analogues. *Phys. Chem. Chem. Phys.* **2020**, *22* (43), 25054–25065. https://doi.org/10/ghp8gh.

(144) Wehrmann, C. M.; Charlton, R. T.; Chen, M. S. A Concise Synthetic Strategy for Accessing Ambient Stable Bisphenalenyls toward Achieving Electroactive Open-Shell π-Conjugated Materials. *J. Am. Chem. Soc.* **2019**, *141* (7), 3240–3248. https://doi.org/10/gjpb7n.

(145) Jiang, Z.; Li, X.; Strzalka, J.; Sprung, M.; Sun, T.; Sandy, A. R.; Narayanan, S.; Lee, D. R.; Wang, J. The Dedicated High-Resolution Grazing-Incidence X-Ray Scattering Beamline 8-ID-E at the Advanced Photon Source. *Journal of Synchrotron Radiation* **2012**, *19* (4), 627–636.

(146) Jiang, Z. GIXSGUI: A MATLAB Toolbox for Grazing-Incidence X-Ray Scattering Data Visualization and Reduction, and Indexing of Buried Three-Dimensional Periodic Nanostructured Films. *Journal of Applied Crystallography* **2015**, *48* (3), 917–926. https://doi.org/10.1107/S1600576715004434.

(147) McCrone, W. C. *Physics and Chemistry of the Organic Solid State*; Wiley-Interscience: New York, 1965; Vol. 2, pp 725–767.

(148) Groom, C. R.; Bruno, I. J.; Lightfoot, M. P.; Ward, S. C. The Cambridge Structural Database. *Acta Cryst B* **2016**, *72* (2), 171–179. https://doi.org/10.1107/S2052520616003954.

(149) Kafle, P.; Sanghavi, R.; Khasbaatar, A.; Punjani, S.; Davies, D. W.; Diao, Y. Drastic Modulation of Molecular Packing and Intrinsic Dissolution Rates by Meniscus-Guided Coating of Extremely Confined Pharmaceutical Thin Films. *ACS Appl. Mater. Interfaces* **2021**, *13* (47), 56519–56529. https://doi.org/10.1021/acsami.1c08398.

(150) Chung, H.; Diao, Y. Polymorphism as an Emerging Design Strategy for High Performance Organic Electronics. *J. Mater. Chem. C* **2016**, *4* (18), 3915–3933. https://doi.org/10.1039/C5TC04390E.

(151) Khalil, A.; Karothu, D. P.; Naumov, P. Direct Quantification of Rapid and Efficient Single-Stroke Actuation by a Martensitic Transition in a Thermosalient Crystal. *J. Am. Chem. Soc.* **2019**, *141* (8), 3371–3375. https://doi.org/10/gjm2ss.

(152) Shi, Y.; Gerkman, M. A.; Qiu, Q.; Zhang, S.; Han, G. G. D. Sunlight-Activated Phase Change Materials for Controlled Heat Storage and Triggered Release. *J. Mater. Chem. A* **2021**, *9* (15), 9798–9808. https://doi.org/10.1039/D1TA01007G.

(153) Kahr, B.; Freudenthal, J.; Gunn, E. Crystals in Light. *Accounts of Chemical Research* **2010**, *43* (5), 684–692. https://doi.org/10.1021/ar900288m.

(154) Wight, C. D.; Xiao, Q.; Wagner, H. R.; Hernandez, E. A.; Lynch, V. M.; Iverson, B. L. Mechanistic Analysis of Solid-State Colorimetric Switching: Monoalkoxynaphthalene-Naphthalimide Donor–Acceptor Dyads. *J. Am. Chem. Soc.* **2020**, *142* (41), 17630–17643. https://doi.org/10/gjp95d.

(155) Su, Y.; Bhunia, S.; Xu, S.; Chen, A.; Reddy, C. M.; Cai, T. Structure–Thermomechanical Property Correlation in Polymorphic Molecular Crystals Probed by the Nanoindentation

Technique. *Chem. Mater.* **2021**, *33* (12), 4821–4829. https://doi.org/10.1021/acs.chemmater.1c00584.

(156) Peng, Y.; Wang, F.; Wang, Z.; Alsayed, A. M.; Zhang, Z.; Yodh, A. G.; Han, Y. Two-Step Nucleation Mechanism in Solid-Solid Phase Transitions. *Nature materials* **2014**, *14* (January), 1–16. https://doi.org/10.1038/nmat4083.

(157) Vekilov, P. G. Nucleation. *Crystal Growth and Design* **2010**, *10* (12), 5007–5019. https://doi.org/10.1021/cg1011633.

(158) Zahn, D.; Anwar, J. Collective Displacements in a Molecular Crystal Polymorphic Transformation. *RSC Advances* **2013**, *3* (31), 12810–12815. https://doi.org/10.1039/C3RA40653A.

(159) Smets, M. M. H.; Kalkman, E.; Krieger, A.; Tinnemans, P.; Meekes, H.; Vlieg, E.; Cuppen, H. M. On the Mechanism of Solid-State Phase Transitions in Molecular Crystals – the Role of Cooperative Motion in (Quasi)Racemic Linear Amino Acids. *IUCrJ* **2020**, *7* (2), 331–341. https://doi.org/10.1107/S2052252520001335.

(160) Davies, D. W.; Park, S. K.; Shiring, S. B.; Chung, H.; Kafle, P.; Yuan, D.; Strzalka, J. W.; Weber, R.; Zhu, X.; Savoie, B. M.; Diao, Y. A Tale of Two Transitions: Unraveling Two Distinct Polymorph Transition Mechanisms in One n-Type Single Crystal for Dynamic Electronics. *ChemRxiv* **2021**. https://doi.org/10.26434/chemrxiv-2021-9xghl.

(161) Casado, J.; López Navarrete, J. T. The Longest Quinoidal Oligothiophene: A Raman Story. *The Chemical Record* **2011**, *11* (1), 45–53. https://doi.org/10.1002/tcr.201000022.

(162) Burrezo, P. M.; Zafra, J. L.; López Navarrete, J. T.; Casado, J. Quinoidal/Aromatic Transformations in π-Conjugated Oligomers: Vibrational Raman Studies on the Limits of Rupture for π-Bonds. *Angewandte Chemie International Edition* **2017**, *56* (9), 2250–2259. https://doi.org/10.1002/anie.201605893.

(163) Quintero, S. M.; Zafra, J. L.; Yamamoto, K.; Aso, Y.; Ie, Y.; Casado, J. Oligoene and Cyanine Features of Tetracyano Quinoidal Oligothiophenes. *J. Mater. Chem. C* **2021**, *9* (33), 10727–10740. https://doi.org/10.1039/D1TC01436F.

(164) Hu, X.; Chen, H.; Xue, G.; Zheng, Y. Correlation between the Strength of Conjugation and Spin–Spin Interactions in Stable Diradicaloids. *J. Mater. Chem. C* **2020**, *8* (31), 10749–10754. https://doi.org/10/gjm2rm.

(165) Han, H.; Zhang, D.; Zhu, Z.; Wei, R.; Xiao, X.; Wang, X.; Liu, Y.; Ma, Y.; Zhao, D. Aromatic Stacking Mediated Spin–Spin Coupling in Cyclophane-Assembled Diradicals. *J. Am. Chem. Soc.* **2021**. https://doi.org/10.1021/jacs.1c08262.

(166) Christensen, D. V.; Dittmann, R.; Linares-Barranco, B.; Sebastian, A.; Le Gallo, M.; Redaelli, A.; Slesazeck, S.; Mikolajick, T.; Spiga, S.; Menzel, S.; Valov, I.; Milano, G.; Ricciardi, C.; Liang, S.-J.; Miao, F.; Lanza, M.; Quill, T. J.; Keene, S. T.; Salleo, A.; Grollier, J.; Markovic, D.; Mizrahi, A.; Yao, P.; Yang, J. J.; Indiveri, G.; Strachan, J. P.; Datta, S.; Vianello, E.; Valentian, A.; Feldmann, J.; Li, X.; Pernice, W. H.; Bhaskaran, H.; Furber, S.; Neftci, E.; Scherr, F.; Maass, W.; Ramaswamy, S.; Tapson, J.; Panda, P.; Kim, Y.; Tanaka, G.; Thorpe, S.; Bartolozzi, C.; Cleland, T. A.; Posch, C.; Liu, S.-C.; Panuccio, G.; Mahmud, M.; Mazumder, A. N.; Hosseini, M.; Mohsenin, T.; Donati, E.; Tolu, S.; Galeazzi, R.; Christensen, M. E.; Holm, S.; Ielmini, D.; Pryds, N. 2022 Roadmap on Neuromorphic Computing and Engineering. *Neuromorph. Comput. Eng.* **2022**. https://doi.org/10.1088/2634-4386/ac4a83.

(167) Nawrocki, R. A.; Voyles, R. M.; Shaheen, S. E. A Mini Review of Neuromorphic Architectures and Implementations. *IEEE Trans. Electron Devices* **2016**, *63* (10), 3819–3829. https://doi.org/10/ghsmdj.

(168) van de Burgt, Y.; Melianas, A.; Keene, S. T.; Malliaras, G.; Salleo, A. Organic Electronics for Neuromorphic Computing. *Nat Electron* **2018**, *1* (7), 386–397. https://doi.org/10/gf7hjn.

(169) Wang, Z.; Joshi, S.; Savel'ev, S. E.; Jiang, H.; Midya, R.; Lin, P.; Hu, M.; Ge, N.; Strachan, J. P.; Li, Z.; Wu, Q.; Barnell, M.; Li, G.-L.; Xin, H. L.; Williams, R. S.; Xia, Q.; Yang, J. J. Memristors with Diffusive Dynamics as Synaptic Emulators for Neuromorphic Computing. *Nature Materials* **2017**, *16* (1), 101–108. https://doi.org/10/gcx46c.

(170) Denisyuk, A. I.; MacDonald, K. F.; Abajo, F. J. G. de; Zheludev, N. I. Towards Femtojoule Nanoparticle Phase-Change Memory. *Jpn. J. Appl. Phys.* **2009**, *48* (3S1), 03A065. https://doi.org/10.1143/JJAP.48.03A065.

(171) Gallo, M. L.; Sebastian, A. An Overview of Phase-Change Memory Device Physics. *J. Phys. D: Appl. Phys.* **2020**, *53* (21), 213002. https://doi.org/10.1088/1361-6463/ab7794.

(172) Pirovano, A. An Introduction on Phase-Change Memories. In *Phase Change Memory: Device Physics, Reliability and Applications*; Redaelli, A., Ed.; Springer International Publishing: Cham, 2018; pp 1–10. https://doi.org/10.1007/978-3-319-69053-7_1.

(173) Park, H.-L.; Kim, M.-H.; Kim, H.; Lee, S.-H. Self-Selective Organic Memristor by Engineered Conductive Nanofilament Diffusion for Realization of Practical Neuromorphic System. *Advanced Electronic Materials* **2021**, *7* (8), 2100299. https://doi.org/10.1002/aelm.202100299.

(174) van de Burgt, Y.; Lubberman, E.; Fuller, E. J.; Keene, S. T.; Faria, G. C.; Agarwal, S.; Marinella, M. J.; Alec Talin, A.; Salleo, A. A Non-Volatile Organic Electrochemical Device as a Low-Voltage Artificial Synapse for Neuromorphic Computing. *Nature Materials* **2017**, *16* (4), 414–418. https://doi.org/10/f9rtm7.

(175) Ribierre, B. J.; Watanabe, S.; Matsumoto, M.; Muto, T.; Nakao, A.; Aoyama, T.; Ribierre, J.-C.; Watanabe, S.; Matsumoto, M.; Muto, T.; Nakao, A.; Aoyama, T. Reversible Conversion of the Majority Carrier Type in Solution-Processed Ambipolar Quinoidal Oligothiophene Thin Films. *Advanced Materials* **2010**, *22* (36), 4044–4048. https://doi.org/10.1002/adma.201001170.

(176) Patel, B. B.; Chang, Y.; Park, S. K.; Wang, S.; Rosheck, J.; Patel, K.; Walsh, D.; Guironnet, D.; Diao, Y. PolyChemPrint: A Hardware and Software Framework for Benchtop Additive Manufacturing of Functional Polymeric Materials. *Journal of Polymer Science* **2021**, *59* (21), 2468–2478. https://doi.org/10.1002/pol.20210086.

(177) Nishiuchi, T.; Ito, R.; Stratmann, E.; Kubo, T. Switchable Conformational Isomerization of an Overcrowded Tristricyclic Aromatic Ene. *J. Org. Chem.* **2020**, *85* (1), 179–186. https://doi.org/10.1021/acs.joc.9b02432.

(178) Tanaka, K.; Toda, F. A Novel Photochromism of Biindenylidene in Crystal Form. *J. Chem. Soc., Perkin Trans. 1* **2000**, No. 6, 873–874. https://doi.org/10.1039/A910194M.

(179) Günther, K.; Grabicki, N.; Battistella, B.; Grubert, L.; Dumele, O. An All-Organic Photochemical Magnetic Switch with Bistable Spin States. **2022**. https://doi.org/10.26434/chemrxiv-2022-bh283.

(180) Zhang, C.; Medina Rivero, S.; Liu, W.; Casanova, D.; Zhu, X.; Casado, J. Stable Cross-Conjugated Tetrathiophene Diradical. *Angewandte Chemie International Edition* **2019**, *58* (33), 11291–11295. https://doi.org/10.1002/anie.201904153.

(181) Casado, J.; Hernández, V.; Navarrete, J. T. L. Vibrational Raman Shifts and Aromaticity: The Case of Oligothiophenes. *The Chemical Record* **2015**, *15* (6), 1110–1118. https://doi.org/10.1002/tcr.201500025.

(182) Sjöqvist, J.; C. González-Cano, R.; Navarrete, J. T. L.; Casado, J.; Delgado, M. C. R.; Linares, M.; Norman, P. A Combined MD/QM and Experimental Exploration of Conformational Richness in Branched Oligothiophenes. *Physical Chemistry Chemical Physics* **2014**, *16* (45), 24841–24852. https://doi.org/10.1039/C4CP03365E.

APPENDIX A: SUPPLEMENTARY MATERIALS FOR CHAPTER 2

A.1 Structure Refinement

A structural model consisting of the host with 4 disordered alkane chains was developed. Each 6 C chain at C3 and C16 was modeled as disordered over 2 orientations Like C-C bonds and C-C-C bond angles were restrained to be similar (esd 0.02 and 0.06 Å respectively). Both the R and S configuration at the C29 position are possible. The C8\C10 chains were thus modeled as both the R and S configuration, however, free rotation about the C28-C29 bond is also possible so the 10C chain could sometime occupy the position of the 8C chain. Both the R and S configuration of the R Group were modeled, but the free rotation was not. All like C-C bonds and C-C-C bond angles were restrained to be similar (esd 0.02 and 0.06 Å respectively). Rigid bond restraints were imposed on all the atoms in this structure because of the poor resolution, data collection temperature and large amount of disorder. All disordered atoms that overlap by less than van der Waals radii were restrained to have similar displacement parameters (esd 0.01 for core atoms and 0.02 for terminal atoms). All disordered chains were left as isotropic positions because of the extreme disorder in these locations.

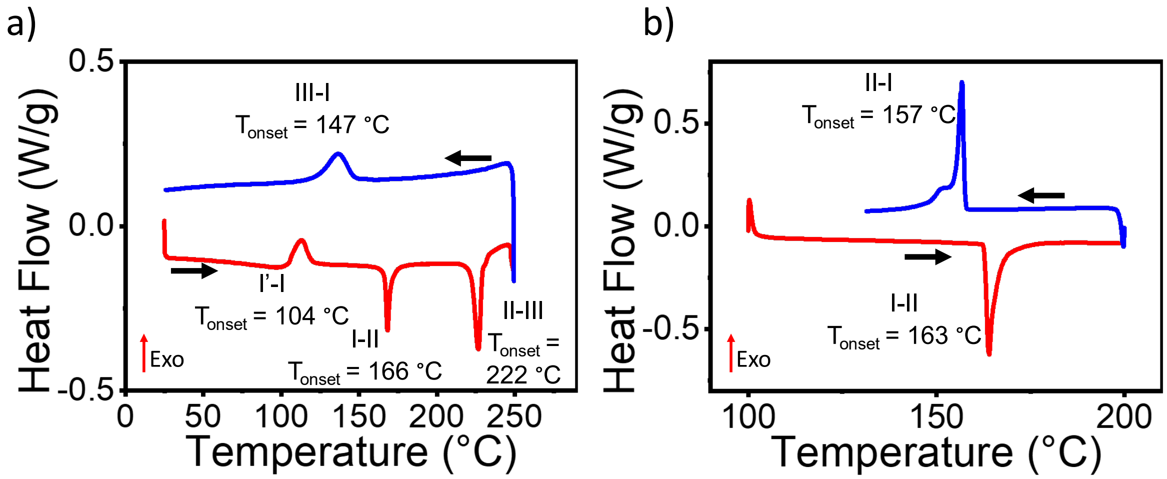

Figure A1. DSC for II-III transitions (a) and I-II transition (b) and low temperature showing no transition (c). For the II-III transition (a), the temperature ramp was set to 5 °C/min. For the I-II transition (b) the temperature ramp was set to 10 °C/min

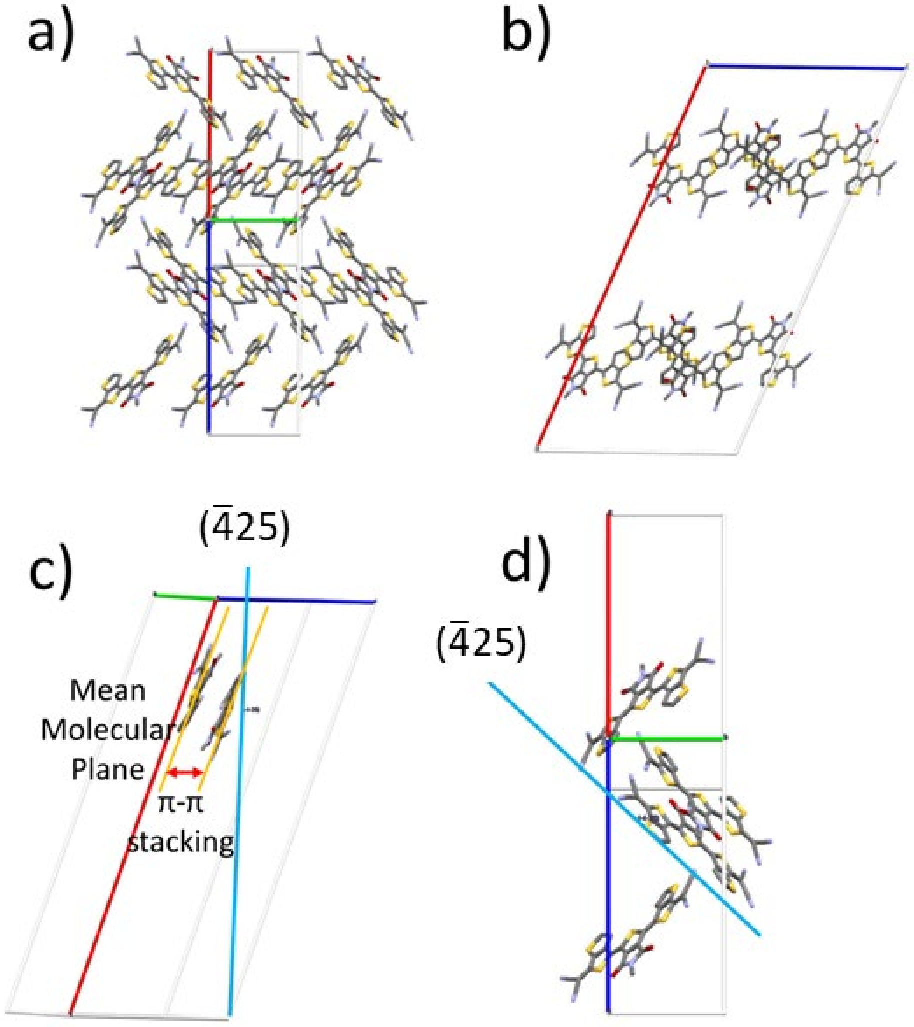

Figure A2. Packing of 2DQTT-o-B at room temperature looking at the bc-plane (a) and ac-plane (b). The unit cell is drawn such that the a, b and c directions are indicated by the colors red, green, and blue respectively. (c) The π-π stacking distance is indicated by the spacing between the molecules perpendicular to the (-425) plane, representing the π-π stacking plane. (d) The π-π stacking plane looking at the bc plane, showing the (-425) plane parallels the long axis of the molecule. The measured distance of the π-π stacking distance was measured to be 3.59 Å.

Table A1. Complete list of conditions under which each polymorph was obtained directly through printing

Polymorph I'

Printing				spincoating			
	Chloroform	DCM	Toluene		chloroform	DCM	Toluene
Substrate	SiO2/PTS	SiO2/PTS	SiO2/PTS	Substrate	SiO2/PTS	SiO2/PTS	SiO2/PTS
Solution and Substrate Temperature (°C)	25	25	80	Solution Temperature (°C)	25	25	100
Concentration (mg mL^{-1})	6	6	6	Concentration (mg mL^{-1})	6	6	6
Speed (mm s^{-1})	0.1-50	0.1-0.5	0.1-0.5	Speed (rpm)	1000-3000	1000-3000	1000-3000
Gap Height (µm)	100	100	100				

Polymorph I''

Printing	
	Chlorobenzene
Substrate	SiO2/PTS
Solution and Substrate Temperature (°C)	85
Concentration (mg mL^{-1})	6
Speed (mm s^{-1})	0.1-0.5
Gap Height (µm)	100

Table A2. Summary of I’ devices with a direction parallel and perpendicular to the printing direction

Parallel

Device	μ (cm^2 V^{-1} s^{-1})	V_{th} (V)	I_{on}/I_{off}	Device	μ (cm^2 V^{-1} s^{-1})	V_{th} (V)	I_{on}/I_{off}
11_A1a_t	2.14E-05	-278.89	1.73	5_A1a_t	5.10E-04	10.44	48.63
11_A1c_t	7.40E-05	-214.49	1.39	5_A1b_t	1.29E-03	14.87	70.88
11_A2a_t	1.10E-04	-98.90	1.87	5_A2a_t	4.10E-04	6.17	12.41
11_A2c_t	3.56E-05	-185.68	1.55	5_A3a_t	3.29E-04	5.01	17.24
11_A3a_t	1.50E-04	-34.79	2.79	5_A3b_t	2.68E-04	7.46	51.33
11_A3b_t	2.07E-05	-214.06	1.62	5_A3c_t	5.42E-04	14.76	31.53
11_A3c_t	5.85E-05	-109.04	1.68	5_A4a_t	3.69E-04	5.96	61.89
11_A4a_t	1.17E-04	-24.42	3.12	5_A4b_t	4.41E-04	15.01	26.36
11_A4b_t	1.22E-04	-7.03	5.34	5_A4c_t	5.09E-04	17.92	24.00
11_A5a_t	1.52E-04	-16.56	3.47	5_A5a_t	3.89E-04	3.74	27.17
11_A5b_t	1.95E-05	-80.43	2.50	5_A5b_t	3.90E-04	10.78	51.46
11_A5c_t	1.97E-04	19.10	7.73	5_A5c_t	4.62E-04	9.10	48.83
11_A6a_t	1.64E-04	7.11	16.64	5_A6a_t	4.45E-04	10.56	61.45
11_A6c_t	2.16E-04	15.57	11.92	5_A6b_t	5.63E-05	-34.74	3.43
2_B1a_t	1.40E-04	-23.80	3.30	5_A6c_t	1.78E-04	29.40	10.46
2_B1b_t	6.61E-05	-259.81	1.30	5_A7c_t	3.97E-04	9.44	279.04
2_B1c_t	2.10E-05	-787.84	1.14	6_A1a_t	3.36E-04	-27.64	3.48
2_B2a_t	1.59E-05	-151.46	1.60	6_A1c_t	3.77E-04	-9.06	5.20
2_B2b_t	2.02E-05	-434.46	1.16	6_A2a_t	1.66E-03	-15.93	41.67
2_B2c_t	1.29E-05	1200.45	1.08	6_A3a_t	2.36E-04	-43.97	2.45
2_B3a_t	1.64E-04	-5.39	4.98	6_A4a_t	1.14E-04	-23.22	31.96
2_B3b_t	1.52E-05	-500.49	1.16	6_A4c_t	8.38E-05	-164.53	1.59
2_B4b_t	1.27E-05	-479.55	1.22	6_A5a_t	3.15E-04	-49.08	2.85
2_B4c_t	1.46E-05	-1018.18	1.09	6_A6a_t	2.72E-04	-57.78	2.39
2_B5a_t	7.03E-05	-67.42	2.09	6_A7a_t	2.89E-04	-19.00	4.25
2_B5b_t	4.79E-06	-807.69	1.17	6_A7c_t	1.33E-04	-125.59	1.61
2_B5c_t	6.47E-06	-1284.80	1.09	8_B1a_t	4.15E-04	12.09	27.53
2_B6a_t	1.42E-04	-43.51	2.32	8_B1b_t	2.43E-04	12.72	10.85
2_B6b_t	2.88E-06	-796.56	1.21	8_B2a_t	3.74E-04	12.95	19.95
2_B6c_t	2.16E-05	-757.72	1.10	8_B2b_t'	3.13E-04	19.01	11.88
2_B7a_t	1.07E-04	-68.50	1.92	8_B3a_t	3.32E-04	12.88	20.11
2_B7b_t	2.36E-05	-449.92	1.17	8_B3b_t	2.59E-04	13.13	13.07
2_C1b_t	2.49E-04	1.73	95.73	8_B4a_t	3.38E-04	12.33	16.85
2_C1c_t	1.40E-04	-29.41	3.16	8_B4b_t	2.89E-04	24.78	8.84
2_C2b_t	3.54E-04	9.04	376.09	8_B5b_t	2.88E-04	13.76	17.54
2_C2c_t	1.65E-04	-41.45	2.61	8_B6a_t	3.88E-04	15.14	16.01
2_C3b_t	4.82E-05	-59.10	2.20	8_B6b_t	3.41E-04	15.26	19.59
2_C3c_t	1.54E-04	-39.23	2.66	8_B7b_t	2.96E-04	12.31	18.00
2_C4c_t	1.53E-04	-54.92	2.11				
Average	2.17E-04	-146.33	21.21				
Standard Deviation	2.26E-04	293.86	55.02				

Table A.2 (Cont.)

	Perpendicular		
Device	μ ($cm^2 V^{-1} s^{-1}$)	V_{th} (V)	I_{on}/I_{off}
2_D1a_t	1.63E-04	-40.29	2.46
2_D1b_t	1.01E-04	-71.75	1.97
2_D1c_t	5.26E-05	-142.42	1.55
2_D1d_t	6.01E-05	-194.72	1.38
2_D1e_t	3.25E-05	-337.91	1.24
2_D1f_t	1.17E-05	-1620.24	1.07
2_D2a_t	2.58E-04	-41.53	2.69
2_D2b_t	8.64E-05	-177.08	1.44
2_D2c_t	6.59E-05	-157.11	1.50
2_D2d_t	4.59E-05	-274.98	1.28
5_C1b_t	2.49E-04	-4.17	15.65
5_C1c_t	4.23E-04	6.95	44.01
5_C1d_t	3.65E-04	-9.33	5.07
5_C1e_t	5.10E-04	9.99	102.62
5_C1f_t	6.24E-04	1.91	24.75
6_B1a_t	4.08E-04	-21.69	3.15
Average	2.16E-04	-192.15	13.24
Standard Deviation	1.95E-04	395.62	26.57

μ_{par}/μ_{perp}	1.00

Table A3. Summary of I′′ devices separated into channel directions parallel and perpendicular to the printing direction.

Parallel

Device	μ ($cm^2 V^{-1} s^{-1}$)	V_{th} (V)	I_{on}/I_{off}
051619-2_A2b_t	2.03E-03	-5.63	8.80E+00
051619-2_A3b_t	3.10E-03	5.36	5.80E+00
051619-2_A3c_t	3.33E-03	-1.41	9.73E+00
051619-2_A4b_t	3.12E-03	2.87	7.11E+00
051619-2_A4c_t	3.17E-03	-0.75	6.90E+00
051619-2_A5a_t	5.92E-04	-30.25	4.13E+00
051619-2_A5c_t	3.82E-03	-3.12	6.41E+00
051619-2_A6c_t	2.91E-03	-1.52	6.93E+00
051619-2_A7a_t	9.95E-04	1.35	1.07E+01
051619-3_B2a_t	1.32E-03	-14.46	1.12E+01
051619-3_B3a_t	4.26E-04	11.27	3.87E+01
051619-3_B4a_t	1.63E-03	11.32	2.16E+01
051619-3_B6a_t	1.16E-03	13.69	5.41E+01
051619-3_B7a_t	8.36E-04	-5.43	2.11E+01
051619-6_A2c_t	1.16E-04	13.03	-1.20E+02
Average	1.90E-03	-0.25	6.24E+00
Standard Deviation	1.23E-03	11.50	3.75E+01

Perpendicular

Device	μ ($cm^2 V^{-1} s^{-1}$)	V_{th} (V)	I_{on}/I_{off}
051619-2_B2c_t	1.97E-03	-15.27	3.98E+00
051619-2_B2e_t	2.33E-03	-17.23	6.11E+00
051619-2_B3a_t	7.50E-04	-23.38	4.67E+00
051619-2_B3b_t	8.31E-04	-22.05	6.61E+00
051619-3_A1e_t	5.99E-04	-29.88	3.32E+00
051619-3_A1g_t	7.63E-04	-14.56	6.10E+00
051619-3_A3e_t	7.91E-04	-34.30	3.18E+00
051619-3_A3f_t	7.74E-04	-3.03	5.15E+00
051619-3_A3g_t	4.56E-04	-14.77	3.96E+00
051619-6_B1a_t	1.93E-04	10.09	-5.69E+02
Average	9.46E-04	-16.44	-5.26E+01
Standard Deviation	6.36E-04	12.13	1.72E+02

μ_{par}/μ_{perp}	2.01

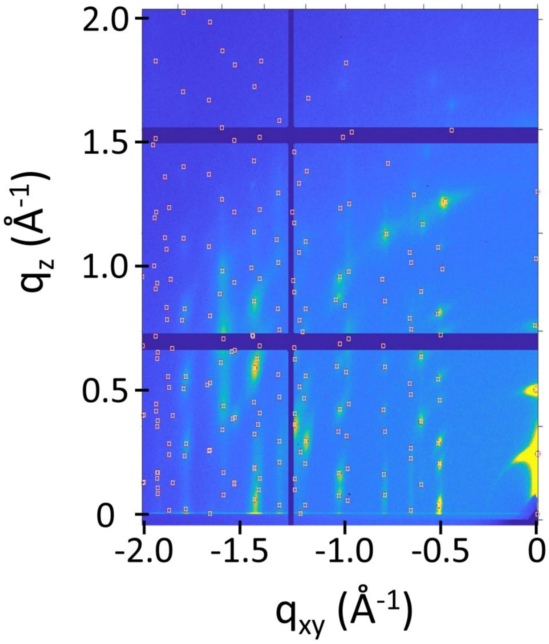

Figure A3. Simulated diffraction peaks from SCXRD and overlaid with GIXD pattern of polymorph I at 25 °C.

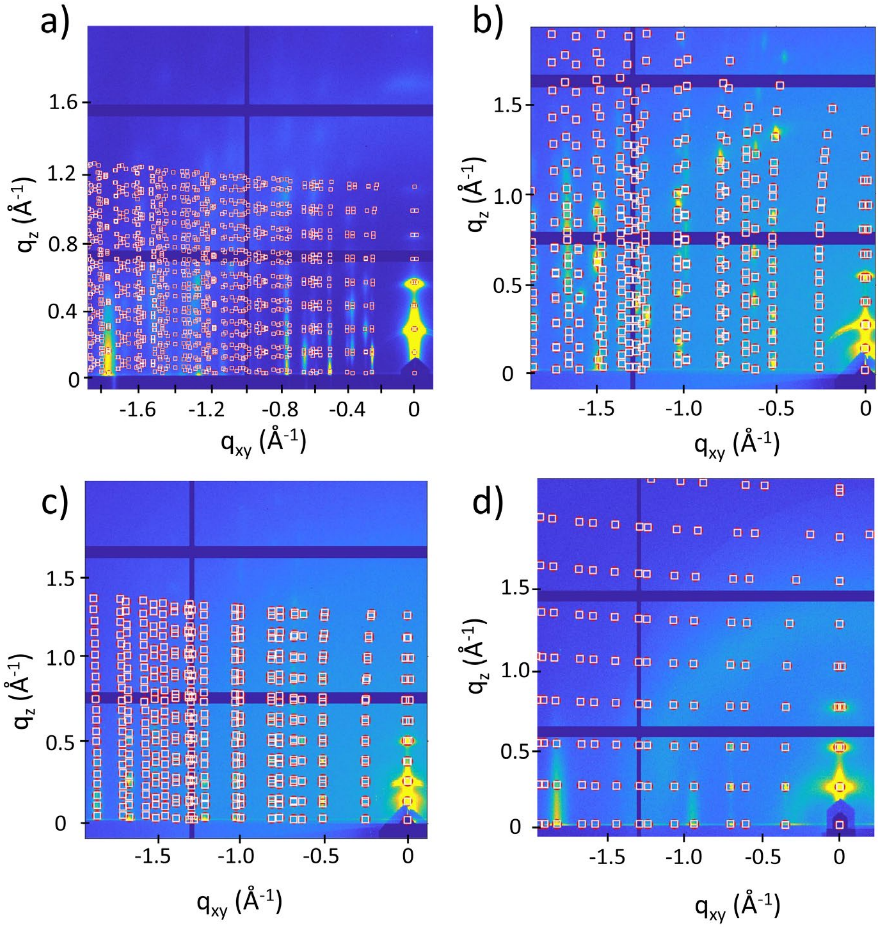

Figure A4. Simulated diffraction patterns for polymorphs I'' (a), I (b), II (c), III (d). Polymorphs I'' and I were simulated at room temperature. Polymorphs II and III were simulated at 200 °C and 220 °C respectively. For polymorphs I'', I and II, we obtained unit cells from fitting the calculated peak positions $\{\mathbf{q}_{\mathbf{xy}}^{\mathbf{calc}},\ q_z^{calc}\} = \{k\mathbf{b}_{\parallel}^{*} + l\mathbf{c}_{\parallel}^{*}, h|\mathbf{a}^{*}| +\ kb_{\perp}^{*} +\ lc_{\perp}^{*}\}$ to the experimentally obtained peak positions. Here, the subscript ∥ denotes the 2D in-plane reciprocal unit cell vectors (x,y-components), and ⊥ the respective out-of-plane components. The best fit unit cells are obtained by looking for reciprocal basis vectors $\mathbf{a}^{*}, \mathbf{b}^{*}, \mathbf{c}^{*}$ for which the least square error $\sum_{peaks}\left(\left|\mathbf{q}_{\mathbf{xy}}^{\mathbf{calc}} - \mathbf{q}_{\mathbf{xy}}^{\mathbf{exp}}\right| + \left|q_z^{calc} - q_z^{exp}\right|\right)^2$ is minimal. These cells were then simulated with considering the b-c plane parallel to the substrate using GIXSGUI. A complete list of parameters for simulation is listed in **Table S4**.We noticed 2 angles (α and γ) were very close to 90°, and upon setting the unit cell to a monoclinic system, we obtained very good agreement between each simulated peak position from GIXSGUI and the experimental diffraction. It is important to note, since we could not obtain enough peaks to determine the space group and account for systematic absences, we simulated each unit cell with a P1 symmetry, to account for all of the potential peaks. In polymorph I'', this becomes an issue due to the alignment discussed in **Figure C2(c,d)**. We simulated the peaks on the parallel diffraction pattern; however it is likely some of the rods are not visible, or may be extremely weak due to the high degree of alignment in the film. We also notice that for polymorphs I and II, all the 01 rods are predicted but do not appear in the experimental data, suggesting a glide plane. But given the few number of absent rods, we cannot be completely certain. For polymorph III, a fitted unit cell was not possible due to the low number of peaks. However, the unit cell appeared to potentially be tetragonal, since b and c appeared to be equal, and all angles 90°. We were able to estimate what the lengths should be based on peak assignment of the tetragonal unit cell. Simulations based on this unit cell were able to

Figure A4 (cont.)

account for both the rectangular pattern in the peaks, the overlap of the a and b axes and the extra vertical peak at q_r =0.95 Å^{-1}. Even with a P1 symmetry, not considering systematic absences, we predicted no peaks to be close to q_r =0.95 Å^{-1}. So, we instead tried a hexagonal unit cell, used the peak positions to estimate the cell lengths, and found very nice agreement between the simulated and experimental results. Consistent with this unit cell, we noticed that the over predicted rods in this case were 11, 22 etc, suggesting a possible systematic absence.

Table A4. Simulation parameters for each polymorph diffraction pattern in **Figure A4.**

		Cell Orientation (uvw)			Simulated (hkl) Ranges		
Polymorph	Simulated symmetry	u	v	w	h	k	l
I''	P1	1	1.19E-02	6.82E-02	-8:8	-6:6	-6:6
I	P1	1	-3.27E-04	8.36E-01	-10:10	-6:6	-6:6
II	P1	1	-2.47E-04	4.77E-02	-10:10	-6:6	-6:6
III	P1	1	5.00E-01	0	-8:8	-6:6	-6:6

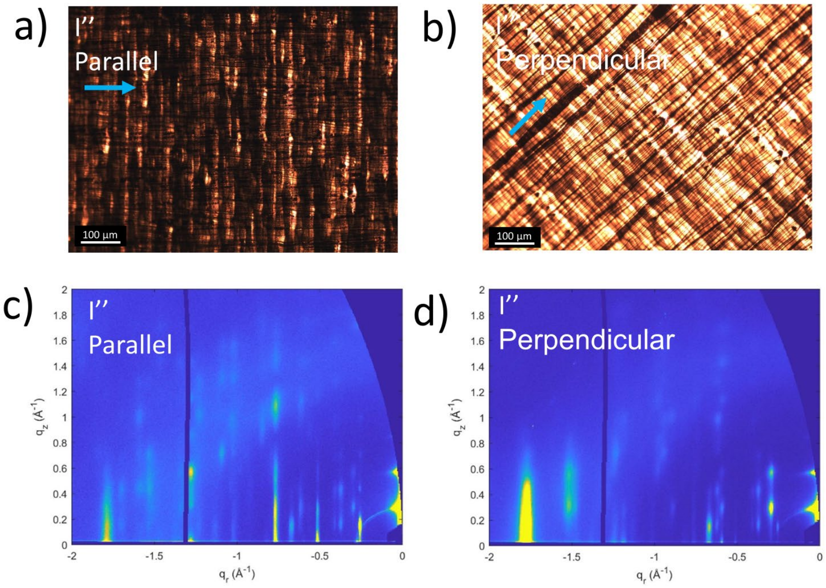

Figure A5. Printed thin films of I'' (0.2 mm s^{-1}, 85 °C) at 0° and 45°, (a,b) showing significant birefringence due to alignment of the molecule in the film. The printing direction is along the direction of the arrow. Parallel and perpendicular diffraction patterns showing the absence of the 01 rods in the perpendicular direction (c,d).

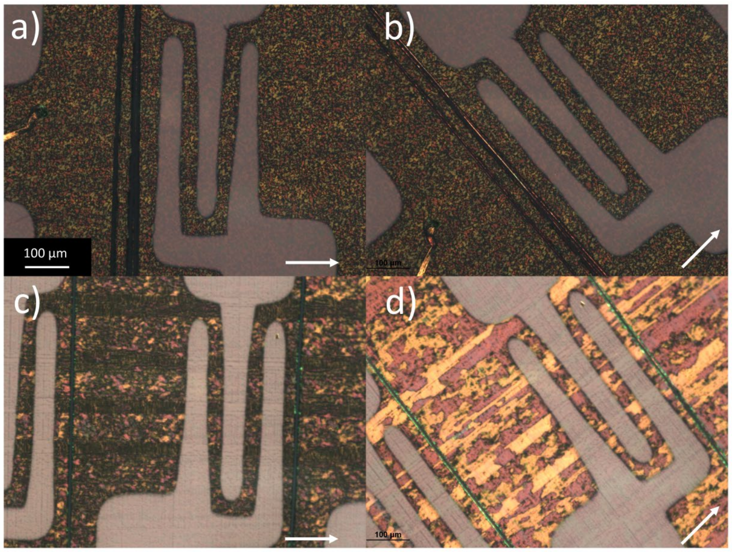

Figure A6. Film of polymorph I annealed from polymorph I’ (printed from chloroform) at 0° and 45° (a, b respectively) showing no birefringence under POM. Film of polymorph I annealed from polymorph I’’ (printed from chlorobenzene) at 0° and 45° (c, d respectively) showing significant birefringence as a result of the originally aligned polymorph I’’. White arrows indicate direction of printing.

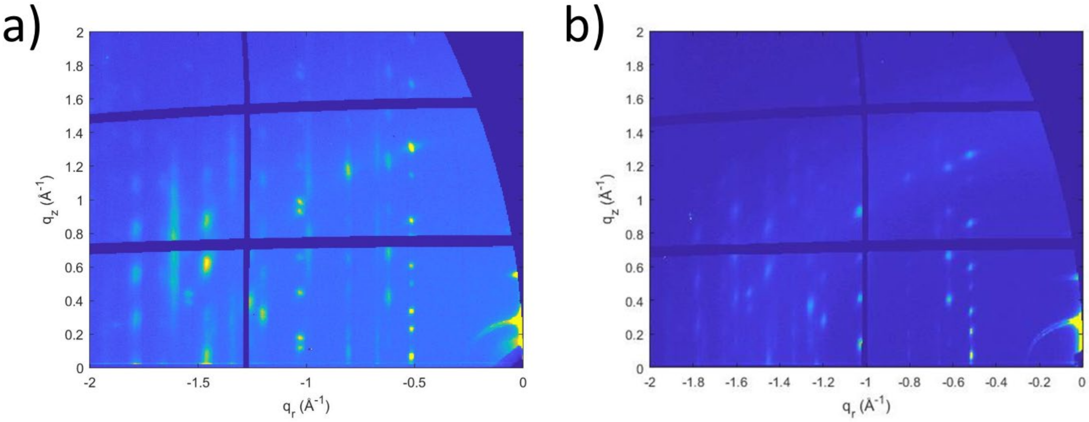

Figure A7. GIXD images of polymorph I of films annealed from polymorph I’ (a) and I’’ (b) showing the slight alignment in polymorph I as a result of initially forming polymorph I’’ (hence missing Bragg rods).

Table A5. Devices of polymorph I measured on aligned films annealed from polymorph I'' showing little to no difference from the non-aligned films annealed from polymorph I'.

Parallel

Device	μ ($cm^2 V^{-1} s^{-1}$)	V_{th} (V)
042919-14_A6b_t.csv	0.172	-35.2
042919-14_A7b_t.csv	0.158	-30.6
042919-14_A7c_t.csv	0.153	-27.7
042919-15_A4b_t.csv	0.126	-11.7
042919-15_A4c_t.csv	0.131	-13.1
042919-15_A5b_t.csv	0.105	-11.4
051619-2_A4b_t.csv	0.138	-22.8
051619-2_A4c_t.csv	0.144	-22.7
051619-2_A5b_t.csv	0.118	-26.0
051619-2_A5c_t.csv	0.126	-25.7
Average	0.137	-22.7
Standard Deviation	0.020	8.2

Perpendicular

Device	μ ($cm^2 V^{-1} s^{-1}$)	V_{th} (V)
041219-2_B1a_t.csv	0.194	-4.6
042919-15_B2a_t'.csv	0.244	-18.0
042919-14_B3c_t.csv	0.161	-53.9
Average	0.200	-25.5
Standard Deviation	0.042	25.5

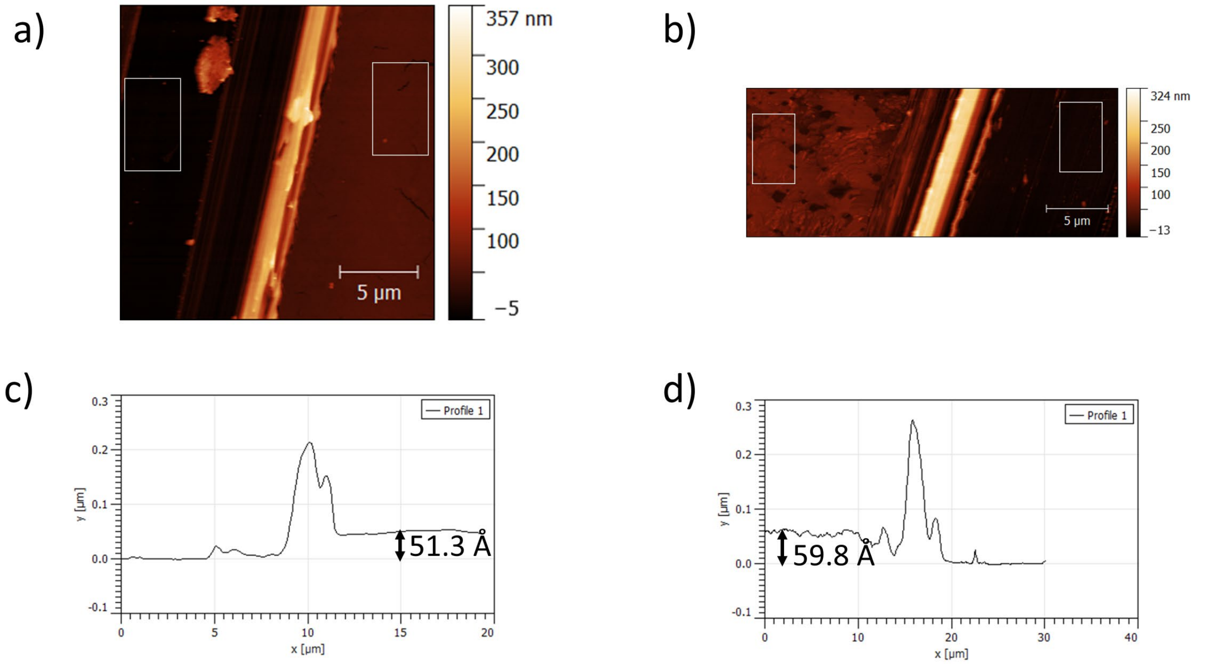

Figure A8. AFM images of films of polymorph I’ and I’’ (a, b respectively). Scratches were made using tweezers to obtain a profile difference between the substrate and the film. Once the images were flattened with respect to the substrate, profiles were obtained (c,d respectively) and a thickness was extracted by averaging a relatively flat part of both the film and substrate for polymorph I’ (51.3 nm) and I’’ (59.8 nm). These values were then subtracted and the averaged substrate value was set to zero. The effective area averaged is marked in the white boxes.

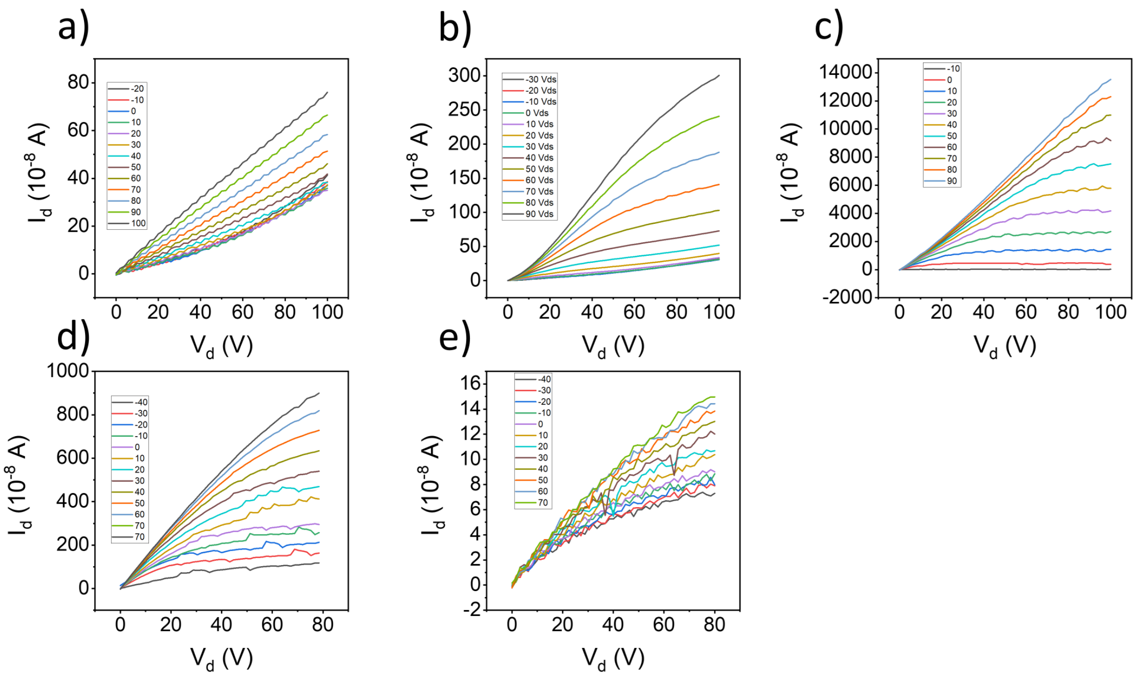

Figure A9. Output curves for polymorphs I', I'', I, II, III respectively (a,b,c,d,e), corresponding to the transfer curves presented in **Figure 2.4f-j**.

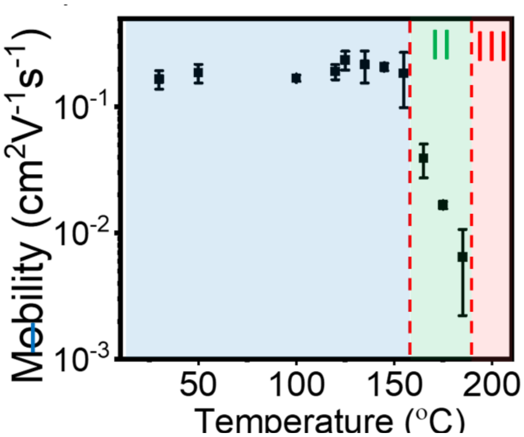

Figure A10. In situ device performance zoomed in to more clearly show the temperature dependence of polymorphs I and II.

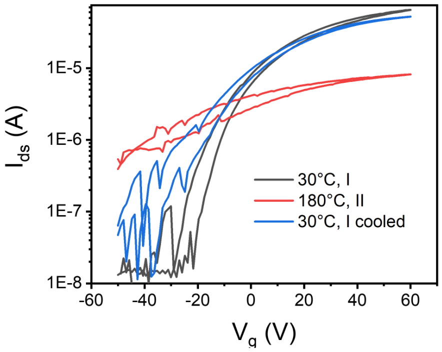

Figure A11. Transfer curve of a polymorph I device at room temperature (black), heated to form II at 180° (red) and the recovered polymorph I at room temperature (blue). The mobility and threshold voltage are summarized in **Table S6**.

Table A6. Summary of recovered device performance.

	I, Initial	II, heated	I, cooled
Mobility ($cm^2 V^{-1} s^{-1}$)	0.15	0.004	0.112
V_{th} (V)	-22.46	-88.61	-24.98

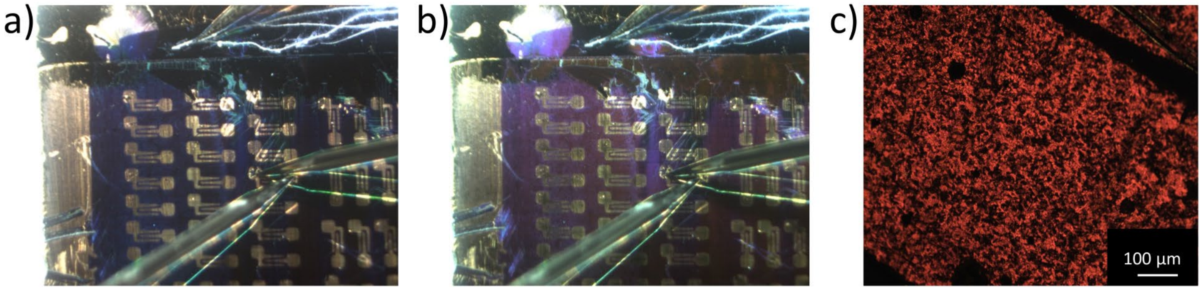

Figure A12. Optical images of OFETS at 175 (a) and 205 °C (b) showing a color change in the film, indicative of the II-III transition. (c) Thin film of polymorph III kinetically trapped at room temperature.

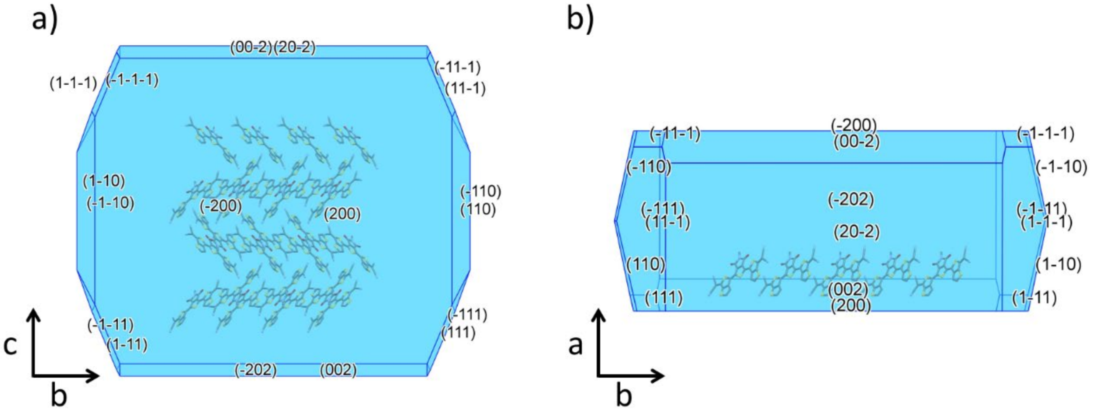

Figure B1. Relative size of each plane based on BFDH calculations looking down (a) *a** and (b) *c*-direction. The calculations suggest the larges plane should be the (200) plane, growing along the 1D π-stacks, consistent with the crystal shapes observed from dropcasting.

Table B1. Statistics for the I-II transition in single crystals

Crystal	**Cooling Transition Temperature (°C)**	**Heating Transition Temperature (°C)**	**Hysteresis (°C)**	**Midpoint Temp (°C)**	**Original length (μm)**	**Heated Length (μm)**	**% Change in Length**
090117-1	173.9	185.8	11.9	179.9	107.4	104.9	-2.35
090117-2	172.9	191.4	18.2	182.2	143.8	140.1	-2.60
090117-3	171.7	183.6	11.9	177.7	133.6	129.1	-3.38
090117-4	169.5	184.8	15.3	177.2	143.1	141.7	-0.96
091217-2	165.8	191.9	26.1	178.9	103.3	100.8	-2.50
110217-1	165.1	185.7	20.6	175.4	368.7	358.7	-2.73
110217-2	166.5	182.4	15.9	174.5	231.9	221.4	-4.51
110917-4-1	171.8	190.5	18.7	181.2	229.4	225.1	-1.88
110917-4-3	172	187	15	179.5	228.1	220.8	-3.19
110917-4-4	173.3	190	16.7	181.7	210.8	201.1	-4.58
110917-4-5	174.3	190.7	16.4	182.5	212.5	205.0	-3.56
110917-5-1	169.3	179	9.7	174.2	224.8	219.7	-2.26
110917-5-2	171	189	18	180.0	390.6	381.7	-2.28
110917-6.1-1	166.8	186.1	19.3	176.5	160.4	151.7	-5.43
110917-6.1-2	174.8	187.1	12.3	181.0	258.0	250.1	-3.06
110917-6-1	164.8	180.1	15.3	172.5	265.2	251.3	-5.23
110917-6-2	161.1	182.9	21.8	172.0	281.2	264.3	-6.03
110917-6-3	162.9	173.1	10.2	168.0	166.0	157.8	-4.92
110917-6-4	163.6	179.6	16	171.6	292.2	276.9	-5.23
120117-PtS-1-1	175	185.7	10.7	180.4	309.4	292.6	-5.44
120117-PtS-1-2	169.1	192.8	23.7	181.0	335.3	321.1	-4.23
120117-PtS-1-3	166	188.3	22.3	177.2	304.7	294.6	-3.33
120117-PtS-2-1	168.5	194.1	25.6	181.3	365.3	353.0	-3.37
120117-PtS-2-2	172.8	181.7	8.9	177.3	256.3	250.8	-2.13
120117-PtS-2-3	175.6	189	13.4	182.3	117.0	112.4	-3.98
120517-2-1	167.2	192.4	25.2	179.8	341.6	330.2	-3.33
120517-2-2	168.2	182.4	14.2	175.3	258.0	248.9	-3.53
120517-2-3	166.6	179.8	13.2	173.2	214.1	204.3	-4.60
		Average	**16.7**	**172**		**Average**	**-3.59**
		Standard Deviation	**4.97**	**1.54**		**Standard Deviation**	**1.27**

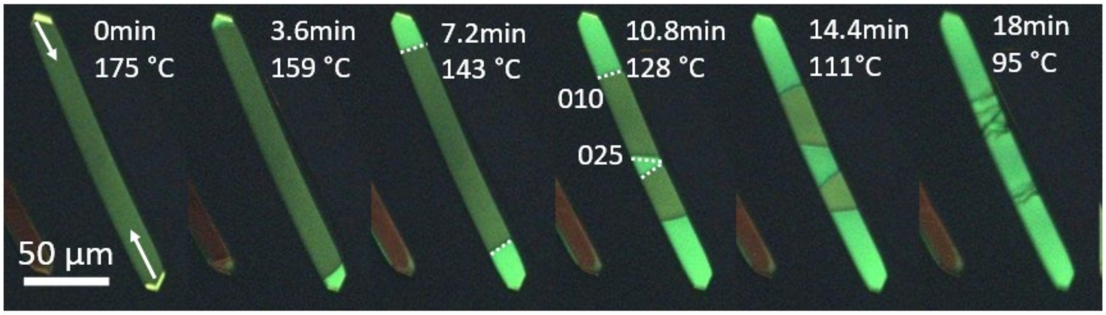

Figure B2. POM images of the II-I transition showing cracking upon convergence of independently initiated phase boundaries. The full movie is shown in **Movie B5**.

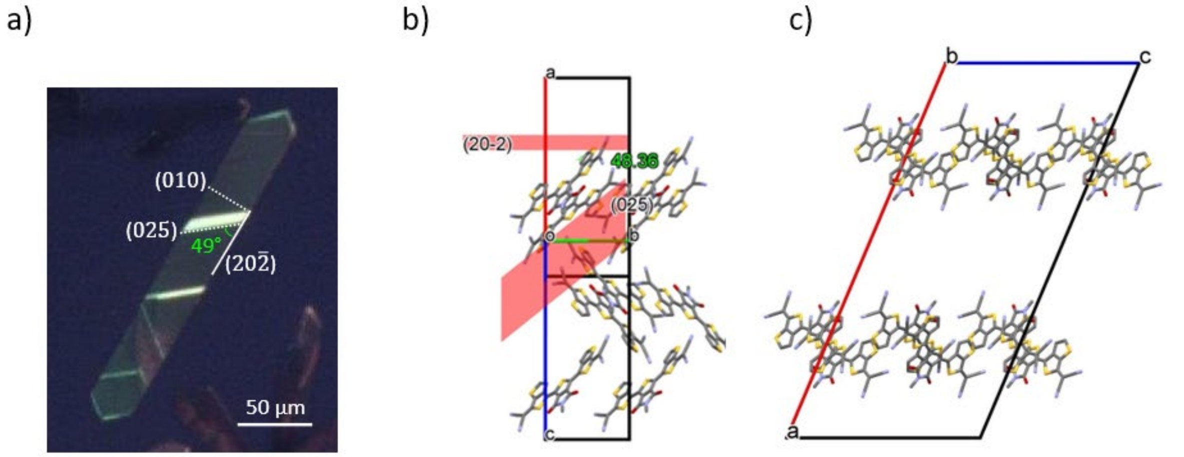

Figure B3. (a) POM images of the II-I transition showing both the (025) plane orientation for the phase boundary. (b) The relationship between the (025) plane and the π-stacking plane of the molecule. The angles between the (025) and $(20\bar{2})$ in the POM image (a) was measured using ImageJ. The angle based on the unit cell was measured using Mercury. Angles are indicated in green and show a close correlation between the π-stacking plane and the phase boundary. (c) The (010) looking down the π-stacking columns

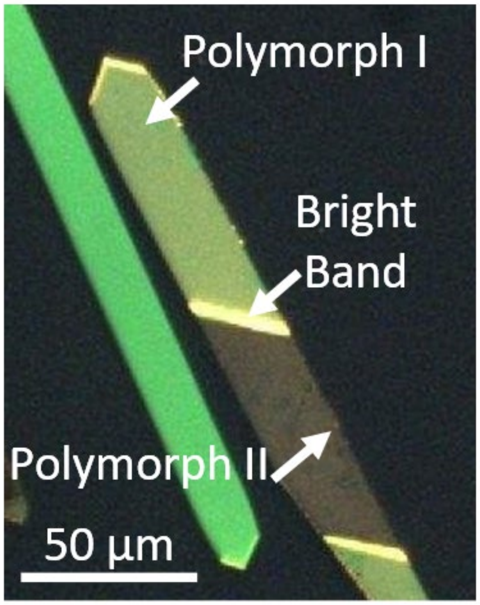

Figure B4. During the avalanche behavior, bright bands sometimes occur that the phase boundary, suggesting strain buildup along the boundary.

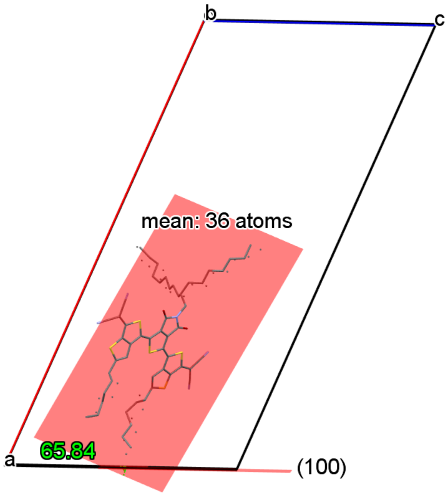

Figure B5. The angle between the conjugated core and the (100) plane (66°) shows a consistent tilt with the complementary β-angle, measured to be 67°.

Quinoidal Raman Peak Assignment

To interpret changes in the intramolecular vibration region (900-1800 cm^{-1}), we assigned the Raman peaks based on a combination of literature and DFT calculations, as discussed in the methods. DFT simulations of the 2DQTT-o-B vibrational spectra shows one dominant vibrational mode which we expect corresponds to the most intense peak in the experimental Raman spectra (**Figure B6a,b**). This suggests a 200 cm^{-1} systematic shift between the experimental and simulated data, which we attributed to performing the simulations on single molecules. The most intense peak measured at 1387 cm^{-1} experimentally (peak 1 in **Figure B6b**), has typically been assigned the collective vibrations of the C-C/C=C bonds in the conjugated core, known as the effective conjugation coordinate (ECC) mode in similar molecules[127–129]. In simulations of 2DQTT-o-B, we observed the ECC mode (1387 cm^{-1}) comprises 2 peaks exhibiting stretching of the TBT and TPD moieties and stretching along the backbone at 1581 and 1584 cm^{-1} (**Figure B6c**, **Movies B8-9**) respectively. Taken together, these vibrational modes stretch along the conjugated C=C bonds, as expected for the ECC mode, and are collectively denoted as $\nu(C{=}C)_{ECC,Q}$ shown in **Figure 3e** (where Q specifies the quinoidal form). Notably in the experimental spectra, we observe medium intensity peaks at 1409 cm^{-1}, 1522 cm^{-1}, and 1772 cm^{-1} (peaks 2-4 in **Figure B6b**) that seem to correspond to low intensity peaks in the simulated spectra. Discrepancy in simulated spectra, as we explain below, are likely related to effects from the alkyl chains (omitted from simulation) and molecular packing which were prohibitively difficult to simulate in this case. We suggest 1522 cm^{-1} and 1772 cm^{-1} correspond to another $\nu(C{=}C)_{TPD}$ in the central TPD ring and $\nu(C{=}O)$ respectively which have corresponding weak vibrational modes in the simulated spectra at 1636cm^{-1} (**Figure S6e**, **Movie B10**) and 1878 cm^{-1} (**Figure B6f**, **Movie B11**). While the simulated intensities were much lower than the measured Raman activity, electron-phonon coupling in the solid state and reduction of the molecular symmetry has a dramatic effect on the calculated intensities for these vibrational modes[138,181,182].

As for the peak at 1409 cm^{-1}, while it seems to correspond to the simulated band at 1610 cm^{-1} (**Figure B6d, Movie B12**), it also overlaps with the CH_2 deformation peak ($\delta(CH_2)$) in the alkyl chains which the simulation does not capture. This vibrational mode involves scissoring of the CH_2 group (**Figure 3.3e**) and has been well studied in literature from alkanes and oligothiophenes with tethered alkyl chains[130–133]. However, assigning these modes based solely on the simulated Raman and literature alone is difficult given the possible overlap with core stretching peaks. In order to confirm the attribution of these peaks to the alkyl chains, we measured the Raman spectra of crystals formed using 2DQTT-C_2C_4, containing the same quinoidal core and only differing in the length of the branched alkyl chains (**Figure B7**). We observed the position and relative intensities of peaks assigned to the quinoidal core show no change upon modification of the alkyl chain. On the other hand, the peak at $\delta(CH_2)$ 1409 cm^{-1} showed substantial reduction in the intensity 2DQTT-C_2C_4, confirming the assignment of this peak to the alkyl chains rather than another core C=C stretching mode. Similarly, based on literature[130–133] and comparison with 2DQTT-C_2C_4, we assign peaks at 1025 cm^{-1} and 1063 cm^{-1} to alkyl C-C stretching of the trans ($\nu(C\text{-}C)_T$) and gauche ($\nu(C\text{-}C)_G$) conformations respectively (**Figure B7**). In the C_2C_4 Raman spectra, the trans C-C stretching mode showed a substantial difference in peak position and presents a new peak at a slightly lower wavenumber. This peak splitting is likely due to the shorter C_2 alkyl chains no longer containing the CH_2-CH_2 bond present in the other alkyl chains. Given the only difference between these molecules is the side chains, this confirms our assignments of the alkyl chain vibrations. The assignment of these modes offers a framework with which to understand the observed peak evolution previously discussed.

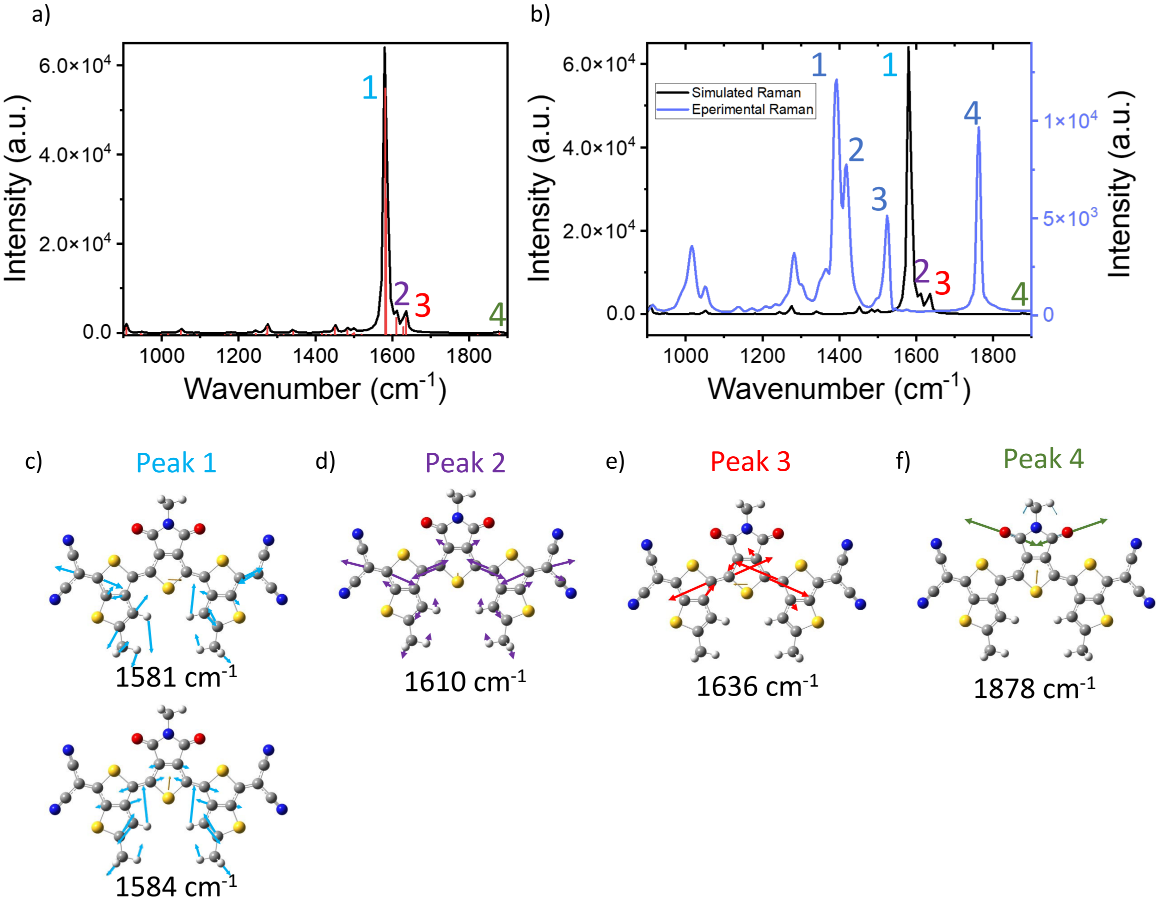

Figure B6. (a) Simulated Raman spectroscopy showing 4 major core stretching peaks. (b) Comparison between the simulated (black) and experimental (red) spectroscopy, showing a qualitatively similar fingerprint offset by approximately ~100 cm^{-1}. (c) The vibrational modes corresponding to the most Raman active vibrations in each peak corresponding to **Movies B8-12**. Based on this, we were able to assign the most intense peak (peak 1) to the ECC mode $\nu(C=C)_{ECC,Q}$ Compared to the experimental spectra, the most intense Raman peak was observed near 1387 cm^{-1}, 200 cm^{-1} lower than the simulation results. This is likely due to the simulation being performed on single molecules at low temperatures, and we see this 200 cm^{-1} shift is similar for all the observed peaks.

The most intense simulated peak was calculated to be composed of 2 peaks at 1581 and 1584 cm^{-1} We expect experimental Peak 2 to be mainly the $\delta(CH_2)$ mode based on well documented literature, we could not simulate the full alkyl chains in this simulation. This assignment was confirmed via performing Raman on 2DQTT-C_2C_4 in **Figure B7**. Peaks 3 and 4 we assigned based on simulated weak peaks and are likely stronger in the experimental spectra as a result of intermolecular interactions in the crystal structure.

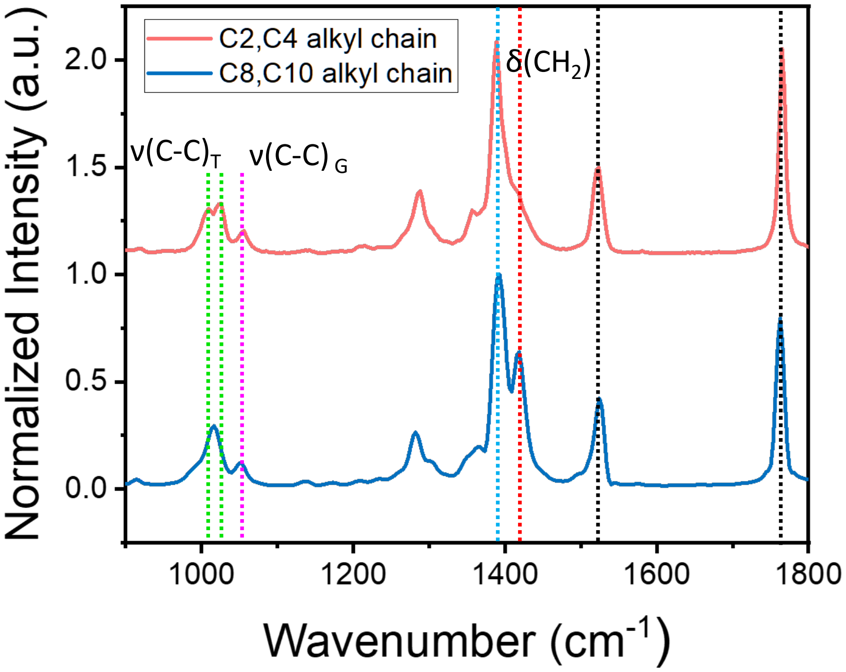

Figure B7. Experimental Raman spectra for 2DQTT-C_8C_{10} (blue) and 2DQTT-C_2C_4 (red) showing modulation of the peak splitting of the ν(C-C)$_T$ (green dotted lines) and intensity of the δ(CH$_2$) vibrational mode associated with the alkyl chains and little to no change to the core C=C stretching peaks (black), confirming these Raman assignments.

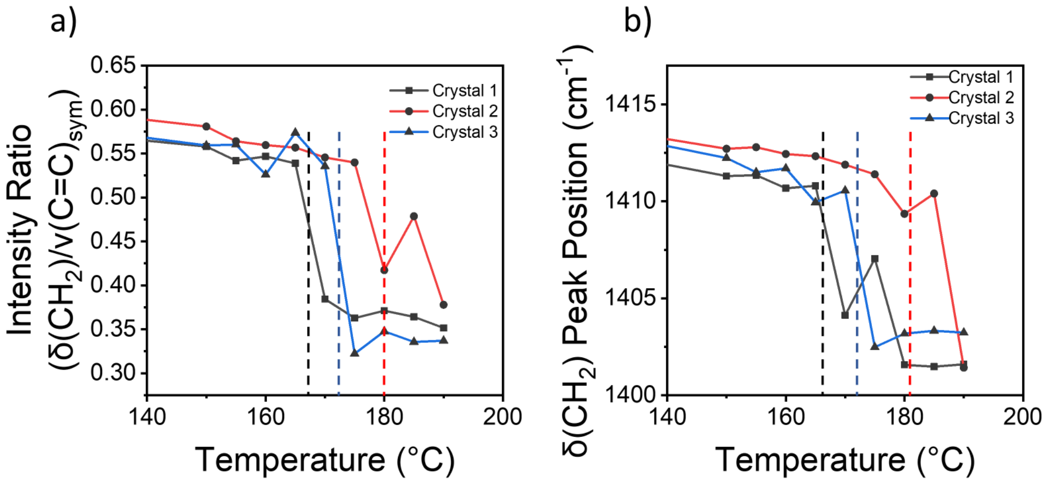

Figure B8. Repeated experiments from **Figure 3.3** showing the consistency of (a) the decrease in the δ(CH$_2$)/ν(C=C)$_{core}$ intensity ratio and (b) the redshift in the δ(CH$_2$) peak. This experiment was performed on 3 separate crystals, each of which transitioned at different temperatures indicated by the dashed line. The transition temperatures were observed and recorded based on the shape change evident under the optical microscope linked with the Raman spectroscopy setup. The discrepancy in the data point at 185 °C is likely the result of the avalanche behavior and measuring at different locations in the crystal. This resulted in accidental measurement of polymorph I that had not finished converting when moving the laser back and forth between each crystal.

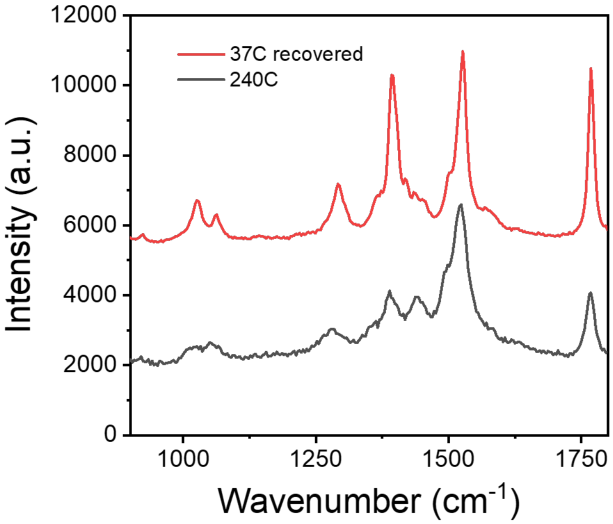

Figure B9. Raman spectra of polymorph III at high temperature (red) and after cooling (black). Upon cooling, while the alkyl ν(C-C) stretching has returned to a high ratio, suggesting solidification, biradical signatures are still observed. The intensity has decreased, but the signatures are still observable.

Aromatic Raman Peak Assignment

To investigate this possibility of a quinoidal to aromatic transition, we simulated the vibrational spectra of an aromatic analogue to 2DQTT-o-B by removing the cyano groups and replacing them with hydrogens (**Figure B10a**) which forced the BLA into the aromatic form while still allowing for structural optimization using the ωB97X-D functional and def2TZVPP basis set. From the simulation of the aromatic form of the molecule, we observed 2 main intense peaks which showed a clear symmetric and asymmetric stretching of the core C=C bonds (the aromatic ECC stretching modes, $\nu(C{=}C)_{ECC,A}$, $\nu(C{=}C)_{asym}$), at 1618 and 1635 cm^{-1}, respectively (**Figure B10b-c, Movie B14-15**). The DFT simulation suggested the aromatic peak should form at higher wavenumbers, approximately a shift of 40 cm^{-1} relative to the quinoidal ECC stretching (**Figure B10d**). This simulated shift is quite close to the experimental difference between the quinoidal ($\nu(C{=}C)_{ECC,Q}$) and aromatic ($\nu(C{=}C)_{ECC,A}$) peaks, which was measured to be 52 cm^{-1}. This suggests the simulated $\nu(C{=}C)_{ECC,A}$ and $\nu(C{=}C)_{asym}$ peaks correspond to the experimentally observed peaks forming at 1440 and 1497 cm^{-1} during the II-III transition (**Figure 3.4f**, **Figure B10e**). Moreover, this assignment is consistent with observations in previous literature results[98,161,181], which also showed the aromatic peaks forming at higher wavenumbers compared to the quinoidal vibrational mode.

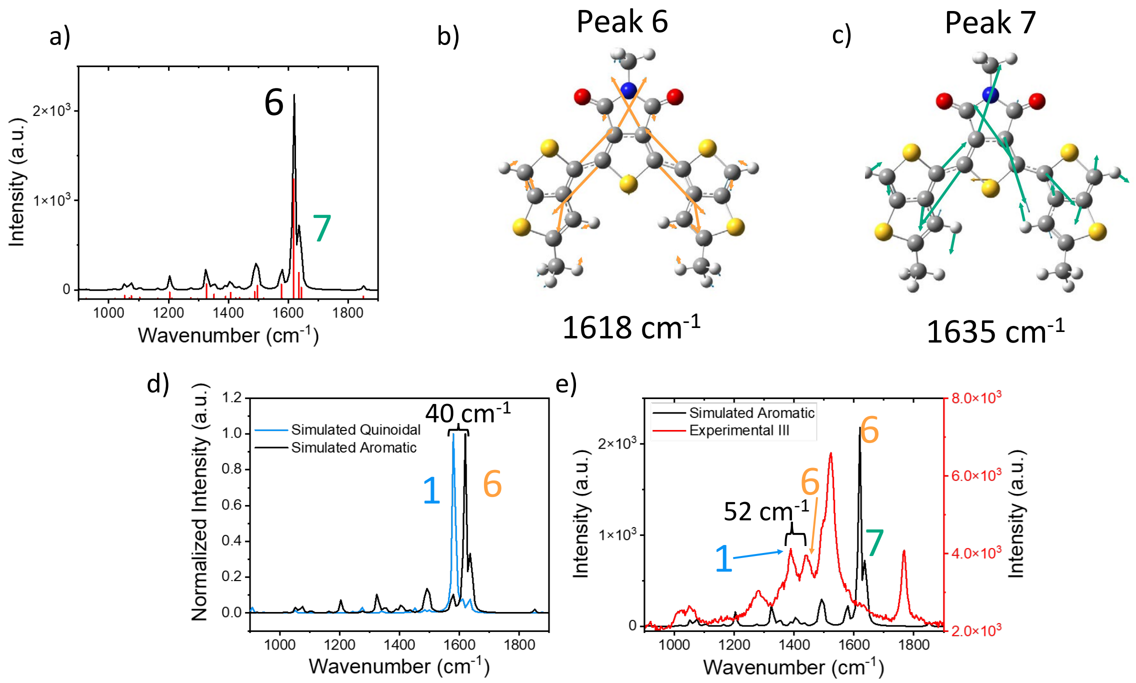

Figure B10. (a) Simulated Raman spectroscopy showing 2 major core stretching peaks in the aromatic form of the molecule. The simulation was performed by removing the cyano groups and allowing full relaxation of the molecule. The main vibrational mode is associated with (b) the ECC symmetric mode $\nu(C=C)_{ECC,A}$ and (c) the ECC asymmetric mode $\nu(C=C)_{ECCasym,A}$, corresponding to **Movies B14-15** respectively. (d) Comparison between the simulated aromatic (black) and quinoidal (blue) Raman spectroscopy, showing an increase of 40 cm^{-1} between the ring breathing modes (most intense peaks). (e) Comparison between the simulated aromatic Raman spectra (black) and the experimental spectra taken from polymorph III at 240 °C. The experimental spectra shows an increase of 52 cm^{-1}, similar to the shift based on the simulated Raman spectra of 40 cm^{-1}, and consistent with trends shown in literature.

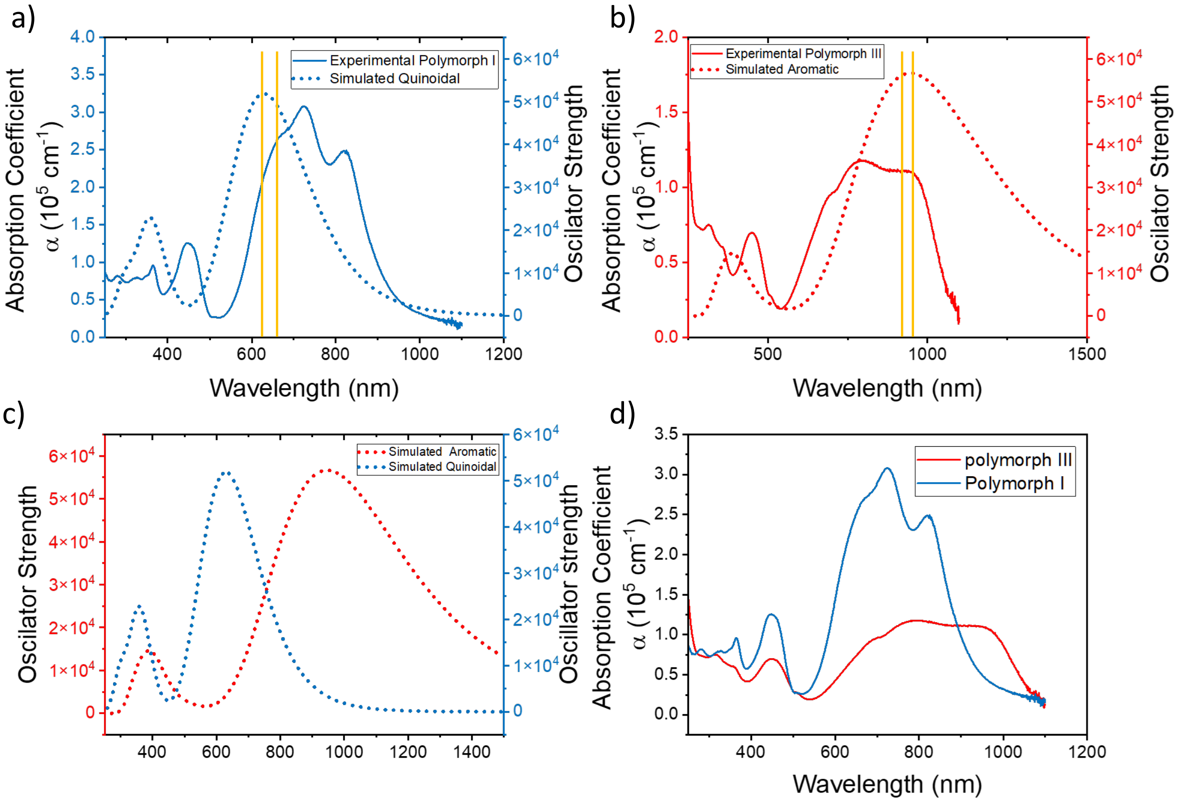

Figure B11. (a) Comparison of simulated UV-Vis absorption spectra for the *quinoidal* form with polymorph I. (b) comparison of simulated UV-Vis absorption spectra for the *aromatic* form with polymorph III. (c) showing the red shift in the lowest energy peak from the quinoidal to aromatic form and (d) a corresponding redshift in the experimental absorption spectra in polymorphs I and III.

APPENDIX C: SUPPLEMENTARY MATERIALS FOR CHAPTER 4

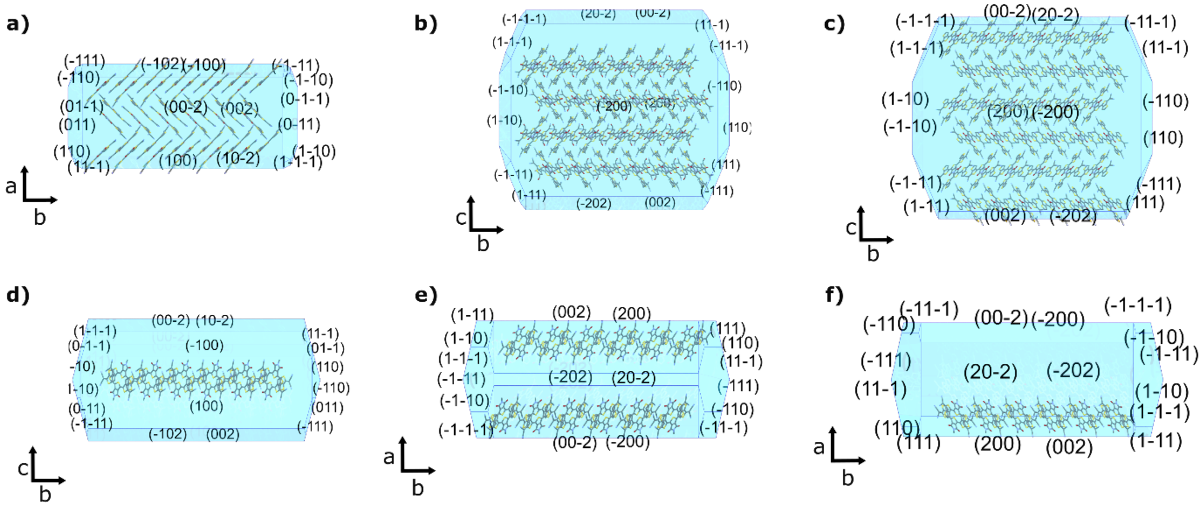

Figure C1. Relative size of each plane based on BFDH calculations for C_2C_4 (a,d), C_6C_8 (b,e) C_8C_{10} (c,f). The calculations show the (002) plane for the C_2C_4 crystal and the (200) plane for the C_6C_8 and C_8C_{10} crystals are the large planes, respectively. This suggests the longest direction is the π-stacking direction, consistent with the crystal shape.

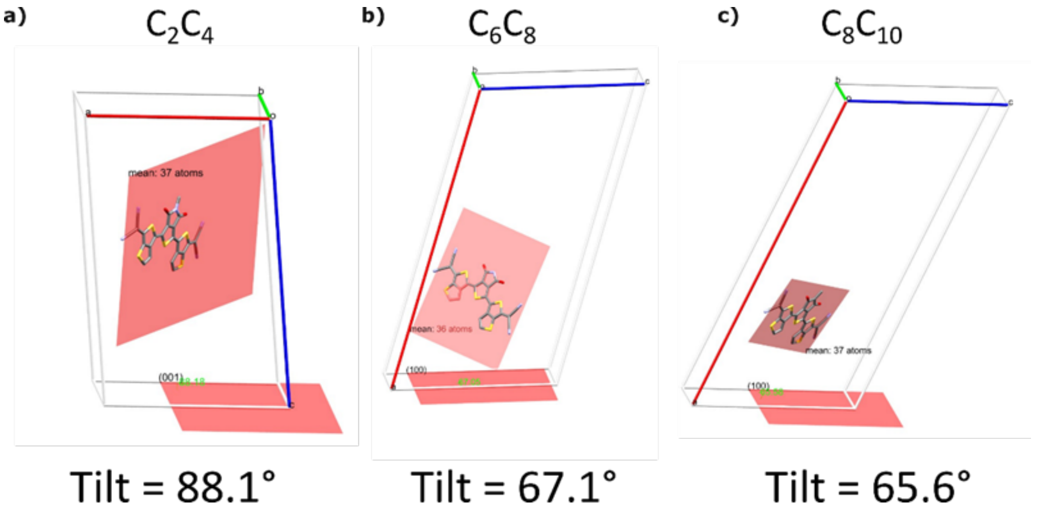

Figure C2. (a) Angle between the average plane of the conjugated core and the (001) plane for the C_2C_4 molecule. Angle between the average plane of the conjugated core and the (100) plane for the C_6C_8 (b) and C_8C_{10} (c) molecules. This tilt angle represents the tilt of the molecule relative to the substrate, suggesting that the C_2C_4 molecule is nearly standing up with respect to the substrate.

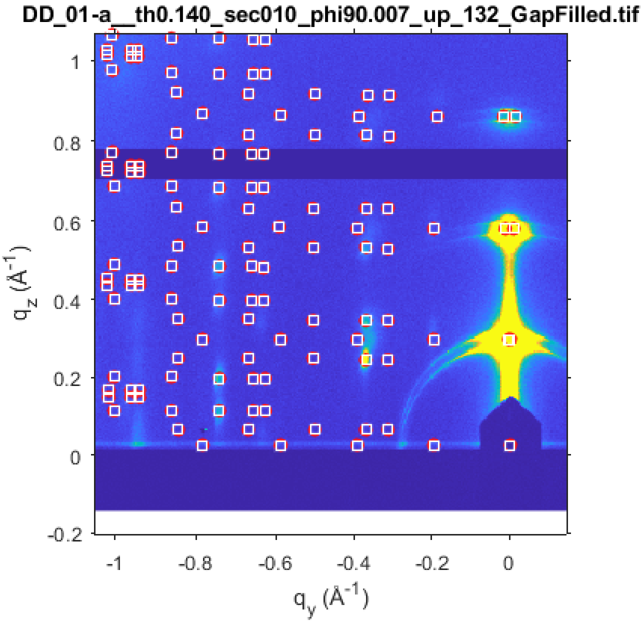

Figure D1. Unit cell simulation for polymorph IV showing a match between the simulated and experimental diffraction pattern.

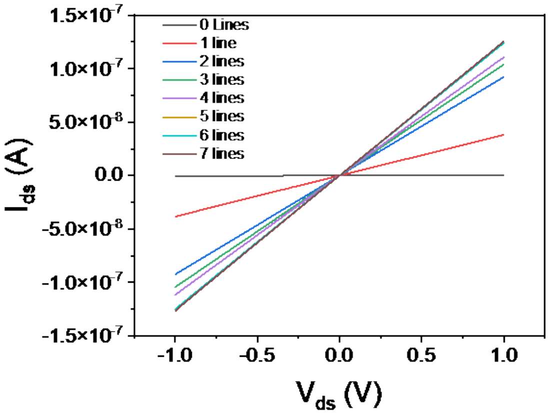

Figure D2. IV curves measured for memristor device 1 after each lasing event.

APPENDIX E: SUPPLEMENTARY MOVIE FILES

The supplementary materials contain a number of videos depicting the in situ POM videos discussed in the text. Videos correspond to chapters 2 (A), 3 (B) and 4 (C). All supplemental videos are listed below.

Movie A1: Movie showing the I″–I transition in thin films

Movie A2: Movie showing the I′–I transition in thin films

Movie A3: Movie showing the I–II transition in thin films

Movie A4: Movie showing the II–III transition in thin films

Movie A5: GIXD movie showing the I–II transition in thin films

Movie A6: GIXD movie showing the II–III transition in thin films

Movie B1: Movie showing the I–II heating transition in single crystals

Movie B2: Movie showing the II–I cooling transition in single crystals

Movie B3: Movie showing the II–III Heating transition in single crystals

Movie B4: Movie showing the III–II cooling transition in single crystals

Movie B5: Movie showing cracking during the II-I cooling transition in single crystals

Movie B6: Movie showing the thermosalient motion during the I-II transition in large single crystals

Movie B7: GIXD movie showing the I–II transition in thin films

Movie B8: Movie showing calculate vibrational mode at 1581 cm-1 for the quinoidal form

Movie B9: Movie showing calculate vibrational mode at 1584 cm-1 for the quinoidal form

Movie B10: Movie showing calculate vibrational mode at 1636 cm-1 for the quinoidal form

Movie B11: Movie showing calculate vibrational mode at 1878 cm-1 for the quinoidal form

Movie B12: Movie showing calculate vibrational mode at 1610 cm-1 for the quinoidal form

Movie B13: GIXD movie showing the II–III transition in thin films

Movie B14: Movie showing calculate vibrational mode at 1618 cm-1 for the aromatic form

Movie B15: Movie showing calculate vibrational mode at 1636 cm-1 for the aromatic form

Movie C1: Movie showing the I–II transition in single crystals of the C_6C_8 molecule

Movie C2: Movie showing the I–II transition in single crystals of the C_8C_{10} molecule

Movie C4: Movie showing no transition in single crystals of the C_2C_4 molecule from 85-265 °C

Movie C4: Movie showing the I–III transition in single crystals of the C_2C_4 molecule

Movie C5: Movie showing the II–III transition in single crystals of the C_6C_8 molecule

Movie C6: Movie showing the II–III transition in single crystals of the C_8C_{10} molecule